



# The atomic structure of inversion domains and grain boundaries in wurtzite semiconductors: an investigation by atomistic modelling and high resolution transmission electron microscopy

Siqian Li

## ► To cite this version:

Siqian Li. The atomic structure of inversion domains and grain boundaries in wurtzite semiconductors: an investigation by atomistic modelling and high resolution transmission electron microscopy. Other [cond-mat.other]. Normandie Université, 2018. English. NNT: 2018NORMC252 . tel-02064267

**HAL Id: tel-02064267**

**<https://theses.hal.science/tel-02064267>**

Submitted on 11 Mar 2019

**HAL** is a multi-disciplinary open access archive for the deposit and dissemination of scientific research documents, whether they are published or not. The documents may come from teaching and research institutions in France or abroad, or from public or private research centers.

L'archive ouverte pluridisciplinaire **HAL**, est destinée au dépôt et à la diffusion de documents scientifiques de niveau recherche, publiés ou non, émanant des établissements d'enseignement et de recherche français ou étrangers, des laboratoires publics ou privés.

## THÈSE

**Pour obtenir le diplôme de doctorat**

**Spécialité PHYSIQUE**

**Préparée au sein de l'Université de Caen Normandie**

**The atomic structure of inversion domains and grain boundaries in wurtzite semiconductors : an investigation by atomistic modelling and high resolution transmission electron microscopy**

**Présentée et soutenue par  
Siqian LI**

**Thèse soutenue publiquement le 04/12/2018  
devant le jury composé de**

M. JOEL DOUIN	Directeur de recherche, CEMES	Rapporteur du jury
M. ABDELKRIM REDJAIMIA	Professeur des universités, UNIVERSITÉ LORRAINE	Rapporteur du jury
M. JUN CHEN	Professeur des universités, UNIVERSITE CAEN NORMANDIE	Membre du jury
Mme LUCIA REINING	Directeur de recherche, ECOLE POLYTECHNIQUE	Président du jury
M. PIERRE RUTERANA	Directeur de recherche au CNRS, 14 ENSI de Caen	Directeur de thèse
Mme MAGALI MORALES	Maître de conférences HDR, UNIVERSITE CAEN NORMANDIE	Co-directeur de thèse

**Thèse dirigée par PIERRE RUTERANA et MAGALI MORALES, Centre de recherche sur les ions, les matériaux et la photonique (Caen)**

## Acknowledgments

*This thesis has been carried out at CIMAP Laboratory (Centre de recherche sur les Ions, les Matériaux et la Photonique), it was supported by the china scholarship council (CSC) for financial support under the file number 201508420147. My greatest thanks belong to my supervisors **Drs. Pierre Ruterana** and **Magali Morales** for the countless fruitful discussions, suggestions and supports during this research.*

*I would like to thank the members of jury: especially **M. Joel Douin** and **M. Abdelkrim Redjaimia** who accepted to review my work and **Mrs. Lucia Reining**, as well as **M. Jun Chen** for their valuable comments and suggestions.*

*Special thanks are due to my collaborators, **Prof. Hadiç Morkoç**, **Dr. Barkat Ullah** and **Dr. Vitaliy Avrutin** who grew the ZnO/GaN heterostructures. I would like to thank **Prof. Slawomir Kret** (institute of Physics, Polish Academy of Science (IP-PAS), Warsaw Poland) who hosted me for high-resolution analytical transmission electron microscopy training, along with **Dr. Lei Huaping** (Heifei Institute of Physics Science, Chinese Academy of Science CAS, Hefei) who kindly introduced me to the first-principles methods with Vienna ab initio simulation package. I am very thankful to **Prof. Jun Chen** and **Dr. Viwanou Hounkpati** who supported and discussed with me about the technical questions on theoretical calculations.*

*My gratitude goes to all the PM2E group members: **Dr. Albert Minj** for his kind help and patient explanations; **Dr. Hichem Ben Ammar**, **Nicolas Chery**, **Farah Bouazzaoui** and **Marie-Pierre Chauvat** who brought a lot of happy times and support all along these three years.*

*Besides, I would like to thank all the following people who always offer me help and support me to overcome the difficulties. My Master degree's advisor: **Prof. Zhang Jun** who always encourages and inspires me. **Prof. Guosheng Shao** and **Dr. Zhuo Wang** who hosted me for a visit and guided me for my further studies.*

*I am grateful to the PSIME graduate school for support of my visits out of the University of Caen Normandie. And also, I acknowledge the extensive use of the computer resources of CRIANN "Centre Regional Informatique et d'Applications Numériques de Normandie" under project No. 2016009.*

# **Structure atomique des domaines d'inversion et joints de grains dans les semiconducteurs wurtzites : Modélisation atomistique et microscopie électronique haute résolution**

Les semiconducteurs nitrures d'éléments III (AlN, GaN, InN) et le ZnO de structure wurtzite sont des matériaux d'une grande importance pour les applications optoélectroniques en raison de leurs larges bandes directes qui couvrent la plus large gamme de longueurs d'onde d'émission pour une seule famille de matériaux de l'ultraviolet lointain (6.2 eV) au proche infrarouge (0.65 eV) en ce qui concerne les nitrures. Ils sont donc très attendus pour de très nombreuses applications en optoélectronique et microélectronique. Ils sont le sujet de recherches très intenses pour optimiser la qualité des couches minces, et donc les investigations portent sur tous les aspects : les mécanismes de croissance, les propriétés structurales comme l'élasticité, la polarité, les défauts cristallins, etc. ... En effet, dans ces couches minces obtenues par épitaxie sur divers substrats, les défauts de croissance vont jouer un rôle important sur les propriétés du matériau et les performances de dispositifs.

Au cours de ce travail, nous avons étudié particulièrement deux types de défauts plans: l'inversion de polarité dans le plan (0001), et les joints de grain de rotation autour de l'axe [0001]. Nous avons ainsi pu déterminer la structure atomique la plus stable dans ce plan d'inversion pour les composés wurtzite et l'hétérostructure ZnO/GaN et ensuite celle des joints, grâce à deux approches complémentaires menées en parallèles: l'investigation au microscope électronique haute résolution et la modélisation atomistique par des techniques *ab initio*. Ceci nous a permis non seulement de connaître la structure intime, mais aussi de mettre en évidence les propriétés électroniques correspondantes.

Le manuscrit de cette thèse contient six chapitres:

Le chapitre 1 examine les propriétés structurales et électroniques fondamentales des composés des nitrures et de ZnO, en passant d'abord en revue la structure wurtzite, ses propriétés élastiques, et la polarité induite. Dans ce chapitre, nous avons aussi décrit brièvement les techniques de croissance des matériaux analysés, ainsi que les principaux défauts rencontrés dans les couches minces correspondantes.



Le chapitre 2 rappelle la théorie de la densité fonctionnelle et introduit les principales approximations qui ont permis d'aborder de façon raisonnable la résolution de l'équation de Schrödinger, jusqu'aux programmes de résolution pratiques que nous avons utilisés dans ce travail.

Dans le chapitre 3, nous présentons les résultats obtenus sur la structure du plan d'inversion (0001) dans ZnO et les nitrures d'éléments III. Il s'agit d'une modélisation entièrement théorique où nous avons analysé la stabilité structurale, les propriétés de liaison chimique ainsi que la structure électronique.

Le chapitre 4 propose une corrélation entre les analyses de la structure atomique par microscopie haute résolution et la modélisation *ab initio* de l'inversion de polarité à l'hétérointerface ZnO/GaN. Ainsi, la configuration la plus stable du point de vue énergétique a été déterminée, et imposée par la polarité Ga du substrat GaN, il est montré que cette inversion dans une monocouche se forme sur une couche métallique contrairement à ce qui avait été rapporté auparavant.

Dans le chapitre 5, nous discutons des résultats originaux obtenus sur des joints de grains de rotation autour de l'axe [0001] qui est la direction de croissance des couches étudiées. Plus particulièrement en utilisant le dépôt en phase vapeur assisté par plasma, nous avons pu obtenir des couches de ZnO polycristallin sur saphir avec seulement deux orientations: en maintenant l'axe [0001] commun, les nano-domaines adjacents avaient leurs axes  $[11\bar{2}0]$  et  $[10\bar{1}0]$  parallèles. Théoriquement, il y avait donc une rotation de  $30^\circ$  ou alors de  $90^\circ$  entre ces domaines. Par microscopie haute résolution, nous avons systématiquement observé la formation des joints de grain de type  $\Sigma 13$ , de rotation de  $32.2^\circ$  ou  $27.8^\circ$ . Plus intéressant, les interfaces correspondantes étaient systématiquement soit le côté ou alors la diagonale de la cellule unitaire de coïncidence. Ainsi, nous avons eu la possibilité de montrer que le concept d'unités structurales existait dans la structure wurtzite. En effet, pour la première fois, et pour quatre joints de grains, on peut observer exactement les dislocations prévues par la théorie topologique. Plus particulièrement dans ZnO, la structure atomique de la dislocation coin  $[10\bar{1}0]$  avec un cœur spécifique large de 486-atomes est montré comme une unité structurale fondamentale pour ces joints de grain de symétrie wurtzite.

Au chapitre 6, une conclusion générale et des perspectives de ce travail sont présentées.



## Introduction

Group III-nitrides and ZnO semiconductors are of great importance materials for the optoelectronics applications due to their wide direct band gaps which cover from the ultraviolet to infrared energy range. It has been a subject of intense investigations on their structural properties like elasticity, polar nature et al., growth mechanism such as polarity control, as well as lattice defects. Among these investigations, the structural defects gained from the film epitaxy growth may influence the material property and further degrade the device performances which consequently received a great deal of attentions in this field. With the thesis, we pay more attention to the two kinds of planar defects: (0001) plane inversion domain boundary (IDB) and [0001] tilt grain boundary (GB). The aim of this work is to clarify the interfacial configuration of (0001) plane IDB at ZnO/GaN heterointerface and the core structure of [0001] tilt GB using precise atomic scale STEM measurements and extensive theoretical simulations. Furthermore, based on the determined atomic structures, the electronic properties are studied as well.

The doctoral dissertation is segmented into five chapters:

Chapter 1 reviews the fundamental structural and electronic properties of group III-nitrides and ZnO compounds including wurtzite crystal, elasticity character, and polarization. In addition, several thin film growth techniques and the selected planar defects are introduced as well.

Chapter 2 briefly reviews the development of density functional theory. Some particular approximations and algorithms are introduced. At the end, the advantages of two kinds of ab initio packages used in this thesis are related.

Chapter 3 deals with the investigation of (0001) plane inversion domain boundary in group III-nitrides and ZnO homogeneous compounds. A completely theoretical calculation is presented. Comparison of structural stability, chemical bonding properties as well as the defective state in electronic structure are analyzed in this chapter.

Depending on the theoretical investigations in chapter 3, the (0001) plane IDBs are implemented in more complex interface, ZnO/GaN heterointerface, since the lattice mismatch between the two materials is moderate (1.8%) and successfully achievement of ZnO/GaN heterojunction based devices. Chapter 4 first presents a serial of atomic scale TEM

images to uncover that polarity reversal took place at one monolayer at ZnO/GaN heterointerface. Based on the theoretical studies in chapter 3, eight (0001) plane IDB models are constructed for the ZnO/GaN heterointerface and their thermodynamical stability, chemical bonding as well as electron structure are investigated.

Chapter 5 discusses a study of [0001] tilt GBs in ZnO. High-resolution TEM is used to analyze the core structure of grain boundaries. For the first time, the  $[10\bar{1}0]$  edge dislocation with a specific core of 486-atom ring is shown to be a characteristic structural unit of this grain boundaries of wurtzite symmetry in agreement with early theoretical reports. Furthermore, the defective state on valence band edge is discussed as well.

In chapter 6, a general conclusion and perspectives of this investigation are given.

## Table of contents

Acknowledgements	i
Introduction	v
Table of Contents	vii
Chapter 1 Wurtzite Semiconductors	1
1.1 Crystal Structure and Related Properties	1
1.1.1 Crystal Structure	1
1.1.2 Elastic Strain	3
1.1.3 Polarity Property	4
1.2 Growth Techniques	8
1.2.1 Substrates	8
1.2.2 Plasma-Induced Molecular Beam Epitaxy (PIMBE)	9
1.2.3 Plasma-Assisted Sputtering	10
1.3 Extended Defects	11
1.3.1 Inversion Domain Boundaries (IDBs)	11
1.3.2 Grain Boundaries (GBs)	14
References	17
Chapter 2 Density Functional Theory and Application Techniques	20
2.1 Schrödinger Equation	20
2.2 Born-Oppenheimer Approximation	21
2.3 Density Functional Theory	22
2.3.1 The Hohenberg-Kohn Theorems	23
2.3.2 The Kohn-Sham Equations	24
2.3.3 Exchange-Correlation Functional	25
2.3.4 The Solution of the Kohn-Sham Equations	27
	vii

2.4 Hybridization Functional Method	28
2.5 On-Site Coulomb Repulsion Correction-DFT+U	29
2.6 Computational Methods	30
2.6.1 Simulation Packages	30
2.6.2 Relative Formation Energies	34
2.6.3 Chemical Bonding Properties	35
2.6.4 Electronic Structures	37
References	39
Chapter 3 (0001) Plane Inversion Domain Boundaries in Wurtzite Semiconductors	42
3.1 Introduction	42
3.2 Simulation Method	43
3.3 Energetic Stability	44
3.4 Chemical Bonding and Bader Population Analysis	45
3.5 Electron Structure of IDBs	50
3.5.1 Band Structure	50
3.5.2 Projected Density of States (PDOS)	52
3.6 Conclusion	54
References	55
Chapter 4 Experimental and Theoretical Investigation of the (0001) Plane IDBs at the ZnO/GaN heterointerface	57
4.1 Introduction	57
4.2 Samples	59
4.3 TEM Observation	61
4.4 Theoretical Modeling of (0001) Plane IDBs in ZnO/GaN heterostructure	64
4.5 Energetic Stability	64

4.6 Chemical Bonding and Bader Population Analysis	69
4.7 Electronic Structure of IDBs	74
4.8 Conclusion	76
References	77
Chapter 5 [0001] Tilt Grain Boundaries in ZnO Semiconductor	82
5.1 Introduction	82
5.2 Topological Analysis of GBs in Wurtzite Symmetry	84
5.3 Methodology	88
5.3.1 Experimental Procedures	88
5.3.2 Computational Details	89
5.4 The Atomic Structure of the $[10\bar{1}0]$ Edge Dislocation	91
5.4.1 The $[10\bar{1}0]$ Edge Dislocation in GaN	92
5.4.2 The $[10\bar{1}0]$ Edge Dislocation in ZnO	94
5.5 Electronic Properties of GBs	103
5.6 Conclusion	105
References	106
Chapter 6 General Conclusion and Perspective	110
6.1 General Conclusion	110
6.2 Perspective	111

# Chapter 1

## Wurtzite Semiconductors

The group III-nitrides and ZnO semiconductors have attracted a great deal of attentions due to their prominent properties such as large direct band gaps (GaN, AlN and ZnO) and high exciton binding energy (~60 meV in ZnO) which have applications in optoelectronic and electronic fields. In this chapter, basic properties encompassing crystallography, elastic constants, polarity, electronic properties, crystal growth, as well as crystal defects are briefly introduced.

### 1.1 Crystal Structure and Related Properties

#### 1.1.1 Crystal Structure

AlN, GaN, InN and ZnO are the most stable in wurtzite (WZ) structure at ambient conditions. In this structure, the atoms occupy tetrahedral sites with each atom bonded to four neighbors of the other atomic species. The respective topology is shown in Figure 1.1 [1]. The unit cell consists of two interpenetrating hexagonal close packed sublattices, in which one of the sublattices is shifted along the c-axis by a relative displacement of  $u$  in fractional coordinates (seen in Figure 1.1(a)). In an ideal WZ crystal, the two lattice constants,  $a$  and  $c$ , are related by  $\frac{c}{a} = \sqrt{8/3} = 1.633$  and the internal parameter  $u$  equals to  $3/8=0.375$ . The side view of Figure 1.1(b) indicates a stacking sequence of -AaBbAaBb- along the [0001] axis.

The dashed lines in side view of Figure 1.1(b) denote the projected positions (A or B sites) along [0001] direction. Due to the different ionicities (ionic radii) of the cations respect to the anions, the group III-nitrides and ZnO exhibit various lattice parameters. Table 1.1 gathers a set of lattice parameters:  $c/a$  ratio and  $u$  parameter for AlN, GaN, InN and ZnO either from experiments or from theoretical calculations. As can be seen,



the  $c/a$  ratios and  $u$  parameters slightly vary from the ideal values of 1.633 and 0.375, which depends on the atom sizes.

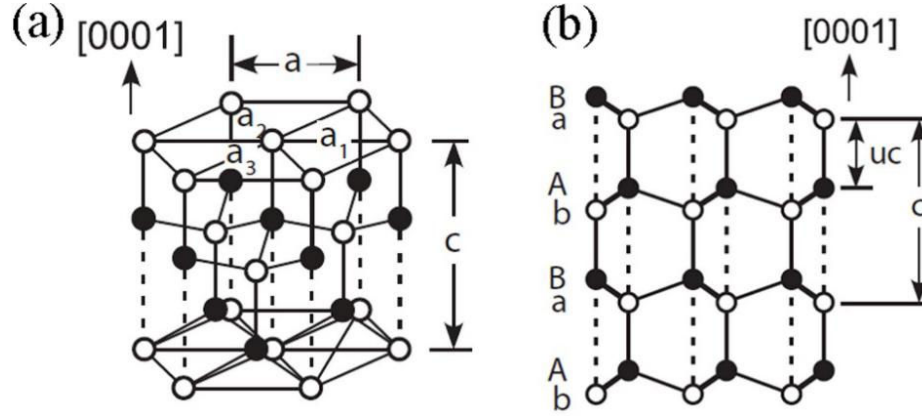


**Figure 1.1.** Topology of wurtzite crystal including stick-ball model (a) and side view (b) presentations. Solid and hollow dots represent the cation and anion. Atomic stacking sequence is shown aside [1].

**Table 1.1** Lattice parameters  $a$ ,  $c$  (Å), internal parameter  $u$ , as well as  $c/a$  ratio of WZ structure for the group III-nitrides and ZnO semiconductors.

	$a$ (Å)	$c$ (Å)	$u$	$c/a$
AlN	3.112 <sup>a</sup>	4.983 <sup>a</sup>	0.380 <sup>b</sup>	1.601
GaN	3.189 <sup>a</sup>	5.185 <sup>a</sup>	0.376 <sup>b</sup>	1.626
InN	3.545 <sup>a</sup>	5.703 <sup>a</sup>	0.377 <sup>b</sup>	1.609
ZnO	3.250 <sup>c</sup>	5.204 <sup>c</sup>	0.382 <sup>c</sup>	1.602

<sup>a</sup>From [2]

<sup>b</sup>From [3]

<sup>c</sup>From [4]

### 1.1.2 Elastic Strain

The elasticity of the solid allows the material to deform under the external force induced by impurities, lattice mismatch etc., and completely recovers its initial state with removal of the stress. The lattice deformation induced by the stress is called strain. The relationship between the stress  $\sigma$  and the strain  $\epsilon$  is defined by the generalized Hook's law [5]:

$$\sigma_{ij} = C_{ijkl}\epsilon_{kl} \quad (1.1)$$

where  $C_{ijkl}$  is the elastic stiffness coefficient related to stress tensor  $\sigma_{ij}$  and strain tensor  $\epsilon_{kl}$ . With hexagonal symmetry, five independent elastic stiffness constants:  $C_{11}$ ,  $C_{12}$ ,  $C_{13}$ ,  $C_{33}$  and  $C_{44}$  are included to simplify the matrix as:

$$\begin{pmatrix} \sigma_1 \\ \sigma_2 \\ \sigma_3 \\ \sigma_4 \\ \sigma_5 \\ \sigma_6 \end{pmatrix} = \begin{pmatrix} C_{11} & C_{12} & C_{12} & 0 & 0 & 0 \\ C_{12} & C_{11} & C_{12} & 0 & 0 & 0 \\ C_{12} & C_{12} & C_{11} & 0 & 0 & 0 \\ 0 & 0 & 0 & C_{44} & 0 & 0 \\ 0 & 0 & 0 & 0 & C_{44} & 0 \\ 0 & 0 & 0 & 0 & 0 & C_{66} \end{pmatrix} \cdot \begin{pmatrix} \epsilon_1 \\ \epsilon_2 \\ \epsilon_3 \\ \epsilon_4 \\ \epsilon_5 \\ \epsilon_6 \end{pmatrix} \quad (1.2)$$

where the Voigt notation is employed:  $xx \rightarrow 1$ ,  $yy \rightarrow 2$ ,  $zz \rightarrow 3$ ,  $yz, zy \rightarrow 4$ ,  $xz, zx \rightarrow 5$ ,  $xy, yx \rightarrow 6$ . In the matrix, x, y, z-axes are parallel to the orthogonal crystal axis  $[2\bar{1}\bar{1}0]$ ,  $[01\bar{1}0]$  and  $[0001]$ , respectively And  $C_{66}$  equals to  $(C_{11} - C_{12})/2$ . In most cases including wurtzite single crystal, the elastic constants are evaluated by measuring the velocity of sound after applying the transverse and longitudinal waves along the c axis and any axis perpendicular to it [5], table 1.2 reports elastic constants taken from the literature.

**Table 1.2** Elastic constants of the group III-nitrides and ZnO compounds (GPa).

WZ	C <sub>11</sub>	C <sub>12</sub>	C <sub>13</sub>	C <sub>33</sub>	C <sub>44</sub>
AlN <sup>a</sup>	396	137	108	373	116
GaN <sup>b</sup>	390	145	106	398	105
InN <sup>a</sup>	223	115	92	224	48
ZnO <sup>c</sup>	209.7	121.1	105.1	210.9	42.5

<sup>a</sup>From [6]

<sup>b</sup>From [7]

<sup>c</sup>From [8]

### 1.1.3 Polarity

The wurtzite structure (space group: P6<sub>3</sub>mc) does not have a center of symmetry along the [0001] direction (Fig. 1.2). So that a crystal film grown along this direction is polar. By convention, the positive polarity [0001] has been defined as when the c axis is pointing from the cation to the anion.

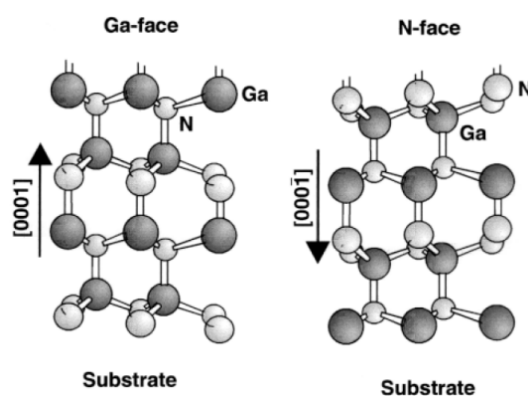


**Figure 1.2.** The polarity lay out in wurtzite, the case of GaN [1].

The polarity of group III-nitrides and ZnO has a marked influence on material growth and electronic properties. For instance, as reported in experiments, the growth of GaN along the [0001] direction leads to layers with smooth surfaces, whereas they can be

rough on top of the N-face [9]. The results are similar with the growth of ZnO films [10]. As for the influence on electronic properties, the most typical application refers to high electron mobility transistors (HEMTs) in which a two-dimensional electron gas (2DEG) can be obtained at heterointerfaces without the need of doping like in cubic semiconductors [11]. Without considering external fields, the macroscopic polarization is given as a sum of spontaneous polarization  $P^{SP}$  in equilibrium condition and strain generated piezoelectric polarization  $P^{PE}$  as:

$$P = P^{SP} + P^{PE} \quad (1.3)$$

In the following section, the determination and derivation of spontaneous and piezoelectric polarization are briefly introduced.

## Spontaneous Polarization

Spontaneous polarization of group III-nitrides and ZnO wurtzite semiconductors directly results from the absence of inversion symmetry along the c axis. Figure 1.3 shows the diagram of dipole moments in wurtzite GaN. Due to the difference of electronegativities between Ga and N atoms, Ga-N bond is polarized with a dipole moment of  $P_0$  pointing from N to Ga. The asymmetry along the c axis leads to a permanent dipole moment along the [0001] direction, named as spontaneous polarization  $P^{SP}$ . The absolute value of spontaneous polarization is unknown and can only be calculated as a relative value with respect to an “unstrained” material reference like zinc-blend structure. Table 1.3 lists the values of spontaneous polarization from Ref.[12]. It is worth noting that the reference structure must have ideal values of  $c/a=1.633$  and  $u=0.375$ . As the real lattice parameters can be distorted through small deviations, the obtained polarization values are sensitive to the lattice parameters used in the calculations.

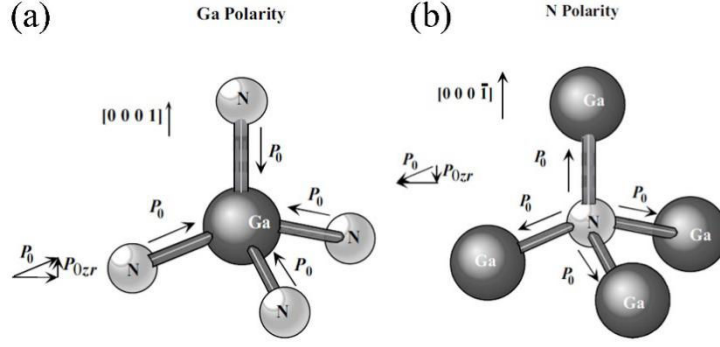


**Figure 1.3.** Ball-and-stick diagram of the tetrahedral bonding in wurtzite GaN for Ga- (a) and N-polarity (b) configuration, respectively. The dipole moments of polarized Ga-N bond are shown.

## Piezoelectric Polarization

Apart from the spontaneous polarization, the strain induced or piezoelectric polarization  $P^{PE}$  has also important influence on electronic properties of the group III-nitrides and ZnO compounds. Similar with the elastic stress, in the linear regime, the piezoelectric polarization is approximatively given as a linear function of elastic strain by:

$$P_i^{PE} = e_{ijk} \varepsilon_{jk} \quad (1.4)$$

In hexagonal symmetry, the three non-vanishing and independent piezoelectric constants are:  $e_{33}$ ,  $e_{13}$ ,  $e_{15}$ . The piezoelectric polarization components along the three axes can be deduced as:

$$P_1^{PE} = e_{15} \varepsilon_5 \quad (1.5)$$

$$P_2^{PE} = e_{15} \varepsilon_4 \quad (1.6)$$

$$P_3^{PE} = e_{31}(\varepsilon_1 + \varepsilon_2) + e_{33} \varepsilon_3 \quad (1.7)$$

The coefficient  $\varepsilon_3$  denotes the strain along the c-axis and is expressed as  $\varepsilon_3 = (c - c_0)/c_0$ . As the in-plane strain in (0001) plane is biaxial,  $\varepsilon_1 = \varepsilon_2 = (a - a_0)/a_0$ ,  $c_0$  and  $a_0$  are the equilibrium lattice constants of WZ structure. Based on Berry phase approach

[13], Bernardini and Fiorentini [12] calculated the polarization constants for all group III-nitrides and compared the results with the conventional III-V and II-VI compounds. Table 1.3 collects the calculated spontaneous polarization and the piezoelectric constants for our compounds using the set of lattice parameters from Ref. 12. The spontaneous polarization has negative sign and increases from GaN over InN to AlN. In particular, the piezoelectric response of AlN is comparable to that of ZnO which is reported to possess the highest piezoelectric polarization among the tetrahedrally bonded compounds.

In case of biaxial strain, the lattice parameters  $a$  and  $c$  in hexagonal symmetry have the relationship:

$$\frac{c-c_0}{c_0} = -2 \frac{c_{13}}{c_{33}} \frac{a-a_0}{a_0} \quad (1.8)$$

The piezoelectric polarization along  $c$  axis in Eq.(1.7) is then determined by:

$$P_3^{PE} = 2 \frac{a-a_0}{a_0} (e_{31} - e_{33} \frac{c_{13}}{c_{33}}) \quad (1.9)$$

From the piezoelectric constants tabulated in Table 1.3,  $(e_{31} - e_{33} \frac{c_{13}}{c_{33}}) < 0$ , therefore, the piezoelectric polarization is negative for tensile strain and positive for compressive strain, respectively.

The polarization induced interfacial sheet charge density is given as the change of polarization between the lower and the upper layer:

$$\begin{aligned} \sigma &= P_{Lower} - P_{Upper} \\ &= (P_{Lower}^{SP} + P_{Lower}^{PE}) - (P_{Upper}^{SP} + P_{Upper}^{PE}) \quad (1.10) \end{aligned}$$

If the charge density  $\sigma$  is positive, electrons will accumulate at the interface region to form a so-called two-dimensional electron gas (2DEG); but if  $\sigma$  is negative, a 2-

dimensional hole gas (2DHG) takes place at the interface.

**Table 1.3** Theoretical results of spontaneous polarization and the piezoelectric coefficients for the group III-nitrides and ZnO. The values are given in ( $C/m^2$ ).

Ref.[12]	$P^{SP}$	$e_{33}$	$e_{31}$
AlN	-0.081	1.46	-0.60
GaN	-0.029	0.73	-0.49
InN	-0.032	0.97	-0.57
ZnO	-0.057	0.89	-0.51

## 1.2 Growth Techniques

In this section, a few growth methods are reviewed with a particular attention focused on the plasma-induced molecular beam epitaxy (PIMBE) and magnetron sputtering that have been used to grow our samples.

### 1.2.1 Substrates

The foreign substrates are necessary for obtaining high quality layers in case no bulk material is available at an affordable price. Due mostly to the large availability and symmetry compatibility, as well as moderate thermal expansion mismatch, silicon [14] and silicon carbide (SiC) [15] and sapphire ( $\alpha$ -Al<sub>2</sub>O<sub>3</sub>) [16] are the most popular substrates used to grow group III-nitrides and ZnO. Besides, the heteroepitaxy of ZnO on GaN can be used to yield a better performance. The combination of GaN and ZnO is stimulated by the moderate lattice mismatch ( $\sim 2.1\%$ ) between the two materials, but also mainly due to the unavailability of stable and reproducible p-type doping of ZnO. With the growth of p-GaN/n-ZnO heterojunction applications for light emission may

be foreseen [17].

### 1.2.2 Plasma-Induced Molecular Beam Epitaxy (PIMBE)

MBE is one of the main methods to grow thin films of semiconductors, insulators as well as metals [18]. It offers precise control of growth rate within one monolayer which is interesting for achieving sharp interface for an accurate tuning of the properties. Different from the metalorganic chemical vapour deposition (MOCVD) which operates under the thermodynamical equilibrium and mostly relies on diffusion process, MBE uses impinging beams reaction on the substrate surface [19].

Figure 1.4 shows a diagram of MBE chamber. For group III-nitrides or ZnO film growth, as reported by Moustakas et al. [20], an electron cyclotron resonance (ECR) may be mounted in the metal effusion cell port to evaporate the atoms; Nitrogen flux is provided via a compact plasma source or second ECR. Through the process, the strong triple bond between two nitrogen atoms in N<sub>2</sub> is dissociated [21-23] to produce the chemically reactive nitrogen radicals under reduced pressure. Thus, the group III-nitrides and ZnO grow by the synergetic effects of the evaporation of metal resource from the effusion cell and the plasma produced nonmetal radical flux.

The MBE growth process follows the three steps: 1) surface cleaning. In the used ultrahigh vacuum, the substrate is first exposed to a nitrogen plasma in order to remove the residual impurities. Taking the ZnO/GaN as an example, GaN substrate surface is pre-exposed to a Zn flux to saturate or remove the Ga top atomic layer. 2) Lower temperature nucleation growth. In this case a ZnO nucleation layer of 25 nm thickness is deposited at 300°C. 3) Finally, a high temperature up to 670°C is adopted to perform an epitaxial growth of ZnO. During the film growth stage, by varying the ratio of metal or nonmetal flux, the speed of step flow growth, surface's morphology, as well as the polarity can be well controlled.



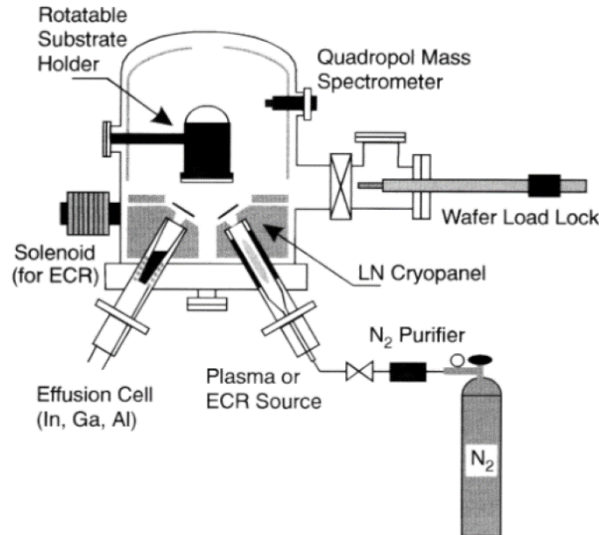


**Figure 1.4.** Schematics of a molecular beam epitaxy chamber. A Plasma or ECR source is used to generate chemically active nitrogen atoms [24].

### 1.2.3 Plasma-Assisted Sputtering

Modern Plasma assisted sputtering is based on a plasma which is generated between a target and the substrate at low pressure using a closed magnetic field at 13.56 MHz. In this process, a pre-sputtering process is needed in order to remove the contamination on the target material surface. A mixture of nitrogen and argon is utilized to serve as the N-resource and sputtering gas. Figure 1.5 schematically exhibits the work principle of magnetron sputtering. The positively charged ions from the plasma are accelerated by an electrical field superimposed on the negatively charged electrode or “target” with a potential range from few hundred to few thousand electron volts, and strike the negative electrode until the atoms are ejected from the target material. Those dislodged metal atoms will condense on the top of the substrate which is in proximity to the sputtering cathode. The substrate holder is rotatable and we could place the substrate above either sputtering source to allow for the sequential deposition required for bilayer and multilayer films. The obtained films by sputtering are in general polycrystalline or columnar, we shall investigate the atomic structure of their boundaries in chapter 5.

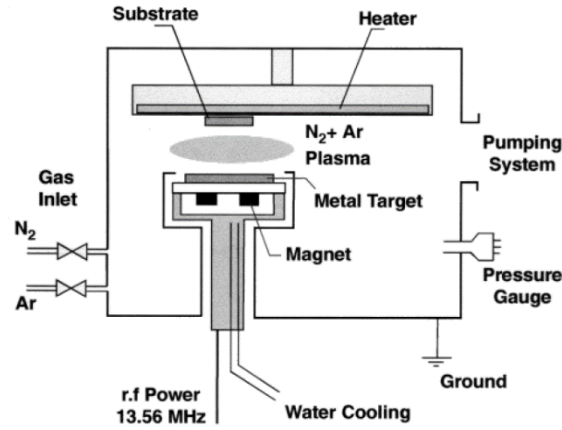


**Figure 1.5.** Diagram of magnetron sputtering system: the source is a target made of the material to be deposited [24].

### 1.3 Extended Defects

The materials under study are grown on foreign substrates such as  $\text{Al}_2\text{O}_3$  and  $\text{SiC}$  which generates a high density of structural defects (up to  $10^{10} \text{ cm}^{-2}$ ) [25,26] due to the mismatch of lattice parameters and expansion coefficients. There is a great need for investigating the crystal defects since they can degrade the electronic and mechanical properties of the material, with a highly detrimental effect on device performance. This work focuses on two kinds of planar defects: the (0001) plane inversion domain boundary (IDB) and the [0001] tilt GBs in ZnO through investigation within a close combination of high-resolution TEM observations and theoretical modelling.

#### 1.3.1 Inversion Domain Boundaries (IDBs)

The reports on the polarity control of wurtzite layers along the  $c$  axis displays a number of controversial conclusions. For example, Xia et al. [27] have reported that low growth temperature ( $<500^\circ\text{C}$ ) and Ga-rich condition lead to a Ga-polar GaN based on O face ZnO; whereas, N-polar GaN can be achieved on O face ZnO by using high growth temperature and low III/V ratio. However, Ohgaki et al. [28] have pointed out that the polarity inverted GaN epilayer based on O face ZnO mainly comes from the very thin interfacial layer of  $\text{Ga}_2\text{O}_3$ .

The IDB is a planar interface between two parts of a crystalline material which are connected by a polarity reversal. It was first reported by Aminoff and Broom in wurtzite ZnO [29], however other terms have also been used to name the same defect such as inversion twins [30], antistructure or antiphase boundaries (APB) [31,32]. Up to now extensive atomic structure and properties investigations have been carried out on the  $\{10\bar{1}0\}$  prismatic IDBs. Four models of  $\{10\bar{1}0\}$  IDBs have been reported in the literature. Austerman et al. have proposed two models [30] obtained by keeping the anion (cation) sublattice continuous when crossing the boundary, whereas the cation (anion) sublattice switch to an equivalent tetrahedral site for the polarity reversal. The Holt IDB model [33], as shown in Figure 1.6 (a), is a pure inversion operation across the boundary, it exhibits wrong bonds inside the boundary plane. This kind of structure has been reported to be energetically unfavorable [34], it may change to a more stable configuration through a translation of  $1/2[0001]$ , as shown in Figure 1.6(b).

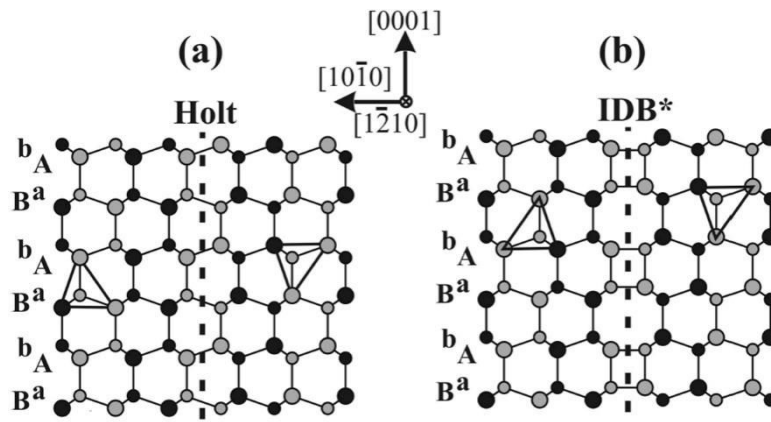


**Figure 1.6.**  $[11\bar{2}0]$  projections of (a) Holt IDB and (b) IDB\* models. Large (cation) and small (anion) circles represent the different elements. The wurtzite stacking sequence of -ABAB- is shown on the left side [33].

For the (0001) IDB, Kim and Goo [35] have reported a TEM observation on the “pure” (0001) plane IDB structure and proposed eight geometrical models. Their projections along the  $[11\bar{2}0]$  direction are exhibited in Figure 1.7 using their notation, where H stands for head to head and T for tail to tail. As can be seen, H1 and H4 IDBs exhibit similar structural features: a metal atomic layer locates at octahedral position sharing six nearest neighbor nonmetallic atoms at the interface, which in turn bond to the adjacent layer of tetrahedrally coordinated metal atoms. The difference between H1 and H4 IDB comes from the adjacent atomic bi-layer which shifting from Bb location in H1 to Aa in H4. In H2 and H3 IDBs, an aligned metal-nonmetal-metal atomic arrangement is shown: the nonmetal atomic layer at interface bonds to two metal layers with an angle of  $180^\circ$  in deviation of tetrahedral occupation. As for the T IDBs, the interface is made of a nonmetallic atomic layer where each atom is surrounded by six nearest metal atoms occupying tetrahedral sites. The corresponding displacement vectors are given in Table 1.4.

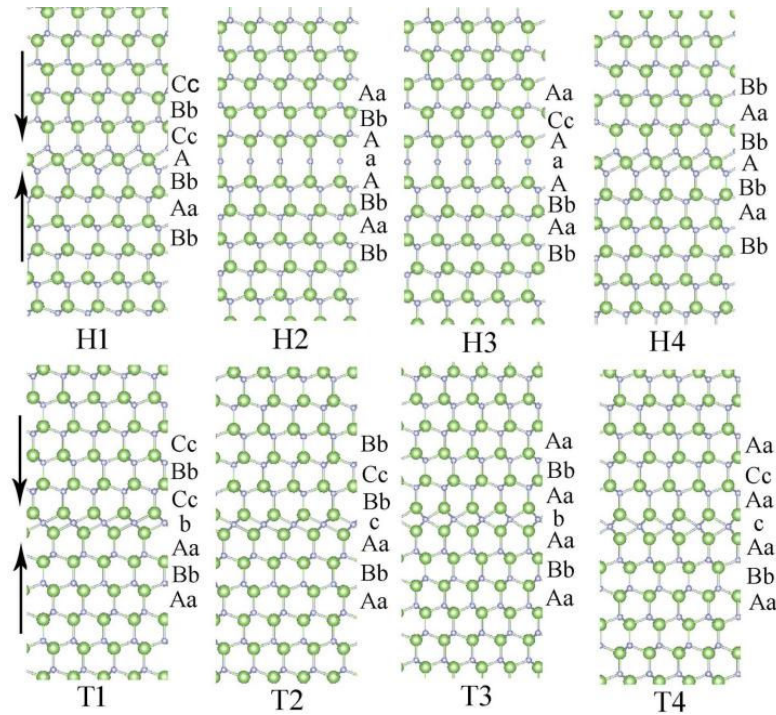


**Figure 1.7.** Atomic structures of the eight (0001) plane IDBs projected along the  $[11\bar{2}0]$  direction. The green and blue balls represent metal and nonmetal atoms, respectively. The arrows indicate the polarity.

**Table 1.4** The stacking sequences and displacement vectors of models in Figure 1.7.

Models	Stakings	Displacement vector
H1	AaBbA-cCbBc	$1/3[0\bar{1}10]$
H2	AaBbA-aAbBa	0
H3	AaBbA-aAcCa	$1/3[0\bar{1}10]$
H4	AaBbA-cCaAc	$1/3[0\bar{1}10]$
T1	AbBaA-bAaBb	$1/3[0\bar{1}10]$
T2	AbBaA-cBbCc	$1/3[0\bar{1}10]$
T3	AbBaA-bAaBb	0
T4	AbBaA-cAaCc	$1/3[0\bar{1}10]$

### 1.3.2 Grain Boundaries (GBs)

A GB is a more complex interface which connects two adjacent crystals of the same material, where the acting symmetry element may be a combination of more than one operation. It always involves a rotation which does not belong to the symmetry group of the crystal. When it results from a pure rotation (Figure 1.8), it can be represented by  $\theta^\circ[h_{\vec{o}}, k_{\vec{o}}, l_{\vec{o}}], (h_{\vec{n}_A}, k_{\vec{n}_A}, l_{\vec{n}_A})$ , the rotation thus takes place around a common axis  $\vec{o} = [h_{\vec{o}}, k_{\vec{o}}, l_{\vec{o}}]$  and  $\theta^\circ$  is the rotation angle. It is simpler to refer to the boundary plane using the coordinates of one of the grains  $(h_{\vec{n}_A}, k_{\vec{n}_A}, l_{\vec{n}_A})$ .

Depending on the angle between the rotation axis  $\vec{o}$  and the boundary plane normal vector  $\vec{n}$ , grain boundaries are tilt GBs ( $\vec{o} \perp \vec{n}$ ), twist GBs ( $\vec{o} \parallel \vec{n}$ ), or of mixed grain type [37]. Moreover, they are also termed as low-angle ( $<15^\circ$ ) and high-angle ( $>15^\circ$ ) GBs according to the value of rotation angle  $\theta$ .

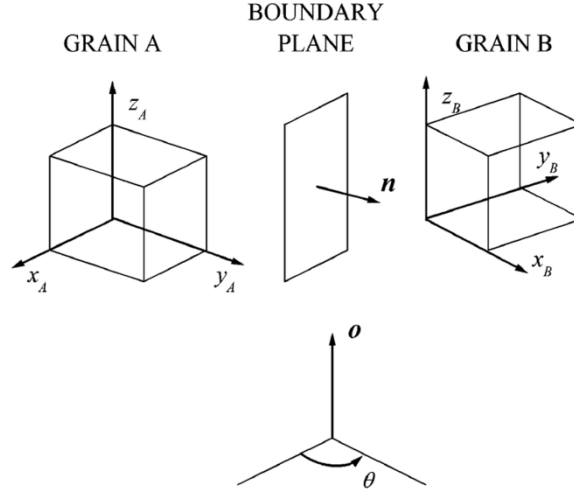


**Figure 1.8.** In a pure rotation grain boundary,  $x_A$ - $z_A$  and  $x_B$ - $z_B$  are the basis vectors of grains A and B. Boundary plane is determined by its normal vector  $\vec{n}$ . The connecting operation between two grains is a rotation of angle  $\theta$  around the direction  $\vec{o}$  [36].

## Coincidence-Site Lattice (CSL) Model

The coincidence-site lattice model for the GBs was proposed by Kronberg and Wilson [38] in an attempt to describe the atomic structure of the boundaries. In this formalism, the lattices are artificially interpenetrated and one of them is rotated around the  $\vec{o}$  axis by  $\theta$ . The results is that for specific angles, sites of the two lattice coincide, which lead to the as-called coincidence-site lattice (CSL). Indeed, it is understandable that the low energy GBs correspond to the highest density coincidence of the two grains and the density of the coincidence site,  $\Sigma$ , was adopted to denominate the grain boundaries as:

$$\Sigma = \frac{\text{Volume of unitcell in CSL}}{\text{Volume of unitcell}} \quad (1.11)$$

Subsequently, the formalism of dichromatic complexes proposed by Pond and Vlachavas [39] is used to determine symmetry operations common to the two grains. In hexagonal symmetry, the rotation angle of  $\theta$  is identical with  $(60^\circ - \theta)$  around the tilt axis of [0001]. As can be seen in Figure 1.9, two misoriented grains are designed as black ( $\mu$ ) and white ( $\lambda$ ), the coincident sites are clearly visible in the overlap region of two crystals with the periodic unit cell shown by ABDC. Thus, the density of the

coincidence site is given as:

$$\Sigma = \frac{S_{ABDC}}{S_{\mu}} \quad (1.12)$$

Using  $\mu$  as the reference crystal,  $AB = -3a_3 + a_2$ ,  $AC = a_3 + 4a_2$ , thus  $S_{ABDC} = AB \times AC = 13|a_3 \times a_2|$ ; applying to Eq.(1.12), the Sigma value can be obtained as:

$$\Sigma = \frac{13|a_3 \times a_2|}{a_3 \times a_2} = 13 \quad (1.13)$$

Therefore, the grain boundary in Figure 1.9 can also be recognized as  $\Sigma 13$  [0001] tilt GB. The GB is periodic with coincidence sites connected by structural defects [40]. These defects are called the primary dislocations of the grain boundary, they are found through the usual Burgers circuits which enclose one period and travel from  $\mu$  to  $\lambda$  crystal. When such circuits are mapped into the  $\lambda$  or  $\mu$  crystal, a unique defect content is obtained which correspond to such a dislocation.

For  $\Sigma 13$  GB in Figure 1.9, for the side of CSL unit cell AB  $\{\bar{4}, 1, 3, 0\}$ , the Burgers circuit is exhibited as SXF ( $C_{\mu} = -3a_3 + a_2$ ,  $C_{\lambda} = a_3 - 3a_2$ ). When mapping this Burgers circuit in  $\lambda$  crystal, an **a** edge dislocation core with the defect content of  $-2a_{1\lambda}$  is obtained. Similarly for the diagonal of CSL, unit cell BC  $\{\bar{5}, 2, 7, 0\}$  boundary, the defect content comes out as  $F'S'=2(a_3-a_1)_{\lambda}$ .

Equipped with the basic topology above, the type and the Burgers vector of the defect content can be directly determined. Their defect core structure can be identified further by high-resolution TEM and atomic modelling.

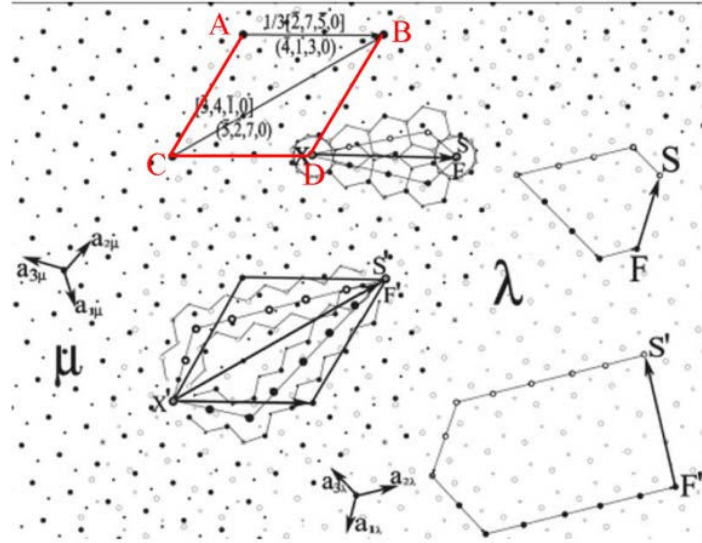


**Figure 1.9.** Dichromatic complex of the CSL for  $\Sigma 13$  GB at  $32.2^\circ$ . A superposition of sublattices  $\mu$  and  $\lambda$  is shown. The Burgers circuits for the side AB  $\{\bar{4}, 1, 3, 0\}$  and diagonal BC  $\{\bar{5}, 2, 7, 0\}$  boundaries are mapped in crystal  $\lambda$ . The rotation axis is along  $[0001]$  direction [40]

## References

- [1] T. Hanada, Basic Properties of ZnO, GaN, and Related Materials, in: T. Yao and S-K Hong (Eds.), Oxide and Nitride Semiconductors, Springer Verlag, pp.1-18.
- [2] I. Vurgaftman, J.R. Meyer, J. Appl. Phys. 94, 3675 (2003).
- [3] F. Bernardini, V. Fiorentini, D. Vanderbilt, Phys. Rev. B 56, R10024 (1997)
- [4] H. Karzel, W. Potzel, M. Köfferlein, W. Schiessl, M. Steiner, U. Hiller, G.M. Kalvius, D.W. Mitchell, T.P. Das, P. Blaha, K. Schwarz and M.P. Pasternak, Physical Review B: Condensed Matter, 53, 11425 (1996).
- [5] M. Levy, Introduction to fundamentals of elastic constants, in: M. Levy, H. Bass and R. Stern (Eds.), Handbook of Elastic Properties of Solids, Liquids, and Gases, pp: 1-35.
- [6] A.F. Wright, J. Appl. Phys. 82, 2833 (1997).
- [7] A. Polian, M. Grimsditch, I. Grzegory, J. Appl. Phys. 79, 3343 (1996).
- [8] T.B. Bateman, J. Appl. Phys. 33, 3309 (1962).
- [9] F.A. Ponce, D.P. Bour, W.T. Young, M. Saunders and J.W. Steeds, Appl. Phys. Lett. 69, 337 (1996).



- [10] M.B. Ullah, V. Avrutin, S.Q. Li, S. Das, M. Monavarian, M. Toporkov, Ü. Özgür, P. Ruterana and H. Morkoç, *Phys. Status Solidi RRL*. 10, 682 (2016).
- [11] O Ambacher, B. Foutz, J. Smart, J.R. Shealy, N.G. Wermann, K. Chu, M. Murphy, A.J. Sierakowski, W.J. Schaff and L.F. Eastman, *J. Appl. Phys.* 87, 334 (2000).
- [12] F. Bernardini and V. Fiorentini, *Phys. Rev. B* 56 R10024 (1997).
- [13] R.D. King-Smith and D. Vanderbilt, *Phys. Rev. B* 47, 1651 (1993).
- [14] S. Keller, Y. Dora, F. Wu, X. Chen, S. Chowdhury, S.P. DenBaars, J.S. Speck, and U.K. Mishra, *Appl. Phys. Lett.* 97, 142109 (2010).
- [15] S. Keller, N. Fichtenbaum, F. Wu, G. Lee, S.P. DenBaars, J.S. Speck, and U.K. Mishra, *Jpn. J. Appl. Phys., Part 2* 45, L322 (2006).
- [16] S. Keller, N.A. Fichtenbaum, F. Wu, D. Brown, A. Rosales, S.P. DenBaars, J.S. Speck, and U.K. Mishra, *J. Appl. Phys.* 102, 083546 (2007).
- [17] D.J. Rogers, F. Hosseini Teherani, A. Yasan, K. Minder, P. Kung, and M. Razeghi, *Appl. Phys. Lett.* 88, 141918 (2006)
- [18] H. Okumura, M. Shimizu, X. Q. Shen and T. Ide, *Current Applied Physics* 2, 305-310 (2002).
- [19] M.A. Herman and H. Sitter, *Molecular Beam Epitaxy*, Springer Series in Materials Science ed M B Panish (New York: Springer) 1989
- [20] T.D. Moustakas, T. Lei and R.J. Molnar, *Physica B* 185, 39 (1993).
- [21] K.R. Jennings and J.W. Linnet, *Quart. Rev.* 12, 116 (1958).
- [22] G.G. Manella, *Chem. Rev.* 63, 1 (1963).
- [23] Brown C R and Winkler C A 1970 *Angew. Chem.* 82 187.
- [24] O Ambacher, *J. Phys. D: Appl. Phys.* 31, 2653 (1998).
- [25] H. Angerer, O. Ambacher, R. Dimitrov, T. Metzger, W. Rieger and M. Stutzmann, *Mater. Res. Soc. Inter. J. Nit. Semi. Res.* 1, 15 (1996).
- [26] S.D. Lester, F.A. Ponce, M.G. Craford and D.A. Steigerwald *Applied Physics Letters* 66, 1249 (1995).
- [27] Y. Xia, J. Brault, P. Vennegues, M. Nemoz, M. Teisseire, M. Leroux and J.M. Chauveau, *J. Cryst. Growth.* 388, 35 (2014).
- [28] T. Ohgaki, *J. Ceram. Soc. Jpn.* 117, 475 (2009).

- [29] G. Aminoff, G. Broome, Strukturtheoretische Studien über Zwillinge, Z. Krist. 80, 355 (1931).
- [30] S.B. Austerman and W.G. Gehman, J. Mater. Sci., 1, 249 (1966).
- [31] H. Blank, P. Delavignette, R. Gevers and S. Amelinckx, Phys. Stat. Sol. 7, 747 (1964).
- [32] D.B. Holt, J. Phys. Chem. Solids, 30, 1297 (1969).
- [33] J. Kioseoglou, G.P. Dimitrakopoulos, P. Komninou, H.M. Polatoglou, A. Serra, A. Béré, G. Nouet, and T. Karakostas, Phys. Rev. B 70, 115331 (2004).
- [34] Y.F. Yan and M.M. Al-Jassim, Phys Rev B 69, 085204 (2004).
- [35] J.C. Kim and E. Goo, J. Am. Ceram. Soc., 73, 877 (1990).
- [36] P. Lejcek, Grain Boundaries: Description, Structure and Thermodynamics in: R.Hull, C. Jagadish, R.M. Osgood, J. J. Parisi, Z.Wang, H.Warlimont (Eds.), Grain Boundary Segregation in Metals, Springer Heidelberg Dordrecht London New York.
- [37] A.P. Sutton, R.W. Balluffi, Interfaces in Crystalline Materials (Clarendon Press, Oxford, 1995).
- [38] M.L. Kronberg, F.H. Wilson, Trans. AIME. 185, 501 (1949)
- [39] R. C. Pond and D. S. Vlachavas, Proc. R. Soc. London, Ser. A 386, 95 (1983).
- [40] P. Ruterana, M. Abouzaid, A. Bere and J. Chen, J. Appl. Phys. 103, 033501 (2008).

## Chapter 2

### Density Functional Theory and Application Techniques

During the last decades, the density functional theory (DFT) has been an important approach to understand the properties of matter down to the level of individual atoms. All material are many-body systems of electrons and nuclei, and their physical and chemical properties are governed by the Schrödinger equation. Therefore, many simulation packages have been developed to help for its resolution and access to the materials properties, for instance: CASTEP [1], ABINIT [2], VASP [3-6], SIESTA [7], Quantum ESPRESSO [8-9], ... In this work, the VASP package was adopted to deal with the simulation of (0001) plane IDBs because of the relative small scale system (around 40 atoms). However, the SIESTA package based on norm-conserving pseudopotential was used to treat the GB simulation that needs a larger number of atoms (more than 100 atoms).

In the following, the basic framework of DFT is briefly reviewed followed by an introduction of the used software packages.

#### 2.1 Schrödinger Equation

The Schrödinger Equation allows describing the stability of any system down to the atomic level throughout the movements of the constituents.

$$\hat{H}\Psi(r, R) = E\Psi(r, R) \quad (2.1)$$

where  $\hat{H}$  is the Hamiltonian operator.  $\psi$  is the wave function of system, it is a function of the spatial coordinates of N electrons  $r_i$   $\{i=1,2,...N\}$  and M nuclei  $R_A$   $\{A=1,2,...M\}$ . E is the corresponding energy for the system.

The Hamiltonian operator is complex, it concerns the kinetic energies of the nuclei and

the electrons, the interactions between the nuclei and the electrons and their mutual interactions. By taking these interactions into account and avoiding the influence of possible external fields, the Hamiltonian operator,  $\hat{H}$ , can be described as:

$$\hat{H} = \hat{T}_e(r) + \hat{T}_n(R) + \hat{V}_{ee}(r) + \hat{V}_{nn}(R) + \hat{V}_{en}(r, R) \quad (2.2)$$

The five terms in right side define, in order, the kinetic energy operator of electrons  $\hat{T}_e$  and nuclei  $\hat{T}_n$ ; the potential energy operator of electrons  $\hat{V}_{ee}$  and nuclei  $\hat{V}_{nn}$ ;  $\hat{V}_{en}$  is a potential energy operator that describes the interaction between electrons and nuclei. In practice the complex coupling between electrons and nuclei term,  $\hat{V}_{en}(r, R)$ , makes it a strong challenge to solve the Schrödinger Equation. Therefore, further approximations are needed to simplify the Hamiltonian operator and the overall wave function.

## 2.2 Born-Oppenheimer Approximation

The Born-Oppenheimer approximation [10] was introduced to take into account that the mass of a nucleus is much larger than that of the electrons. Therefore, the electrons respond rapidly to the movement of nucleus, but this is not reciprocal. The wave function of the system can thus be decoupled as the product of electron  $\phi(r)$  and nuclei  $\chi(R)$  wave functions:

$$\Psi(r, R) = \phi(r)\chi(R) \quad (2.3)$$

So, instead of considering the overall wave function and energy operator in Schrödinger equation, the problem can be split into two parts: 1) solving the electron-related Schrödinger equation. At this stage, the nuclei are fixed in a certain configuration, thus the electron-related Hamiltonian describes a system of electrons placed in a fixed external potential of nuclei  $\hat{V}_{ext}$  including the  $\hat{V}_{nn}$  electron-nuclei interaction  $\hat{V}_{en}$  term. Therefore, the electron-related Schrödinger equation is given as:

$$[\hat{T}_e + \hat{V}_{ee} + \hat{V}_{ext}]\phi(r) = E_e\phi(r) \quad (2.4)$$

As the nuclei are fixed, by solving the Eq.(2.4), the eigenstate  $\phi(R)$  and eigenvalue

$E_e(R)$  of electrons can be obtained with respect to the positions of nuclei  $R$ . 2) solving the nuclei-related Schrödinger equation based on the eigenstate of electron. Since the movement of nuclei are not affected by electrons, the overall Schrödinger equation (Eq.(2.1) and (2.2)) can be simplified as:

$$[E_e(R) + \hat{T}_n]\chi(R) = E\chi(R) \quad (2.5)$$

By solving this equation, the energy of the whole system can be obtained. Subsequently, taking into account the movement of nuclei, iterative scheme is proceeded from step one to step two, and the ground state energy of the system can be obtained at the end.

Among the process, most of the computer efforts are paid to find the eigenstate of electrons (step one, solution of electron-related Schrödinger equation) since the number of electrons are larger than nuclei and the electronic configuration is complex. Therefore, the electron structure calculation is very expensive and complex. The basic notation is introduced as following.

## 2.3 Density Functional Theory

As mentioned above, the main point turns to solve the electron-related Schrödinger equation Eq.(2.4). Considering the huge number of electrons in a system, it's apparent that the solution of the Eq.(2.4) is still a many-body problem. To further simplify the problem, density of electrons  $n(r)$  is used as the probability of electrons at a set of particular positions  $r_i$  in real space to replace the set of individual electron wave functions. It can be given as:

$$n(r) = 2 \sum_i \phi_i^*(r) \phi_i(r) \quad (2.6)$$

Herein, the term inside the summation is the probability of an electron to be at a specific position  $r$  with a wave function  $\phi_i(r)$ ; the summation goes over all the individual electron wave functions that occupied by electrons. The factor of 2 is induced by the

Pauli exclusion principle. Use of the electron density has turned the 3N-dimensional full wave function solution of Schrödinger equation into a 3-dimensional solution which possesses only three coordinates. Besides, the electron density is physically observable and experimentally measurable [11-14].

### 2.3.1 The Hohenberg-Kohn Theorems

The entire density functional theory is established based on the two theorems proposed by Hohenberg and Kohn in 1964 [15], which apply to any system consisting of electrons moving in an external potential  $\hat{V}_{ext}(r)$ .

**Theorem 1:** The external potential is a unique functional of the electron density. Thus the Hamiltonian, and hence all ground state properties, are determined solely by the electron density.

The total energy of the system can be written as:

$$E_{tot}[n(r)] = F[n(r)] + \hat{V}_{ext}[n(r)] = F[n(r)] + \int dr n(r) v_{ext}(r) \quad (2.7)$$

Where  $F[n(r)]$  is a universal functional of the electron density independent of the external potential which describes the electronic kinetics and electronic exchange-correlation interaction energies.

**Theorem 2:** The ground state energy can be obtained variationally: the density that minimizes the total energy is the exact ground state density.

Therefore, for a N electrons system within an external potential  $V[r]$  with a ground state of  $E_0$  the total energy is constrained to the inequality:

$$E_V[n(r)] \geq E_0 \quad (2.8)$$

Thus, the Hohenberg-Kohn Theorems point out that the total energy of the system is a functional of electron density and the full solution of the Schrödinger equation can be

obtained by minimization of the system total energy. However, in practice, the system is made of an ensemble of electrons in interaction. And the contribution of electronic exchange-correlation energies to the universal functional  $F[n(r)]$  needs to be further defined through various approximations.

### 2.3.2 The Kohn-Sham Equations

Subsequent to the Hohenberg-Kohn theorems, Kohn and Sham [16] proposed to map the fully interacting system of N-electrons onto a fictitious auxiliary system of N non-interacting electrons moving within an effective Kohn-Sham single-particle potential,  $\hat{V}_{KS}[n]$  and provided the Hamiltonian operator of the system as:

$$\begin{aligned}\hat{H} &= \hat{T}_s[n] + \hat{V}_{KS}[n] \\ &= \hat{T}_s[n] + \hat{V}_{ext}[n] + \hat{V}_H[n] + \hat{V}_{xc}[n]\end{aligned}\quad (2.9)$$

where the four terms on the right are: the kinetic energy operator of non-interacting electrons, the external potential representing the interaction between an electron and the nuclei, the Hartree potential including coulomb repulsion between electrons, and the exchange-correlation potential. Thus, the single-particle Schrödinger equation or Kohn-Sham equation is derived as:

$$\left[ -\frac{1}{2}\nabla^2 + V_{ext}(r) + \int \frac{n(r')}{|r-r'|} dr' + \frac{\delta E_{xc}[n]}{\delta n(r)} \right] \phi_i(r) = \varepsilon_i \phi_i(r) \quad (2.10)$$

where the  $\varepsilon_i$  and  $\phi_i(r)$  denote the single-electron eigenvalues and wave functions. This approach generates a set of equations where each describes one electron. The electron density of the N-electron system is then obtained by summation over the occupied states:

$$n(r) = \sum_{i=1}^N |\phi_i(r)|^2 \quad (2.11)$$

For solving the set of Kohn-Sham equations, the challenge is to have an accurate form

of the exchange-correlation functional,  $E_{XC}[n]$  in Eq.(2.11). To this end, a number of approximations have been proposed.

### 2.3.3 Exchange-Correlation Functional

#### Local Density Approximation (LDA)

The local density approximation assumes that the electron correlation energy at a point  $r$  is equal to that of a homogeneous electron gas [17] which has the same electron density. Then, the corresponding (Eq.(2.10)) exchange-correlation energy functional can be written as:

$$E_{XC}^{LDA}[n] = \int n(r) \varepsilon_{XC}^{homo}(n(r)) dr \quad (2.12)$$

where the exchange-correlation energy density  $\varepsilon_{XC}^{homo}(n(r))$  is derived from the homogeneous electron gas with the electron density  $n(r)$  [18,19]. Moreover, the exchange-correlation energy density in a homogeneous electron gas (excluding the spin polarization) is an addition of the exchange and correlation terms:

$$\varepsilon_{XC}^{homo} = \varepsilon_X^{homo} + \varepsilon_C^{homo} \quad (2.13)$$

The exchange term can be given as:

$$\varepsilon_X^{homo} = -0.4582/r_s \quad (2.14)$$

and the correlation term is obtained by fitting the Quantum Monte Carlo simulation results proposed by Ceperley and Alder [17,18] as:

$$\varepsilon_C^{homo} = \begin{cases} -0.1423/(1 + 1.0529\sqrt{r_s} + 0.3334r_s), & r_s > 1 \\ 0.0311 \ln(r_s) - 0.048 + 0.002r_s \ln(r_s) - 0.0116r_s, & r_s \leq 1 \end{cases} \quad (2.15)$$

where  $r_s$  is the average distance between electrons in homogeneous electron gas:  $r_s = (3/4\pi n)^{1/3}$ . This approximation uses only the local electron density to evaluate the



exchange-correlation functional term and it is known as the local density approximation (LDA). The use of this method implies that the electron density is uniform in the vicinity of position  $r$ , so that the exchange-correlation energy is over-estimated in most materials.

## General Gradient Approximation (GGA)

In order to improve the LDA, the generalized gradient approximation (GGA) which includes both the electron density  $n(r)$  and its gradient  $\nabla n(r)$  in the exchange-correlation functional was proposed to account for the non-homogeneity of true electron density [20]. The corresponding functional is:

$$E_{XC}^{LDA}[n] = \int F[n(r), \nabla n(r)] \epsilon_{XC}^{homo}(n(r)) dr \quad (2.16)$$

$F_{XC}$  represents the influence of electron density gradient. For practical calculations of the properties of the materials, it has been necessary to develop various GGA functionals depending on the practical physical problem. For instance, for the calculation involving solids, two of the widely used functionals are the Perdew-Burke-Ernzerhof functional (PBE) [21] and Perdew-Wang functional (PW91) [22]. In this work, we choose the GGA-PEB since it can correct the overbonding problem and improve the cohesive energy with group III-nitrides and ZnO semiconductors [23]. However, it still has some drawbacks, such as, the underestimation of the band gap and a noticeable reduction of bulk modulus [23,24].

### 2.3.4 The Solution of the Kohn-Sham Equations

#### Variational Principle

Using the advanced approximations to describe the exchange-correlation energy functional, the Hamiltonian of Kohn-Sham system can be determined approximately. For performance, the electron wave function can be expanded by the basis set functions  $\varphi_\alpha(r)$  as:

$$\phi_i(r) = \sum_{\alpha}^{\infty} C_{i\alpha} \varphi_{\alpha}(r) = \sum_{\alpha}^M C_{i\alpha} \varphi_{\alpha}(r) \quad (2.17)$$

For the point of view of computer cost, the size of basis set functions is limited as a finite number of M.

For a certain Hamiltonian, the Kohn-Sham equations are then:

$$\hat{H}_{k-s} \sum_{\alpha}^M C_{i\alpha} \varphi_{\alpha}(r) = \varepsilon_{app} \sum_{\alpha}^M C_{i\alpha} \varphi_{\alpha}(r) \quad (2.18)$$

Multiplying by  $\varphi_{\beta}^*(r)$  on both sides of Eq.(2.18), and integrating in the whole space:

$$\sum_{\alpha}^M C_{i\alpha} \int \varphi_{\beta}^*(r) \hat{H}_{k-s} \varphi_{\alpha}(r) dr = \varepsilon_{app} \sum_{\alpha}^M C_{i\alpha} \int \varphi_{\beta}^*(r) \varphi_{\alpha}(r) dr \quad (2.19)$$

$$\sum_{\alpha}^M C_{i\alpha} [H_{\alpha\beta} - \varepsilon_{app} \delta_{\alpha\beta}] = 0 \quad (2.20)$$

where  $H_{\alpha\beta} = \int \varphi_{\beta}^*(r) \hat{H}_{k-s} \varphi_{\alpha}(r) dr$  and  $\delta_{\alpha\beta} = \int \varphi_{\beta}^*(r) \varphi_{\alpha}(r) dr$  are constants when  $\hat{H}_{k-s}$  and  $\varphi_{\alpha}(r)$  are known. This is an eigenvalue of the system which can be solved to give the approximate energies  $\varepsilon_{app}$ . The eigenvalues should converge to true energy values  $\varepsilon_i$  of the corresponding Hamiltonian when the basis set is increased to infinity.

## Self-Consistent Iteration

In practice the Kohn-Sham equations of Eq.(2.10) are solved in an iteratively as follows:

- (1) Define a initial electron density,  $n(r)$ , and deduce the starting Hamiltonian.
- (2) Solve the set of Kohn-Sham equations to obtain the single-particle electron wave function,  $\phi_i(r)$ .
- (3) Calculate the new electron density through Eq.(2.11) as  $n_{KS}(r)$ .
- (4) The criterion of convergence is: if  $n(r) = n_{KS}(r)$ , the ground state density is obtained. Thus, as long as  $n(r) \neq n_{KS}(r)$ , the calculated electron density is used as an input and the process is repeated from step (2).

In this way, the electron structure is obtained as well.

## 2.4 Hybridization Functional Method

A well-known limitation in DFT is the underestimated band gap prediction in semiconductors and insulators. On the contrary, Hartree-Fork (HF) theory generally leads to overestimation of the band gaps [25]. Hybrid functionals are combinations of non-local HF exchange energy and local density functional energy. One of the widely used hybrid functional is B3LYP (Becke, 3-parameters, Lee-Yang-Parr) exchange-correlation functional [26,27] which combines exchange energy of 80% DFT and 20% HF and correlation part of 19% Vosko-Wilk-Nusair (VWN) [28] and 81% Lee-Yang-Parr [29] energy, as well as an additional Becke's correction [30],  $\Delta E_X^{B88}$ . The expression can be written as:

$$E_{XC}^{B3LYP} = 0.8E_X^{LDA} + 0.2E_X^{HF} + 0.19E_X^{VWN} + 0.81E_C^{LYP} + 0.72\Delta E_X^{B88} \quad (2.21)$$

The involved coefficients are determined empirically by fitting on known molecules energies. Attempts have been made to reduce the number of empirical parameters, and for instance the PBE0 functional [31-33] mix the 25% HF exchange energy with 75% PBE exchange energy:

$$E_{XC}^{PBE0} = 0.25E_X^{HF} + 0.75E_X^{PBE} + E_C^{PBE} \quad (2.22)$$

In these approximations, the introduction of HF exchange contribution means a large computational effort since the decay of HF exchange energy is slow with distance. To reduce the computational cost, Heyd et al. [34] separated the exchange energy into two parts, short- and long-range. Only 25% of the short-range contribution comes from the HF exchange energy:

$$E_{XC}^{HSE03} = 0.25E_X^{srHF} + 0.75E_X^{srPBE} + E_X^{lrPBE} + E_C^{PBE} \quad (2.23)$$

The mixture of screened HF exchange in HSE03 [35] enlarges the band gaps for narrow and medium gap semiconductors.

In VASP, not only the three mentioned hybrid methods but also other latterly developed functionals (eg. HSE06 et al [36]) are available.

## 2.5 On-Site Coulomb Repulsion Correction-DFT+U

Use of the hybrid functional method can perform a better description of band structure, but the computational consumption is rather expensive. DFT+U is a semi-empirical approach to treat the strong on-site Coulomb interaction of localized electrons, such as: 3d- or 5f- orbitals and also p orbitals. The Hubbard-type on-site Coulomb repulsion parameter U and on-site exchange parameter J are added to the DFT Hamiltonian [37-39]. The DFT+U is introduced in ab initio through two ways. One of the methods proposed by Anasimov et al. [37] includes a single effective  $U_{eff}$  parameter considering only the Coulomb interaction and the DFT+U total energy is defined as:

$$E_{DFT+U} = E_{DFT} + \frac{U_{eff}}{2} \sum_{\sigma} Tr[\rho^{\sigma} - \rho^{\sigma} \rho^{\sigma}] \quad (2.24)$$

where the  $\rho^{\sigma}$  is the atomic orbital occupation matrix. If the on-site density matrix is idempotent,  $\rho^{\sigma} = \rho^{\sigma} \rho^{\sigma}$ , for example in a completely full or an empty band, the total energy is only dependent on DFT results. The other way is to split the single effect  $U_{eff}$

into two parameters as:  $U_{eff} = U - J$ . The DFT+U applicability of VASP has been widely used for transition-metal compounds [40-43] as well as for the group III-nitrides which contain full or partly filled d shells. In this thesis, the DFT+U method is the dominant approach adopted for achieving better description of electron structure within group III-nitrides and ZnO compounds.

## 2.6 Computational Methods

In practice, for performing a first-principle calculation, choices have to be made in advance: (i) The selection of a basis set to expand the eigenfunctions in Kohn-Sham equations, between plane waves and localized basis functions. (ii) The description of interactions between ionic core and valence electrons to use either a full-potential approach or pseudopotential method to avoid the consideration of complicate nodal character. (iii) The choice of exchange-correlation functional to describe the electron-electron interactions from the many DFT functionals (LDA, GGA or hybrid functional etc...) or DFT+U method.

According to the particular requirements, calculation packages are available for solving the Schrödinger equation. For instance, VASP (Vienna ab initio Simulation Package) [3-6] and SIESTA (Spanish Initiative for Electronic Simulations with Thousands of Atoms) are widely used to perform the ab-initio quantum-mechanical simulations. They have been applied for the calculation of the materials properties including the structure and phase stability, magnetism, mechanical and dynamical properties, chemical reaction etc.. VASP and SIESTA are utilized in this work to model the (0001) plane IDBs and [0001] tilt GBs, respectively.

### 2.6.1 Simulation Packages

VASP is a plane wave code using ultra-soft pseudopotentials or projector-augmented wave (PAW) method to describe the electron-core interactions. In contrast SIESTA implements strictly localized basis set and linear-scaling algorithms to allow dealing

with the system with larger number of atom systems. Both packages can use the local density (LDA) and generalized gradient (GGA) approximations for implementation of electron-electron interactions. In the following, a summary of the procedures used in VASP and SIESTA are introduced.

## Basis set

As pointed out in section 2.3.4, for solving the Kohn-Sham equations and reduce the computation cost, definite number of basis set functions are used to expand the electron wave function. In VASP, plane wave functions are used as the basis set. In practical, a reasonable convergence of plane wave basis set can be achieved when performing the total energy versus cut-off energy curve. Besides, the use of the plane wave basis set is independent of the topology of system. It can perform better prediction on system energy and avoid the basis-set superposition errors [44].

SIESTA package uses linear combination of atomic orbital (LCAO) basis set in which the basis functions are atom-centered. It strictly goes to zero beyond a specific radius from the center. The orbitals are the products of radial function and spherical harmonic. In the case of single-zeta (minimal) basis set, one atomic orbital consists of only one radial dependent function. This small basis set is suitable for a fast structural search and less cost simulation. Beyond this, multiple-zeta is realized using one or several radial dependent orbitals with the same angular dependence. The cut-off radii of these orbitals is in general different. So that the scale of basis set is increased to perform a careful simulation.

## Pseudopotentials

When solving the Kohn-Sham equations, the single electron wave functions are expanded as the product of basis set like plane wave functions or local-basis set as mentioned in last section. However, difficulties still exist: 1) inside the atomic core region, electron wave functions oscillate rapidly, as seen in the region  $r < r_c$  in Figure

2.1, so that a large basis set is needed to reach a precise presentation. In addition, the wave functions are localized and their response to the chemical environment is stiff. 2) In bonding region ( $r > r_c$ ), the electron wave function is smooth and response rapidly to the chemical environment. Different strategies are developed to reach the requirements.

The concept of pseudopotential was first advanced by Hans Hellmann in 1934 [45]. It treats the core electrons and the nucleus as rigid non-polarizable ion core with an effective potential. Only chemical active valence electrons are explicitly described by plane wave basis functions or local-basis set functions to reduce the computational effort. Outside the core region  $r > r_c$ ), see solid line of Figure 2.1, the pseudo wave function and potential of nucleus produce the same eigenenergy and amplitude as the all-electron approach. While the wave function inside the ion core region is nodeless and smooth. Use of the method efficiently reduced the number of basis set functions when solving the Kohn-Sham equations and the number of electrons counted as well. However, the loss is the unknown electronic state inside the core region.

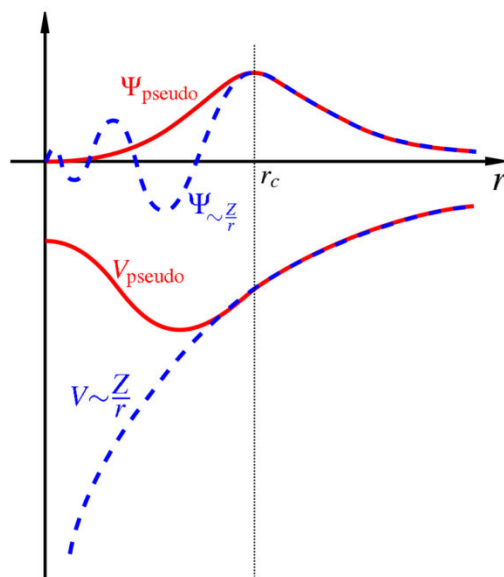


**Figure 2.1.** Comparison of the real (blue) and the pseudo (red) potentials and their corresponding electron wavefunctions. Beyond a certain cutoff radius  $r_c$ , the two are in agreement (see <https://en.wikipedia.org/wiki/Pseudopotential>).

The other way to simplify the electron-core interaction is to develop the basis set functions. Via the combination of pseudopotential method and full-potential linearized augmented plane wave (FLAPW) method [46], projector-augmented wave (PAW) method is first advanced by Blochl [47], which becomes the benchmark of DFT calculation in VASP method. In PAW method, the all-electron (AE) wave function is reconstructed using Pseudo (PS) wave function with a linear transformation:

$$|\Psi_n^{AE}\rangle = |\Psi_n^{PS}\rangle + \sum_i (|\varphi_i^{AE}\rangle - |\varphi_i^{PS}\rangle) \langle p_i^{PS} | \Psi_n^{PS} \rangle \quad (2.25)$$

where, within the augmentation region, the AE and the corresponding PS wave functions can be linearly expanded by their partial wave functions:  $|\Psi_n^{AE}\rangle = \sum_i |\varphi_i^{AE}\rangle c_i$ ,  $|\Psi_n^{PS}\rangle = \sum_i |\varphi_i^{PS}\rangle c_i$ , and the common coefficients are products of PS wave function and projector functions:  $c_i = \langle p_i^{PS} | \Psi_n^{PS} \rangle$ . The transformation results can be determined by quantifying the three terms:

- 1) AE partial wave function  $|\varphi_i^{AE}\rangle$  by integrating the Schrodinger equation of the atomic energy for a set of energies  $\varepsilon_i$  and orthogonalization to the core states;
- 2) Outside the augmentation region, a PS partial wave function  $|\varphi_i^{PS}\rangle$  is identical with the AE partial wave function;
- 3) Within the augmentation region, the projector function obeys the relationship:  $\langle p_i^{PS} | \varphi_j^{PS} \rangle = \delta_{ij}$ .

In VASP code, the valence electron-core interaction is described using pseudopotentials or PAW method. The size of basis set is restricted to be small to save the computational resource. Even with the transition metals, the number of the plane wave required to describe the bulk material is restricted within 100 per atom. In some case, only 50 PW per atom is sufficient to achieve an adequate description.

In SIESTA code, norm-conserving pseudopotential is used [48] in the form of:



$$V_{ps}(r) = \sum_l \sum_m |Y_{lm}\rangle V_{lm}(r) \langle Y_{lm}| \quad (2.26)$$

where  $|Y_{lm}\rangle$  is a one-particle wave function projected to the angular momentum ( $l$  and  $m$ ).  $V_{lm}(r)$  is the pseudopotential acting onto the projected component. The norm-conserving pseudopotentials are non-local potentials. The generation of norm-conserving pseudopotentials relies on two conditions:

1.  $\int_0^{r_c} \varphi_{AE}^*(r) \varphi_{AE}(r) dr = \int_0^{r_c} \varphi_{ps}^*(r) \varphi_{ps}(r) dr$  , where  $\varphi_{AE}(r)$  is the all-electron wavefunction and  $\varphi_{ps}(r)$  is the pseudo-wavefunction. This means that, inside the cut-off radius  $r_c$  , the norm of each pseudo-wave function is equal to that of the corresponding all-electron wave function.
2. Outside of the chosen cut-off radius  $r_c$  , all-electron wave function is identical to the pseudo- wave function.  $\varphi_{AE}(r) = \varphi_{ps}(r)$ , when  $r > r_c$ .

### 2.6.2 Relative Formation Energies

When dealing with defects in a perfect material, the question is to determine the additional energy that is consumed by the system for the generation of such a defect. This formation energy of a defect  $X$  is calculated by following the definition of Van de Walle [49] as:

$$E[X] = E_{tot}[X] - E_{tot}[reference] - \sum_i n_i \mu_i \quad (2.27)$$

$E_{tot}[X]$  and  $E_{tot}[reference]$  are the total energies of the supercell containing the defect and of the reference structure.  $n_i$  indicates the number of atoms of  $i$  element that have been added to ( $n_i > 0$ ) or removed from ( $n_i < 0$ ) the supercell when the defect or impurity is created,  $\mu_i$  is the corresponding chemical potential of element  $i$ . By defining the upper and lower bounds associating with the experimental process, the relative stability of the defect with respect to the reference structure can be determined. For example, in ZnO, the formation energy of a Zn point defect can be given as:  $E[X] =$

$\Delta E + \mu_{Zn}$ . The chemical potential of Zn,  $\mu_{Zn}$ , is subjected to an upper bound  $\mu_{Zn} \leq \mu_{Zn}[Zn, bulk]$  in Zn-rich growth condition to avoid the precipitation of bulk Zn. However, in thermodynamic equilibrium of bulk ZnO, it follows the expression:  $\mu_{Zn} + \mu_O = E_{tot}[ZnO]$ . So, the lower limitation of  $\mu_{Zn}$  can be obtained when  $\mu_O$  takes the maximum. In O-rich condition, the maximum of  $\mu_O$  is  $\mu_O[O_2, gas]$ . The firm bounds of  $\mu_{Zn}$  is shown as:  $E_{tot}[ZnO] - \mu_O[O_2, gas] \leq \mu_{Zn} \leq \mu_{Zn}[Zn, bulk]$ . So that the defect is relatively stable under the various range of chemical potential.

### 2.6.3 Chemical Bonding Properties

The electron localization function (ELF) was introduced by Becke and Edgecombe based on Hartree-Fock theory [50]. They proposed that the electron localization can be given by:

$$D(r) = \tau(r) - \frac{1}{4} \frac{(\nabla n(r))^2}{n(r)} \quad (2.28)$$

where  $\tau(r)$  is the kinetic energy density and  $n(r)$  is the electron density. The localization value  $D(r)$  is expected to be small in areas where the localized electrons are located. The relative electron localization with respect to the uniform electron gas  $D_0(r)$  which possesses the same electron density  $n(r)$  is:

$$\kappa(r) = \frac{D(r)}{D_0(r)} \quad (2.29)$$

where  $D_0(r) = \frac{3}{5} (6\pi^2)^{2/3} n^{5/3}(r)$ . ELF is defined as the electron localization function by mapping its values from 0 to 1 in the three-dimensional (3D) space and projecting along particular projections of the investigated material:

$$ELF(r) = \frac{1}{1 + (\kappa(r))^2} \quad (2.30)$$

ELF=1 indicates the perfect electron localization and ELF=1/2 corresponds to the uniform electron gas [51-53]. The ELF in bulk GaN is shown in Figure 2.2 to give a

first insight on the binding character. The 3D topological representations, where only one ELF value, as called isosurface value  $\eta$ , is shown in Figure 2.2(a) and (b) with the value of 0.7 and 0.83, respectively. As seen, owing to the large electronegativity of nitrogen, the electron localization domains of Ga-N bonds are more localized towards N core (yellow regions in Figure 2.2(a) and (b)). As increasing the isosurface value  $\eta$  from 0.7 to 0.83, the electron localization domains further bifurcate spatially into four irreducible domains, named as bonding attractors, which are consistent with the four polarized covalent Ga-N bonds in bulk material [51]. Additionally, 2D slice contour of ELF is adopted, where the ELF values are coded in a color scheme range from blue through green, and yellow to brown when the ELF value increases from 0 to 1, to visualize the electron localization property. As per Figure 2.2(c), the high electronic localization regions, large value of ELF, are seen as a large yellow-brown annular region and they correspond to N atoms. On the contrary, the Ga atoms are seen as the light blue ring. Atomic ball-stick model is correspondingly superimposed onto the 2D slice contour to identify the atoms.

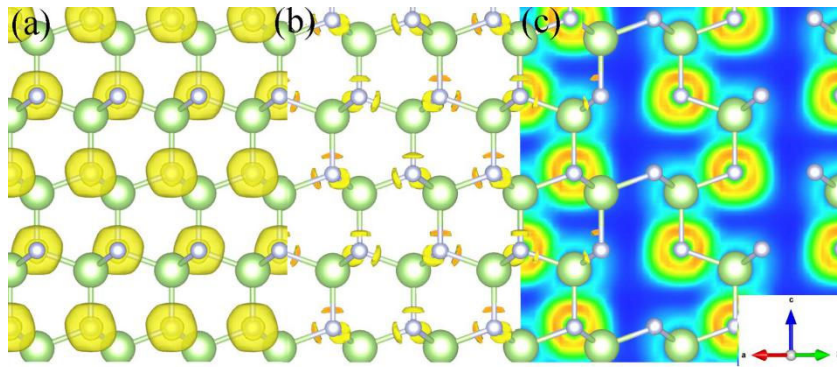


**Figure 2.2.** ELF of bulk GaN. (a) and (b) 3D topological representations bounded with the isosurface value  $\eta = 0.7$  and  $\eta = 0.83$  unveil the spatial electron localization; (c) 2D slice contour indicates the chemical bonding character between two atoms. Large and small atoms correspond to Ga and N, respectively.

The covalent character of Ga-N bond is seen in the localization domains of N atoms pointing towards domain of Ga atoms, without a clear cut separation. Analysis of the ELF mapping over the whole space provides a way to understand the chemical bonding

character between atoms and the distribution of electron localization in the overall configuration.

## 2.6.4 Electronic Structure

The electronic structure of group III-nitrides and ZnO has been a subject of extensive investigations in the literature [54,55]. A number of theoretical techniques such as semi-empirical and ab initio methods [56], as well as experimental measurements like x-ray spectroscopy [57] have been used for such investigations. In addition to the usual two dimensional band structure in the section of the reciprocal space, the main features of the spectroscopy are present through two ways. 1) The total density of states (DOS) which shows the total occupation of the states and 2) the partial density of states (PDOS) which exhibits each contribution of the valence electron orbitals for the constituents. For instance, in the case of nitrides and ZnO, it can be seen in Figure. 2.3 that for both AlN and ZnO compounds, the total DOS patterns present three regions, whereas for GaN and InN, four segments are seen in the right panels of Figure 2.3. Moreover, the examination of the PDOS shows that the metal-d electrons play an important role on the valence band. As seen in Figure 2.3(a), in absence of d electrons, the lowest part of valence band ranging from -15 to -12.5 eV is contributed from N:2s and Al:3s electron orbitals. The immediate upper valence band with the energy range between -6 and 0 eV is dominated by Al:3p, 3s and N:2p electron orbitals. As for the first conduction band, Al:3s electron orbital is dominant. As for ZnO shown in Figure 2.3(c), since the Zn:3d electron orbital is located at the middle of valence band, a strong hybridization of Zn:3d, 3s and O:2p orbitals is present at energy range between -6 and -4.5 eV. The valence band edge states are contributed by Zn:3d, 3p and O:2p orbitals. The lowest valence band states mainly come from O:2s orbital and a small contribution of Zn:3s. The first conduction band is predominantly contributed by Zn:3s electron orbital [54].

Unlike the DOS patterns of AlN and ZnO in which the cation d electrons are absent or their location is at middle of valence band, the electronic structures of GaN and InN

possess four regions and similar characters as reported in the literature [57]. as shown in Figure 2.3(b) and (d). The metal-d electron orbitals are located at bottom of valence band. Therefore, from -16 to -12 eV, the hybridization states mainly come from metal-3d and N:2s electrons. The Ga/In:s electrons hybridize with N:2p states at the energy range from -7 to -4 eV in GaN and from -5.5 to -3 eV in InN. As for the valence band edge, strong hybridization of Ga/In:p and N:2p states is dominant. In agreement with the AlN and ZnO, the lowest conduction bands of GaN and InN are originated from Ga/In:s electrons.

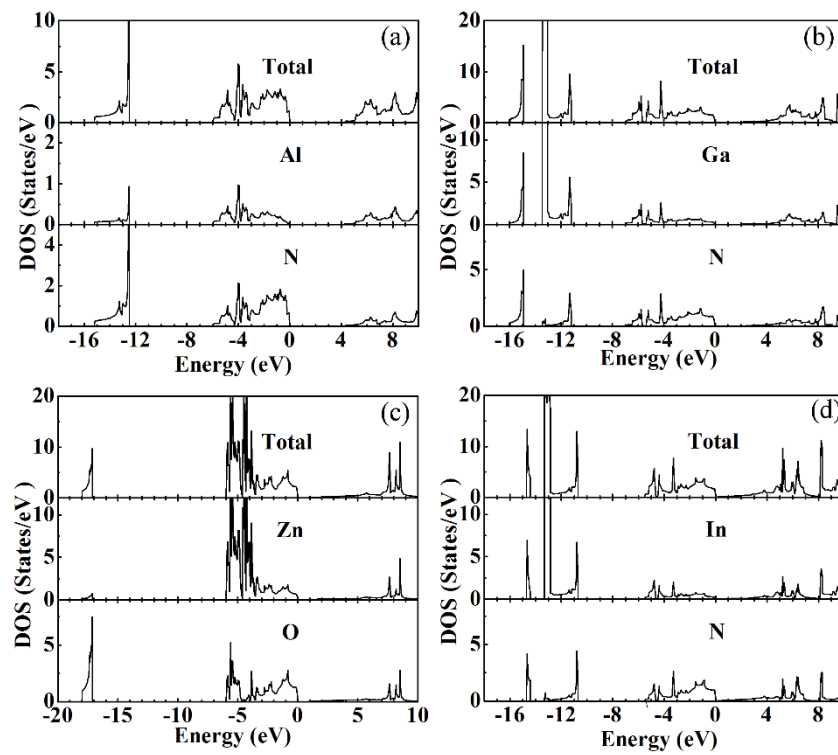


**Figure 2.3.** Calculated DOS and PDOS of the group-III nitrides and ZnO. The Fermi level is allocated to zero position.

## References

- [1] M.C. Payne; Rev. Mod. Phys. 64, 1054 (1992).
- [2] X. Gonze, G.M. Rignanese, M. Verstraete, J.M. Beuken, Y. Pouillon, R. Caracas,

- F. Jollet, M. Torrent, G. Zerah, M. Mikami, P. Ghosez, M. Veithen, J.Y. Raty, V. Olevano, F. Bruneval, L. Reining, R. Godby, G. Onida, D.R. Hamann, D.C. Allan, *Comput. Mater. Sci.* 25, 478 (2002).
- [3] G. Kresse, J. Hafner, *Phys Rev B* 47, 558 (1993).
- [4] G. Kresse, J. Furthmüller, *Computat Mater Sci* 6, 15 (1996).
- [5] G. Kresse, J. Furthmüller, *Phys Rev B* 54, 11 169 (1996).
- [6] G. Kresse, D. Joubert, *Phys Rev B* 59, 1758 (1999).
- [7] J.M. Soler, E. Artacho, J.D. Gale, A. Garcia, J. Junquera, P. Ordejon, D. Sanchez-Portal, *J Phys Condens Matter* 14, 2745 (2002).
- [8] P. Giannozzi, S. Baroni, N. Bonini et al. *Journal of Physics: Condensed Matter*. 21 (39), 395502 (2009).
- [9] P. Giannozzi, O. Andreussi, T. Brumme, O. Bunau et al. *Journal of Physics: Condensed Matter*. 29(46), 465901 (2017).
- [10] M. Born, J.R. Oppenheimer (1927). "Zur Quantentheorie der Molekeln" [On the Quantum Theory of Molecules]. *Annalen der Physik* (in German). 389 (20), 457 (1927).
- [11] P. Coppens, *X-ray charge densities and chemical bonding*; International Union of Crystallography, Oxford University Press, 1997.
- [12] R.F. Bader, *Atoms in Molecules: A Quantum Theory* (International Series of Monographs on Chemistry); Clarendon Press, 1994.
- [13] D. Stalke, *Electron Density and Chemical Bonding I* ; Springer, 2012.
- [14] D. Stalke, *Electron Density and Chemical Bonding II* ; Springer, 2012.
- [15] P. Hohenberg, W. Kohn *Physical Review*. 136, B864 (1964).
- [16] W. Kohn and L.J. Sham, *Phys. Rev.*, 140, 1133A (1965).
- [17] J.P. Perdew and A. Zunger, *Phys. Rev. B* 23, 5048 (1981).
- [18] D.M. Ceperley and B.J. Alder, *Phys. Rev. Lett.* 45, 566 (1980).
- [19] U. Von Barth and L. Hedin, *J. Phys. C* 5, 1629 (1972).
- [20] F. Herman, J.P.V. Dyke and I.P. Ortenburger, *Phys. Rev. Lett.* 22, 807 (1969).
- [21] J.P. Perdew, K. Burke, M. Ernzerhof, *Phys. Rev. Lett.* 77, 3865 (1996).
- [22] J.P. Perdew, Y. Wang, *Phys. Rev. B* 45, 13244 (1992).

- [23] M.Fuchs, J.L.F.D.Silva, C. Stampfl, J. Neugebauer, and M. Scheffler, Phys. Rev. B 65, 245212 (2002)
- [24] C. Stampfl and C.G. Van de Walle, Phys. Rev. B 59, 5521 (1999).
- [25] A.J. Garza and G.E. Scuseria, J. Phys. Chem. Lett. 7(20), 4165 (2016).
- [26] P.J. Stevens, F.J. Devlin, C.F. Chablowski, M.J. Frisch, J Phys Chem. 80, 11 623 (1994).
- [27] A.D. Becke, J Chem Phys. 98, 5648 (1993).
- [28] S.H. Vosko, L. Wilk, M. Nusair, Can J Phys. 58, 1200 (1980).
- [29] C. Lee, W. Yang, R. Parr, Phys Rev B 37, 785 (1988).
- [30] A.D. Becke, Phys. Rev. A 38, 3098 (1988).
- [31] J.P. Perdew, K. Burke, M. Ernzerhof, Phys Rev Lett 78, 1396 (1997).
- [32] J.P. Perdew; M. Ernzerhof; K. Burke, J. Chem. Phys. 105, 9982 (1996).
- [33] A. Carlo, V. Barone, The Journal of Chemical Physics. 110, 6158 (1999).
- [34] J. Heyd, G.E. Scuseria, J Chem Phys 118, 8207 (2003).
- [35] J. Heyd and G.E. Scuseria, J. Chem. Phys. 121, 1187 (2004).
- [36] A.V. Krukau, O.A. Vydrov, A.F. Izmaylov, and G.E. Scuseria, J. Chem. Phys. 125, 224106 (2006).
- [37] S.L. Dudarev, G.A. Botton, S.Y. Savrasov, C.J. Humphreys, A.P. Sutton, Phys Rev B 75, 1505 (1998).
- [38] A.I. Lichtenstein, V.I. Anisimov, J. Zaanen, Phys Rev B 52, 5467 (1995).
- [39] O. Bengone, M. Alouani, P. Blöchl, J. Hugel, Phys Rev B 62, 16392 (2000).
- [40] A. Rohrbach, G. Kresse, J. Hafner, J Phys Condens Matter 15, 279 (2003).
- [41] A. Rohrbach, G. Kresse, J. Hafner, Phys Rev B 69, 075413 (2004).
- [42] A. Rohrbach, G. Kresse, J. Hafner, Phys Rev B 70, 125426 (2004).
- [43] G. Rollmann, A. Rohrbach, P. Entel, J. Hafner, Phys Rev B 69, 165107 (2004).
- [44] J. Hafner, Journal of Computational Chemistry 29 (13): 2044-2078 (2008 )
- [45] H. Hellmann, J. Chem. Phys. 3, 61 (1935).
- [46] D. J. Singh, Plane Waves, Pseudopotentials and the LAPW Method; Kluwer Academic, Norwell, MA, 1994.
- [47] P. E. Blöchl, Phys Rev B 1994, 50, 17 953.

- [48] D.R. Hamann, M. Schlüter, and C. Chiang, Phys. Rev. Lett. 43, 1494 (1979).
- [49] C. G. Van de Walle, and J. Neugebauer, JAP, 95, 3851 (2004);
- [50] A. D. Becke and K. E. Edgecombe, J. Chem. Phys. 92 (9): 5397
- [51] A. D. Becke, K. E. Edgecombe, A. D. Edgecombe, J. Chem. Phys. 1990, 92, 5397-5403.
- [52] A. Savin, O. Jepsen, J. Flad, O. K. Andersen, H. Preuss, H. G. Von Schnering, Electron Localization in Solid-state Structures of the Elements: the Diamond Structure. Angewandte Chemie-International Edition in English 1992, 31, 187-188.
- [53] B. Silvi, and A. Savin, Nature 371, 683-686 (1994).
- [54] P. G. Moses, M. S. Miao, Q. Yan and C. G. Van de Walle, J. Chem. Phys, 134, 084703 (2011).
- [55] F. S. Saoud, J. C. Plenet and M. Henini, J. Alloys Compd. 619, 812-819 (2015).
- [56] D. J. Chadi and M. L. Cohen, Phys. Stat. Sol. (b), 68 (1975) 405
- [57] M. Magnuson, M. Mattesini, C. Höglund, J. Birch, and L. Hultman, Phys. Rev. B 81, 085125 (2010).



## Chapter 3

### **(0001) Plane Inversion Domain Boundaries (IDBs) in Wurtzite Semiconductors**

#### 3.1 Introduction

During the last decades, the nitride semiconductors have come up to dominate the optoelectronic industry especially for applications in lighting [1]. They crystallize in the wurtzite structure, which exhibits polarity along its [0001] direction which is used for the fabrication of most devices. For instance, heavy p doping of GaN leads to a change in polarity during the growth in a non-controlled way [2] with Mg rich precipitates at the interface between the Ga and N-polar zones. More recently, it appeared that high electron mobility transistors may have best characteristics along the N polar side of the device on single crystal GaN substrates [3]. Therefore, the polarity governs the physical properties in these materials and has an impact on the devices. In nitride layers grown along the [0001], extensive attention has been focused on the polarity reversal and plenty of investigation methods like TEM and theoretical calculation have been carried out on  $\{10\bar{1}0\}$  IDBs to investigate their native structure and growth behavior [4-7]. However, up to now, only Kim and Goo [8] reported a TEM observation of (0001) plane IDB in polycrystalline ZnO material with a flat interface and they proposed eight possible geometric models. They concluded that a head-to-head type IDB with the stacking sequence of AaBbAa-AcCaA could be the most stable structure in their sample by matching the high-resolution TEM images with the simulation images of geometrical models. However, the local structure and electronic properties were not dealt with in their investigation.

The most stable form of group III-nitrides and ZnO compounds is the wurtzite structure which exhibits a polarity along [0001] direction. The polarity reversal may occur during the film growth, which may influence the material property. Therefore, it is necessary

to investigate this resulting planar interface for homogeneous materials in order to contribute to a better understanding of the materials and necessary polarity control during the growth of epitaxial layers.

In this chapter, based on the eight models proposed by Kim and Goo [8], as seen in Figure 1.8, the energetic stability of these (0001) plan IDB models is investigated for group III-nitrides (AlN, GaN and InN) and ZnO homogeneous compounds since they share the same wurtzite structure. Subsequently, their chemical bonding character, Bader charge as well as electronic structure are investigated in detail.

### 3.2 Simulation Method

First-principle calculations with the slab geometry scheme are implemented using Vienna ab initio simulation package (VASP) to calculate the total energies, charge transfer as well as the electronic structures. The slabs with stacking sequence of (AaBb)<sub>9</sub>A- (Metal-polar) and (AbBa)<sub>9</sub>A- (N-polar) are first constructed as substrates along the [0001] direction. The corresponding polarity inverted slabs starting with nitrogen atoms are put on the front metal surfaces with displacement of  $1/3[10\bar{1}0]$  (displacement vectors are shown in Table 1.4) to form H and T IDBs. Figure 3.1 and 3.2 give the detailed interface configurations. The surfaces are saturated with virtual hydrogen (H\*) which host corresponding fractional electron located straight along [0001] direction for termination. A vacuum layer of  $\sim 24.434 \text{ \AA}$  thickness is set to avoid the artificial interactions. In the supercells the in-plane coordinates (x and y directions) of atoms away from boundaries are fixed. The relaxation along c-axis did not give rise to any significant change in the test calculations [9]. The exchange correlation functional adapts the generalized gradient approximation [10, 11] with the U corrections (GGA+U) according to the approach of reference 12 and the pseudopotential uses the projector augmented-wave method (PAW) method [13]. The  $21 \times 21 \times 1$  Monkhorst-Pack Gamma k-point mesh is applied for Brillouin zone sampling. The atomic positions are optimized until the force on each atom is less than  $10^{-2} \text{ eV/\AA}$ , and the energy difference between two electronic steps reaches  $10^{-6} \text{ eV}$ . The valence

electron configurations are chosen as: Al( $3s^23p^1$ ), Ga( $3d^{10}4s^24p^1$ ), In( $4d^{10}5s^25p^1$ ) Zn( $3d^{10}4p^2$ ) and N( $2s^22p^3$ ), respectively.

### 3.3 Energetic Stability

The calculated relative energies obtained by total energy calculation of DFT are utilized to make statement for the relative stability among those candidates as shown in Table 3.1. The number of atoms and polarity arrangements are different between H and T IDBs but are identical in H and T supercells respectively, therefore the relative energies are evaluated by taking total energy of H1 and T1 supercell as their respective reference. For H IDBs, H4 is the most stable configuration in GaN, InN and ZnO materials with the energies slightly lower than those of H1 (~1, 4 and 10 meV lower in GaN, InN and ZnO respectively). This is understandable when comparing the atomic stacking sequences of H1 (A/B/A/C/B) and H4 (A/B/A/C/A) (seen in Figure 1.8). It can be seen that the first-nearest neighbors of interfacial cations are similar. The changes of stacking sequence take place at the second-nearest neighbors suggesting a small influence on energetics as reported by Yanfa Yan and M.M. Al-Jassim [14] for IDBs in ZnO. Moreover, as compared with H1 IDB which hosts two violations of stacking rule, H4 possesses only one stacking violation which is expected to be more energetically favorable [15, 16]. H2 and H3 IDBs have linear metal-nonmetal-metal bonding at boundaries and their calculated total energies are 46, 650 and 520 meV higher than those of H4 in GaN, InN and ZnO, respectively. As for AlN, H1/H4 have higher energies than H2/H3, which is at variance to the results obtained in the another three compounds. Bond length distribution analysis reveals that, in interface region, H1/H4 IDBs shows a deformation of ~9.3% in AlN, which is around 1.3% larger than those in GaN and InN. However, the bond length deformations of H2/H3 IDBs in AlN are rather small, 1.1% on average, when compared with the other two compounds. This is probably at the origin of the lower energy in H2/H3 with respect to H1/H4 in AlN.

As for T types, the T2 IDB exhibits the lowest relative energy in all group III-nitrides

discussed here which indicates that it is more energetically favorable. The interactions between the first-nearest neighbor metal layers play a primary role on the thermodynamic stability. As seen in Figure 3.2, the interfacial cation-anion bonds in T IDBs are distorted after structural relaxation. Moreover, the calculated lattice distortions (strains) between the first-nearest metal atom layers of interfacial N layer in T2 are smaller than those of T1 (~0.5% smaller), and T3/T4 (~5% smaller).

**Table 3.1** IDB relative energies calculated in AlN, GaN and InN with DFT by taking H1 and T1 as the respective reference in H and T IDBs. The relative energies are given in meV.

	AlN	GaN	InN	ZnO		AlN	GaN	InN	ZnO
H1	0	0	0	0	T1	0	0	0	0
H2	-46	46	652	520	T2	-59	-35	-12	0
H3	-46	47	654	520	T3	249	110	222	200
H4	-2	-1	-4	-10	T4	200	84	210	200

### 3.4 Chemical Bonding and Bader Population Analysis

To visualize the chemical bonding character and charge transfer in the vicinity of the boundaries, the ELF as well as Bader charge population are calculated for the H and T IDBs in the group III-nitrides and ZnO homogeneous compounds. Since group III-nitrides and ZnO compounds have the same tetrahedral bonding characters, in the following, the main properties of chemical bonding around IDB regions and the layer-by-layer charge transfer profile near the boundaries are shown through the example of GaN.

Following the basic conception of ELF introduced in chapter 2 (section 2.7.3), ELF is calculated for all the IDBs with homogeneous wurtzite compounds. Figure 3.1 and 3.2 display the obtained ELF isosurface contours of H and T IDBs along with the structures

projected along  $[11\bar{2}0]$  direction. The corresponding color-coded 2D contour slices are depicted on right-hand panel. As expected, owing to the large electronegativity of nitrogen, the electron localization domains of Ga-N bonds are more localized towards N core and further bifurcate spatially into four irreducible bonding attractors (yellow regions in left-hand panels of Figure 3.1 and 3.2) by increasing the isosurface  $\eta$  value to 0.823, which is consistent with the four polarized covalent Ga-N bonds in bulk material [17]. The electron localization domains between the interfacial Ga atoms and the first-nearest neighbor N atoms in H1 and H4 IDBs show the identical bifurcation of four spherical bonding attractors corresponding to perfect crystal region (seen in left panels of Figure 3.1(a) and (d)). However, for H2 and H3 IDBs, as the interfacial N atoms bind with only two Ga atoms due to the linear Ga-N-Ga bond chain, the spherical electron localization domains divide into two bonding attractors with 180 degree apart along the Ga-N-Ga bond direction (shown in left panels of Figure 3.1(b) and (c)).

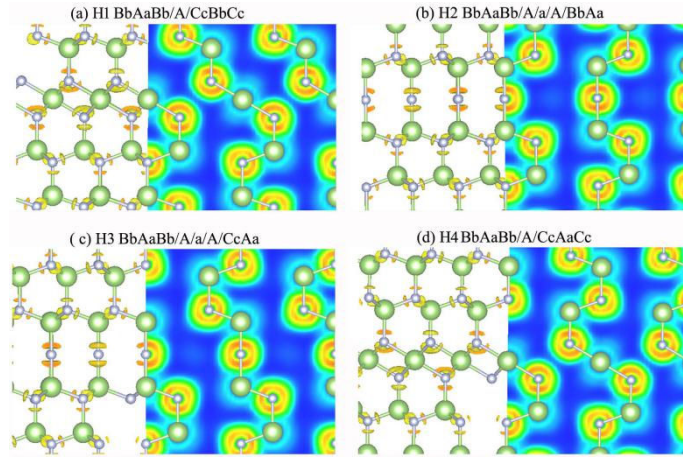


**Figure 3.1.** ELF isosurface contours with  $\eta=0.823$  on the left-hand panel and the corresponding 2D contour slice crossing atomic plane on right-hand panel for H IDBs in GaN. The green and grey ball represent Ga and N atom, respectively. The respective atomic stacking sequences are shown on top: (a) H1, (b) H2, (c) H3 and (d) H4.

The 2D contour slices of H IDBs are shown in right panels of Figure 3.1. There is no obvious change exhibited by the ELF graphical presentation in H IDBs, the picture is more or less similar to that of a perfect crystal. For the T IDBs, the situation is completely different; as shown in Figure 3.2, the Ga-N bonds below the interfacial N atoms are stretched after structural relaxation and the electron localization domains

around the interfacial N atoms bifurcate into smaller domains along the bond directions radically deviating from the tetrahedral geometry in all T IDBs. In particular, all the 2D contour slices exhibit a visible electron delocalization with ELF value of about 0.5 at Ga atomic layer just below the interface which indicate a homogeneous electron gas at the boundaries [18].

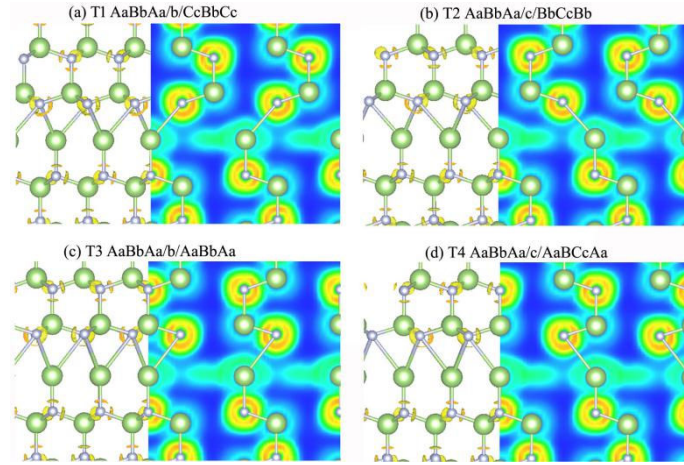


**Figure 3.2.** The ELF isosurface contours of T IDBs in GaN. The  $\eta$  values and atom balls stay the same as in Figure 3.1: (a) T1, (b) T2, (c) T3 and (d) T4.

Bader charge analysis of each atomic layer is carried out to quantify the charge transfer at IDBs [19]. Independent of atomic species, H1/H4, H2/H3 and T IDB possess similar electron transfer behavior, respectively; Figure 3.3(a) shows Bader charges of Ga and N atomic layer along [0001] direction in H IDBs. As can be seen, the first-nearest neighbor N atomic layers just below and above interfacial Ga layer in H1/H4 structures has a Bader charge of  $-1.2e^-$  per atom,  $0.32e^-$  lesser than the value in perfect crystal ( $-1.52e^-$  per atom). This indicates a positively charged N atomic layer in H1/H4 boundary regions. Similar with the H1/H4 structures, an extra positive charge excess of  $0.61e^-$  per atom is also found to confine at the interfacial N atomic layer in H2/H3 ones. This hole accumulation appearing at one monolayer of IDBs can be considered as 2-dimensional hole gas (2DHG). In contract to H IDBs, a distinct electron accumulation with an extra negative charge of  $0.9e^-$  per atom is located at the Ga atomic layer just below the interfacial N layer in all T IDB regions as shown in Figure 3.3(b). In this case, the adjacent interfacial N layer is slightly positively charged by about  $0.11e^-$  per

atom. This electron accumulation at interfacial monolayer of T IDBs suggests the formation of a 2-dimensional electron gas (2DEG), which is in agreement with the of ELF contours in Figure 3.2. However, the ELF cannot show the hole density; therefore, the 2D slices of H IDBs in Figure 3.1 do not exhibit any visible change across the boundaries. Considering AlN, InN and ZnO, the hole accumulation (2DHG) or the electron excess (2DEG) appear at the same atomic layers similar to GaN although with different charge values. The final net charges after removal of the bulk values are given in Table 3.2, where the values for GaN have also been included. It can be pointed out that, similar with GaN, the N atom at the first-nearest neighbor layer below and above the IDBs has a positive net Bader charge of  $0.57e^-$ ,  $0.2e^-$  and  $0.18e^-$  in AlN, InN and ZnO in H1/H4 IDBs respectively. And also, the interfacial N atom in H2/H3 IDBs has an additional positive charge of  $1.15e^-$ ,  $0.52e^-$  and  $0.4e^-$  in AlN, InN and ZnO respectively. This indicates the formation of 2DHG in H IDBs. As for T IDBs, the negatively charged cation layers with the magnitude of  $1.35e^-$ ,  $0.7e^-$  and  $0e^-$  per atom contribute 2DEG just below the interface in T IDBs.

The charge transfer in IDBs is induced by the polarization (P) discontinuity of the two domains above and below [9,20,21]. In the H IDBs, the substrate has cation-polarity with a spontaneous polarization ( $P_{sp}$ ) pointing to [0001] direction. While the upper domain has a N-polarity with an equal value of  $P_{sp}$  but opposite direction. This polarization discontinuity leads to a maximum negative sheet charge density  $\delta$  (about -0.162, -0.058, -0.064 and -0.114 C/m<sup>2</sup> for AlN, GaN, InN and ZnO, orderly [22]) in boundaries. It consequently induces a positive charge (hole) accumulation at H boundaries [20] which is confirmed by Bader charge analysis shown in Figure 3.3(a) and Table 3.2. In contrast to H IDBs, T types have a N-polarity in substrate and cation-polarity in upper region. Therefore, the discontinuity in spontaneous polarization results in a maximum positive sheet charge density  $\delta$  (about +0.162, +0.058, +0.064 and +0.114 C/m<sup>2</sup> for AlN, GaN, InN and ZnO respectively) in boundaries, which leads to an electron excess at T boundaries. As seen in Figure 3.3(b), all the T types exhibit electron accumulation in boundaries. Besides, in addition to the spontaneous

polarization, a piezoelectric polarization with an opposite direction with respect to its corresponding Psp is induced in substrates of T types due to tensile strain after structural relaxation (up to 2.5% bond deformation as shown above). As a consequence, the electron accumulation regions shifted down to cation-layer of substrate which is consistent with the ELF and Bader charge analysis in Figure 3.2 and Figure 3.3(b).

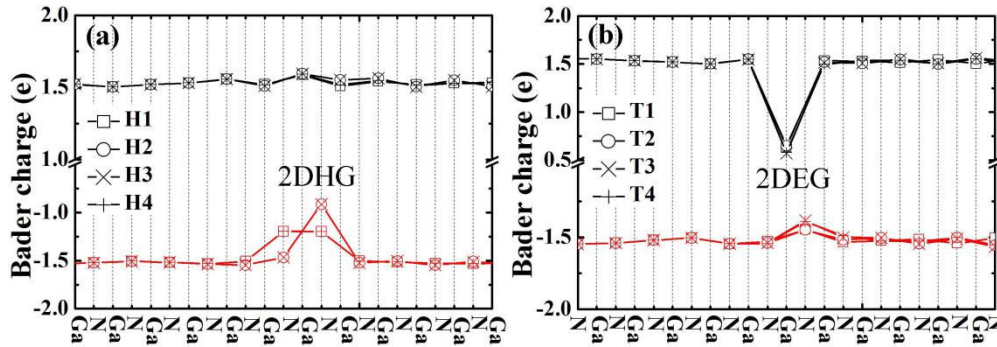


**Figure 3.3.** (a) and (b) Bader charge of each atomic layer with H and T IDB structures in GaN. Black and red solid lines are guide for eyes. The values have been subtracted from the background of bulk values.

**Table 3.2.** Net Bader charge values at the corresponding atom layers in IDBs with respect to Figure 3.3 for those compounds.

IDB	Net Bader charge (e)			
	AlN	GaN	InN	ZnO
H1/H4	+0.57	+0.32	+0.2	+0.18
H2/H3	+1.15	+0.61	+0.52	+0.4
T	-1.35/+0.15	-0.9/+0.11	-0.7/+0.08	-0.49/+0.09



## 3.5 Electron Structure of IDBs

### 3.5.1 Band Structure

The influences in electron structures resulting from IDB defect are mainly contributed by cation d electrons and the anion 2p electrons at the valence band edge. However, the conventional DFT-GGA method overestimates the interaction of semicore cation d states and the anion p-derived valence states due to the discontinuities in derivative of the exchange-correlation energy, and consequently pushes up the valence band maximum (VBM) and decrease the band gap [23,24]. Particularly in the case of InN, a wrong metallic ground state is predicted (see band structure of InN in Figure 3.4). To this end, on-site U Coulomb interactions are used both on cation d electrons and anion p electrons to reduce the d-p coupling interaction for the discussed compounds.

For group III-nitrides, the VBM and the conduction band minimum (CBM) are mainly contributed by N orbitals, and the d states of Ga and In are located near the bottom of valence band, more than 10 eV below the VBM, the band gap is more sensitive to the  $U(N)$  value. Therefore, a test of  $U_{N:2P}$  value was firstly performed in a wide range. Based on the best value of  $U(N)=5$  eV, an extra correction test on d orbital was attempted. The U parameters:  $U(Ga) = 10$  eV,  $U(In) = 1.9$  eV,  $U(Zn) = 8.5$  eV,  $U(N) = 5$  eV were determined since the change of defect states at VBM is small. The large U of Ga results from the more localized nature of 3d state compared to In, where the 4d electrons are more efficiently screened by the In core electrons. In ZnO, the overestimation of p-d coupling still exist at VBM, but the position of Zn:3d state is located at the middle of valence band, higher than the position of group III-nitrides. Depending on the previous report [25], we choose  $U(Zn:3d) = 8.5$  eV for the electronic structure calculation.

Figure 3.4 shows a quantitative change of GaN, InN and ZnO band structure along the high symmetry lines of hexagonal Brillouin zone with GGA+U and GGA approximation. In agreement with the previous reports [23-27], the GGA+U method significantly improves the band gap ( $E_g$ ) of GaN to 2.75 eV compared to the  $E_g = 1.86$  eV using GGA method. Besides, the d states are pushed down by more than 1 eV using U correction with respect to the VBM and bear now less dispersion, which suggests an increased localized character. Moreover, the p-d interaction is even smaller now although the d states are located at more than 12 eV below the VBM.

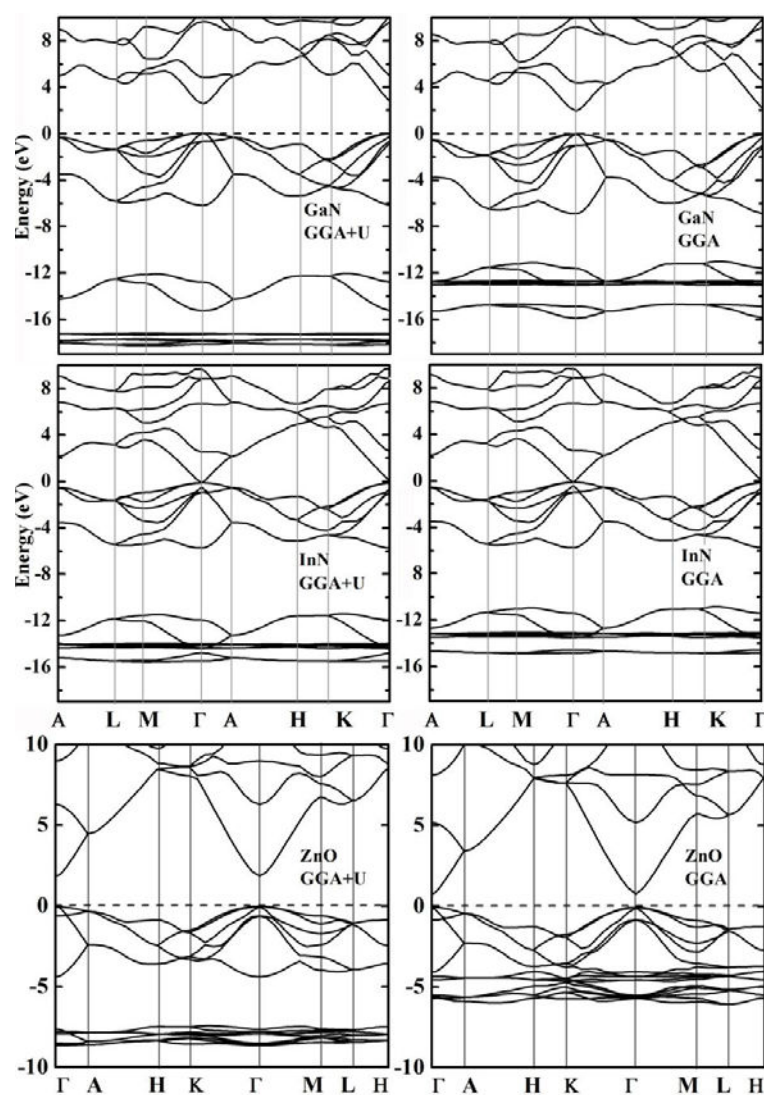


**Figure 3.4.** Calculated band structure of GaN, InN and ZnO unit cell predicted by the GGA +U ( $U_{Ga:3d} = 10$  eV,  $U_{In:4d} = 1.9$  eV,  $U_{Zn:3d} = 8.5$  eV and  $U_{N:2p} = 5$  eV) as well as the GGA method. The energy of VBM is set to zero in each case.

Similarly for InN, as the 4d states are efficiently screened by In core electrons, a minor improvement is obtained with the band gap increased from -0.011 eV to 0.00 eV and with the position of d states pushed down by around 0.7 eV. The calculated band gap of AlN is 4.2 eV which is consistent with typical theoretical value using U calibration [27]. The Zn: 3d state is more sensitive to U correction, as we can see, the band gap calculated using GGA+U method is 1.86 eV, which is a significant improvement over the GGA method with the band gap of 0.80 eV and also conforms to the archetypical theoretical values using U calibration method [23]. In particular, the GGA+U calculation yields a slightly smaller dispersion of the lowest band which is predominantly originating from Zn:3d states. The anion p band (mainly from O:2p) just above is no longer pushed up towards conduction band bottom and the p-d interaction are smaller now. It has to be pointed out that one should not expect a perfect band alignment with this on-site Coulomb correlation, the application of U calibration was mostly motivated by the aim to prevent the overestimation of p-d interactions at VBM.

### 3.5.2 Projected Density of States (PDOS)

Now we turn to discuss the influence of IDBs on electronic structures by means of the partial density of states (PDOS). Consistent with the bonding and charge transfer, H1/H4, H2/H3 and all the T types show, respectively, very similar characters in the four compounds. Therefore, only PDOS of interfacial cation-anion bonding atoms in H1, H2 and T1 IDBs are depicted in Figure 3.5 in the energy range from -7 eV to 3 eV. All the IDBs exhibit a metallic character with non-zero DOS at Fermi level position. The cation d electrons (of Ga, In and ZnO) play an important role in hybridization at VBM which is supported by both experimental measurement using x-ray photoelectron spectroscopy [28] as well as theoretical calculations [29]. Independent of the atomic species, this metallic behavior of H IDBs mainly originates from the hybridization states of cation d states and N 2p states around Fermi level as seen in Figure 3.5. The empty hybridization states at VBM just above Fermi level indicate a p type interface with hole carriers at H boundaries, which is consistent with the Bader charge analysis

in Figure 3.3(a). As compared to the group III-nitrides, the Zn: 3d orbital exhibits higher density and is dominant for the hybridization states at the valence band. This is consistent with the band structure character unveiled in Figure 3.4, in which the Zn:3d electrons are located at higher energy rang (more close to the valence band edge) than the other cation d electrons.

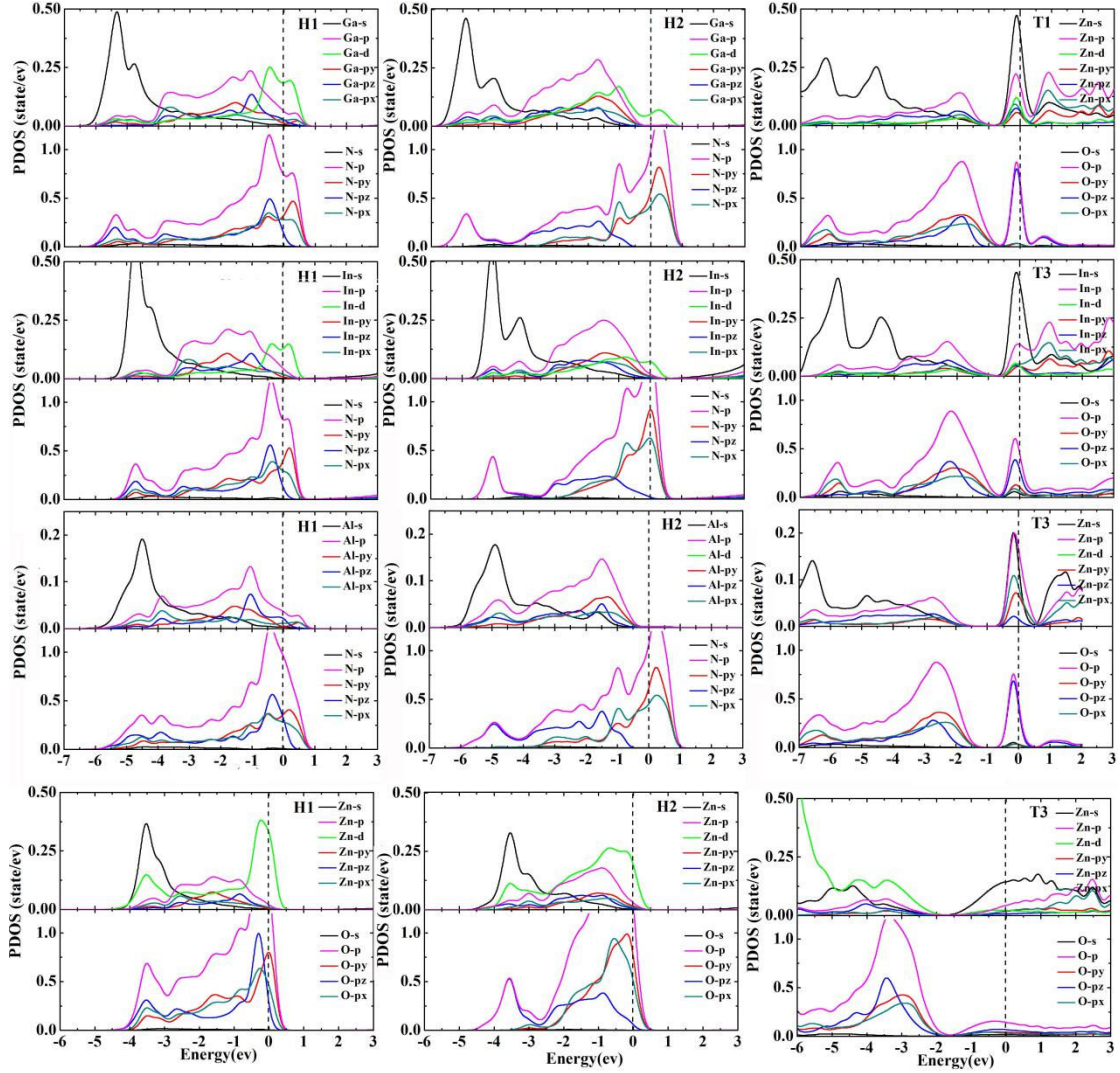


**Figure 3.5** Calculated PDOS of Ga-N, In-N and Al-N and Zn-O bonding atoms in regions of H1, H2 and T1 IDBs. The Fermi level is specified to zero in each case. In H1 IDBs, the interfacial cation and the anion just below are chosen to plot the PDOS. For H2 and T1 IDBs, the interfacial N and the cation below are used.

The partial DOS of anion: 2p orbital in px, py, pz direction is further calculated by projecting the wave functions onto spherical harmonics within spheres of a radius around each ion to investigate the electronic contribution. As shown in Figure 3.5, the

distribution of the anion: 2p electrons at the valance band edge is very dependent on topological structures of IDBs. Indeed, the cation d states hybridize with all projected p states (N/O: px, py, pz states) at the valence band edge crossing the Fermi level in H1/H4 IDBs. Whereas in H2/H3 IDBs, only N/O: px and py states are found to hybridize with cation d states at band edge of valance band. The N: pz states remain unchanged with respected to that of perfect structures. Considering the topological configurations of H IDBs, the interfacial cations at H1/H4 IDBs are located at octahedral sites and bond with their adjacent N atoms in tetrahedral positions. Therefore, the number of cation-anion bands, as well as the bond angles, deviate from the perfect wurtzite structure. So that the N/O: p states in all directions follow the same deviation. The interfacial N/O atom in H2/H3 IDBs linearly bonds with their adjacent two cations to achieve the cation-N-cation bond chain in z direction but the cations are located at normal tetrahedral positions. Therefore, the N/O: pz states stay identical as in perfect crystal, while N p states in x and y directions deviate.

As for the T IDBs, the band gap reduces, and an extended band is generated with a strong hybridization peak contributed from cation s electrons and p electrons as well as anion p electrons crossing Fermi level. The DOS of cation are remarkably intense at this band edge. This demonstrates a metallic character in all the T IDBs which agrees with the electron accumulation as already depicted by ELF and Bader charge analysis.

### 3.6 Conclusion

In this work, we presented systematic calculations on energetics, interfacial bonding properties as well as electronic structures of eight (0001) plane IDBs in group III-nitrides (AlN, GaN and InN) and ZnO homogeneous compounds. The energetic comparison shows that, among H IDBs, H4 is the most stable in GaN and InN, but not in AlN due to the lattice deformation. As for T types, T2 one is the most energetically favorable configuration in the three compounds. ELF and Bader charge analysis clearly indicate a formation of 2DHG and 2DEG in H and T IDBs, respectively. This charge

transfer is mainly attributed to the polarity discontinuity across the IDBs and to strain effects. The electronic structures corrected by on-site Coulomb interaction ( $U$ ) exhibit a metallic character in all IDBs with none-zero DOS crossing Fermi level position. The hybridization states of valance band edge cross the Fermi level in H boundaries indicating hole excess interfaces. As for T types, the PDOS is extended in density with the Fermi level shifted up above the conduction band minimum (CBM) which corresponds to an electron accumulation in boundaries consistent with ELF and Bader charge results.

## References

- [1] S. Nakamura, III-V nitride-based light-emitting diodes, *Doam. Relat. Mater.* **5** 496-500 (1996).
- [2] J. E. Northrup, *Appl. Phys. Lett.* **82**, 2278-2280 (2003).
- [3] Y. J. Cho, Z. Y. Hu, K. Nomoto, H. G. Xing, and D. Jena, *Appl. Phys. Lett.* **110**, 253506 (2017).
- [4] V. Potin, P. Ruterana, and G. Nouet, *J. Appl. Phys.* **82**, 2176 (1997).
- [5] A.D. Westwood and M.R. Notis, *J. Am. Ceram. Soc.* **74**, 1226 (1991).
- [6] J. Jasinski, Z.L. Weber, H. Lu, and W.J. Schaff, *Appl. Phys. Lett.* **85**, 233 (2004).
- [7] L.T. Romano, J.E. Northrup and M.A. O'Keefe, *Appl. Phys. Lett.* **69**, 2394 (1996).
- [8] J. C. Kim and E. Goo, *J.Am.Ceram.Soc.* **73**, 877 (1990).
- [9] S.Q. Li, H. P. Lei, Z. Wang, J. Chen, P. Ruterana, *Phys. Status Solidi B* **255**, 1700429 (2018).
- [10] J.P. Perdew, K. Burke, and Y. Wang, *Phys. Rev. B* **54** 16533 (1996).
- [11] J.P. Perdew, K. Burke, and M. Ernzerhof, *Phys. Rev. Lett.* **77** 3865 (1996).
- [12] M. Cococcioni, S. de Gironcoli, *Phys. Rev. B* **71** 035105 (2005).
- [13] G. Kresse and J. Joubert, *Phys. Rev. B.* **59**, 1758 (1999).
- [14] Y. Yan and M.M. Al-Jassim, *Phys. Rev. B* **69** 085204 (2004).
- [15] H. Blank, P. Delavignette, R. Gevers and S. Amelinckx, *Phys. Status Solidi* **7**, 747 (1964).

- [16] C. Stampfl and C.G. Van de Walle, Phys. Rev. B 57 R15052 (1998).
- [17] B. Silvi and A. Savin, Nature 371, 683 (1994).
- [18] A. Savin, O. Jepsen, J. Flad, O.K. Andersen, H. Preuss, H. G. Von Schnering, Electron Localization in Solid-state Structures of the Elements-the Diamond Structure. Angewandte Chemie-International Edition in English **31**, 187, (1992).
- [19] W. Kutzelnigg, in: Von R.F.W. Bader (Ed.), Atoms inMolecules: A Quantum Theory, Reihe: International Series of Monographs on Chemistry, vol. 22, Clarendon Press,Oxford, 1990.
- [20] F. Schuster, B. Laumer, R.R. Zamani, C. Magen, J.R. Morante, J. Arbiol, M. Stutzmann, ACS Nano, 8, 4376 (2014).
- [21] F. Bernardini, V. Fiorentini, D. Vanderbilt, Phys. Rev. B 56 R10024 (1997).
- [22] A. Zoroddu, F. Bernardini and P. Ruggerone, Phys. Rev. B 64 045208 (2001).
- [23] A. Janotti, D. Segev, C.G. Van de Walle, Phys. Rev. B 74, 045202 (2006).
- [24] T. Zakrzewski, P. Boguslawski, J. Alloys Compd. 664 565 – 579 (2016).
- [25] J. Lei, D. P. Zhu, M. C. Xu, S. J. Hu, Phys. Lett A 379, 2384 (2015).
- [26] J. Kaczkowski, Acta Phys. Polon. A 121 1142 – 1144 (2012).
- [27] C. Bacaksiz, H. Sahin, H.D. Ozaydin, S. Horzum, R.T. Senger, F.M. Peeters, Phys. Rev. B 91 085430 (2015).
- [28] L. Ley, R.A. Pollak, F.R. McFeely, S.P. Kowalczyk and D.A. Shirley, Phys. Rev. B 9, 600 (1974).
- [29] S. Strite, Jpn. J. Appl. Phys. 33 L699 (1994).

## Chapter 4

### **Experimental and Theoretical Investigation of the (0001) Plane IDBs at ZnO/GaN heterointerface**

#### 4.1 Introduction

The last two decades have shown intensive research on wurtzite semiconducting materials, primarily the group III-nitrides and ZnO, for a wide range of potential applications, such as high efficiency light emitters [1], high-power, high-frequency transistors [2,3], as well as spintronic devices [4]. Indeed, a whole industrial field was opened for solid state lighting based on GaN, as soon as reliable p-type doping with Mg has been established [5]. Of course this is not yet the case in ZnO for which efficient p-doping is still a challenge, notwithstanding its large exciton binding energy [6].

Recently, ZnO-based heterojunction concept is introduced to operate 2DEG with a sheer carrier density of  $10^{13} \text{ cm}^{-3}$  at heterointerface without the need of doping [7], which extends its application into heterojunction field-effect Transistors (HFET), such as: ZnMgO/ZnO HFET, the electron mobility is reported to reach as high as  $10^6 \text{ cm}^2 \text{V}^{-1} \text{s}^{-1}$  at low temperature [8]. While, limited availability and high price of native ZnO substrate necessitate establishing growth of high-quality ZnO structure on foreign substrates, for instance III-nitrides [9],  $\text{Al}_2\text{O}_3$  [10,11] and SiC [12]. However, due to the large lattice mismatch, the epitaxial ZnO layers are always plagued with high densities of extended defects inherent to the wurtzite structure [13-15]. Detrimental effects of these defects on the performances of the related devices have been the subject of numerous reports [16-20]. For instance, the basal and prismatic stacking faults in ZnO were reported to exhibit low formation energies, and tend to coexist with large densities of point defects [13-14]. For the prismatic  $\{10\bar{1}0\}$  inversion domain boundary (IDB) which exhibits two stable atomic configurations [21-24], it has been found that this type of boundary does not induce electronic states in band gap, but could attract



charged point defects and build up an electrical potential for the minority carriers in both p- and n-type ZnO [15]. Obviously, in order to fabricate high performance devices, it is necessary to fabricate high quality ZnO thin films. To further improve the structural perfection of ZnO films, (0001)-GaN/c-sapphire template is considered as one of the best substrates for epitaxial growth, since the 1.8% of the lattice mismatch between GaN and ZnO is ten times smaller than that with sapphire. This improvement for high quality ZnO film growth would indeed open the way for optimization of devices performance [25]. The predicted electron velocity in bulk ZnO reaches to  $3.1 \times 10^7$  cm/s [26,27], exceeding that in GaN ( $2.9 \times 10^7$  cm/s) [28]. When combined with inexpensive epitaxial technology, this feature makes ZnO an attractive choice for high-power, high-frequency FETs (note that p-type problem is not an obstacle for these unipolar devices relying on electron conduction). In particular, theory predicts superior performance of ZnO-based FETs in THz-range as compared to GaAs [27].

The realization of full potential of ZnO-based heterostructures on GaN in electronic devices requires an insight into the properties of the ZnO/GaN heterointerfaces at atomic scale. At the interface, one not only faces purely crystallographic and chemical relationship, but also requires a precise control on the polarity relationship. As an example, in a number of reports published on the luminescence properties of p-GaN/n-ZnO heterojunctions, the emission was observed either from the GaN [29,30] or the ZnO side [31,32]. However, as was reported by Schuster et al. for nearly defect-free p-GaN/n-ZnO nanowires [33], strong excitonic UV emission originating from the ZnO-side of the interface as well as stimulated emission can be controllably attained from the ZnO side. Until now, attempts to attain a control of the layer polarity at the ZnO/GaN heterostructure are scarce, mainly consisting in the insertion of ultrathin (4 nm)  $\text{Ga}_2\text{O}_3$  which helped to change the polarity of the overgrown ZnO to O-polar on top of a Ga-polar template [34,35]. However, for device application, an abrupt and clean interface between the two semiconductors is the most efficient way to achieve the best performance. In this vein, early attempt to grow Ga-polar GaN on O-polar ZnO by pulsed laser deposition reported that this could take place at room temperature, while it

was necessary to use low temperature buffer layer in order to achieve similar result at 700° C [36,37]. It is only recently that, by close tuning of the growth conditions in molecular beam epitaxy (MBE), one may obtain complete reversal of polarity of a ZnO layer growing on a Ga-polar GaN template within one monolayer [38]. But the details of atomic structures of this ZnO/GaN heterointerface and the corresponding physical properties have not been clarified yet. Clearly, this ZnO/GaN heterointerface is (0001) plane IDB and a number of reports on its investigation mainly focus on polycrystalline wurtzite BeO [39] and ZnO [40] using either optical or high resolution transmission electron microscopy. In agreement with the geometrical models proposed by Kim and Goo [40], the study of the surface energy points out to the eight atomic configurations of the (0001) IDB in wurtzite. However, until now, no systematic investigation of their structural, energetic and electronic stability has been reported, neither has been reported a detail experimental analysis of the stable atomic structure.

In this chapter, we report on a systematic investigation of a one monolayer transition from Ga-polar GaN to O-polar ZnO heterostructure using STEM, particularly in the high angle annular dark field and annular bright field mode (HAADF, ABF) in order to clarify the atomic structure and chemical composition. To gain insight into the genesis of the experimental observations, a detailed theoretical analysis based on density functional theory is used to elucidate the chemical bonding character and electron property of the heterointerfaces.

## 4.2 Samples

ZnO films were grown by plasma enhanced molecular beam epitaxy (P-MBE). Highly resistive (60 kΩ.mm), carbon-compensated 2.5-μm Ga-polar (0001) GaN layers prepared by metalorganic chemical vapor deposition on c-plane sapphire served as substrates. Prior to loading into the MBE system, the GaN templates were cleaned with aqua regia to remove possible metal contamination followed by immersion in a HCl:H<sub>2</sub>O = 1:1 solution to remove any gallium oxide (Ga<sub>2</sub>O<sub>3</sub>) from the surface. After loading the substrate to the growth chamber, GaN surface was thermally cleaned at 625°C

for 15 min followed by an exposure to Zn beam to terminate the GaN surface with Zn adatoms [38]. The same Zn flux of  $0.1 \text{ \AA/s}$  was maintained during cool down and the growth of low-temperature (LT) ZnO nucleation layer of thickness 25 nm at  $T_g = 300^\circ\text{C}$ . During the LT ZnO growth, the oxygen-to-Zn ratio (VI/II ratio in the following discussion) was varied via varying the O flux within a wide range, from deep Zn rich (VI/II = 0.55) to deep oxygen rich (VI/II = 3) conditions. After annealing the LT-ZnO layer at  $730^\circ\text{C}$  for 5 min at  $1 \times 10^{-5}$  Torr reactor pressure with closed O-plasma shutter, ZnO growth proceeded at  $670^\circ\text{C}$ . For all the samples under investigation, Zn flux and oxygen gas flow during the high temperature (HT) ZnO growth were kept at  $0.25 \text{ \AA/s}$  and 0.7 sccm, respectively. 400W RF power of the plasma cell was used for both the LT- and the HT-ZnO growth. The growth time for HT ZnO was 2 hours and total film thickness for the samples nucleated with VI/II ratio below 1.5 is around 365 nm and for those nucleated with larger VI/II ratio is 175nm. Figure 4.1 exhibits the sample structure. The heterointerface of ZnO/GaN can be seen as a high contrast line pointed out by red rectangle.

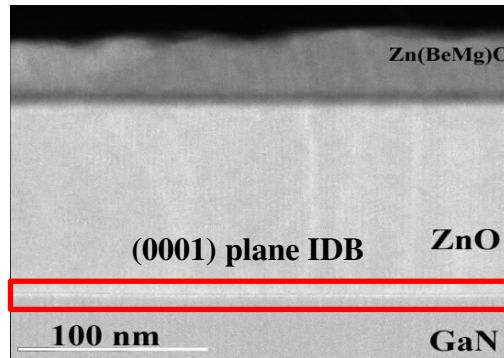


**Figure 4.1.** Sample structure of ZnO/GaN heterointerface. Red rectangle points out the interface

As we have reported previously [38], O/Zn ratio higher than the critical value of 1.5 gives rise to the nucleation of O-polar ZnO films, and it turns out that this polarity inversion at nucleation takes place at the whole wafer surface and thus results in a ZnO layer with an reversed polarity to that of the underlying GaN. Herein, the studied O-polar ZnO/Ga-polar GaN heterostructure was prepared at a high O/Zn ratio of 6.0 to verify the occurrence of polarity inversion. A Zn-polar ZnO/Ga-polar GaN nucleated

at low O/Zn ratio was investigated for comparison.

### 4.3 TEM Observations

High angle annular dark field (HAADF, collection angles of 75-309 mrad) and annular bright field (ABF, collection angles of 11-24 mrad) analysis were carried out in double Cs corrected JEOL ARM 200CF scanning transmission electron microscope (STEM) to determine the atomic stacking and elemental composition across the ZnO/GaN heterointerface. A semi-convergence angle of 20.4 mrad was used, giving rise to a probe size of 0.8 Å. To improve the signal-to-noise ratio and minimize the image distortion, 10 serial frames were acquired with a short dwell time (2 µs per pixel). Multiple images were then aligned and superimposed.[41]

TEM investigation on polarity inverted ZnO/GaN heterointerface is shown in Figure 4.2. As pointed out by white arrow (HAADF image of Figure 4.2(a)), only one monolayer in this ZnO/GaN heterointerface exhibits a change in contrast, which originates from the abrupt transition from GaN to ZnO. Further in GaN template and ZnO epilayer, the change of stacking sequence, as illustrated by blue dots and lines, reveals the occurrence of polarity inversion between two layers [41]. In the ABF image recorded simultaneously (Figure 4.2(b)), a clear atomic resolution is obtained and the light atom positions are now well visible. The characteristic polarity dumbbell pairs of wurtzite crystal are resolved with the presence of the lighter contrast zigzag below or above the darker atomic positions (Ga, Zn). The interface plane comes out as only one monolayer which exhibits a different geometry with respect to the perfect wurtzite structure. Otherwise, on each side of the interface, the hexagonal ‘-ABAB-’ stacking is clearly preserved and the polarity can be identified as O-polar in ZnO and Ga-polar in GaN, respectively. Figure 4.2(c) is the superimposition of HAADF and ABF images in which the large green spots correspond to intensities where the metal atoms are dominant. Now the abrupt ZnO/GaN heterointerface is evidently identified as a contribution of metal layer. And the whole stacking sequence of the heterostructure can

be directly deduced to AaBbA-cCaAc (H4 IDB) by following the same definition in reference [40]. The corresponding atomic model is seen in Figure 4.2(d).

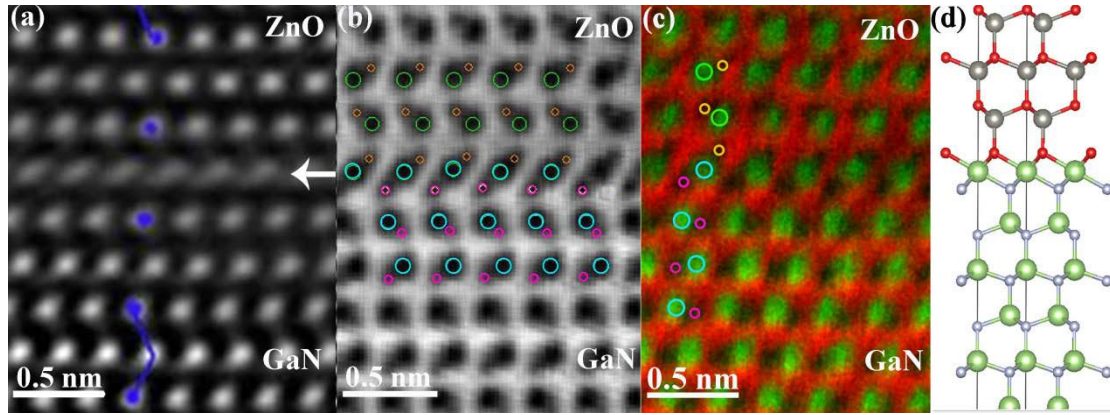


**Figure 4.2.** STEM images of O-polar ZnO/Ga-polar GaN heterointerface. (a) HAADF image of O-polar ZnO/Ga-polar GaN heterointerface. The white arrow shows the interface. The blue dots and lines underline the stacking sequences. (b) Simultaneous ABF image where atoms have been superimposed. Big circles indicate metal atoms and small circles denote nonmetal atoms. (c) Overlap of the HAADF and ABF images showing the interface configuration. (d) Corresponding atomic model of the (0001) plane IDB.

When the polarity inversion was not initiated by tuning the right O/Zn ratio, the polarity of substrate extends to ZnO epilayer and the interface geometry is completely preserved. As seen in HAADF image of Figure 4.3(a), only a faint change in chemical contrast permits to delineate the ZnO/GaN interface (see white arrows). The corresponding ABF image (Figure 4.3(b)) displays a perfect transfer of cation-anion sequence through the interface. This polarity continuity also can be underlined directly in superimposition of HAADF and ABF images (Figure 4.3(c)) in which a Zn-polar ZnO/Ga-polar GaN heterostructure is shown.

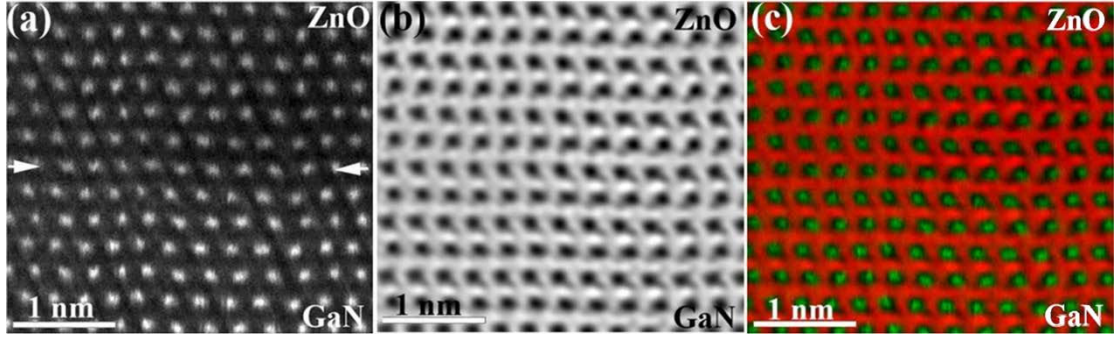


**Figure 4.3.** STEM images of Zn-polar ZnO/Ga-polar GaN heterointerface, (a) HAADF image where the interface position is pointed out by the white arrows. (b) ABF image recorded on the same area as in (a). (c) A superposition of the HAADF and ABF images showing the continuous polarity.

Although the TEM observations clearly displayed the geometry of ZnO/GaN heterointerface and proved that the inversion operation has taken place at a metal atomic layer, the exact elemental composition of the interfacial monolayer (cation-anion) should be subjected to a more intimate examination. Considering the reduced surface mobility in MBE process with low temperature (300°C) growth [38], we may suspect that mixtures of atomic species (Zn/Ga, O/N) at the interface should remain at the level of dopants, and shall not be considered in modelling the dominant properties of the (0001) plane IDB at heterointerface. Moreover, since the GaN surface was thermally pre-cleaned at high temperature and the use of O/Zn ratio flux is high as 6.0, one may conclude that the growth was initiated with a Ga-terminated surface leading to a -N-Ga-O-Zn- (type-A) interface alignment. However, we could also consider the extreme case of a monolayer shift of the interface to the next layer to form a -Ga-N-Zn-O- (type-B) interface. From the above points, for each IDB model, two types of interfaces (type-A and type-B) are considered in the following simulation sections. For convenience, the simplified expression in form of H(A) IDB is also used to represent an H IDB with type-A interface in following discussion

## 4.4 Theoretical Modeling of (0001) Plane IDBs in ZnO/GaN heterostructure

First-principle calculations are performed using the Vienna Ab-initio Simulation Package (VASP) [42,43]. The exchange correlation functional adopts the generalized gradient approximation (GGA) with Perdew-Burke-Ernzerhofer (PBE) scheme. The interaction between core and valence electrons are described by the projector augmented-wave (PAW) method [44]. A  $21 \times 21 \times 1$  Monkhorst-Pack Gamma mesh is applied for Brillouin zone sampling; the tolerance of energy and force convergence is set to  $10^{-6}$  eV and  $10^{-2}$  eV/Å, respectively.

The IDBs are constructed using the slab model with consideration of two type interfaces (type-A and type-B). Each supercell contains only one boundary at interface with nine bi-layers on both sides along [0001] direction. The detailed interface alignment can be seen in Figure 4.5 (type-A interface) and Figure 4.6 (type-B interface). The use of slab scheme implies a infinite planar defect on (0001) plane. Pseudo-Hydrogen atoms with fractional charge are used to saturate the terminated surface and a vacuum layer of 24.4 Å thickness is set to avoid the artificial interaction between image slabs [45]. During the structural relaxation, the top two bi-layers of GaN and the whole ZnO epilayer are relaxed whereas the rest of GaN atoms are fixed at their bulk positions to simulate the substrate.

## 4.5 Energetic Stability

The thermodynamical stability of the sixteen IDBs is evaluated by computing their relative formation energies  $\gamma_{form}$  as introduced in chapter 2 (section 2.6.2) [22]:

$$\gamma_{form} = \Delta E - \Delta n_O \mu_O - \Delta n_{Zn} \mu_{Zn} - \Delta n_N \mu_N - \Delta n_{Ga} \mu_{Ga} \quad (4.1)$$

where  $\Delta E$  is the energy difference of a supercell containing one IDB relative to the reference structure with bulk stacking sequence at ZnO/GaN heterointerface.

$\Delta n_{O(Zn,N,Ga)}$  is correspondingly the variation of individual atom number in those supercells.  $\Delta\mu_{O(Zn,N,Ga)}$  is the chemical potential of the constituent O (Zn, N, Ga) referenced to elemental solid/gas phase.

The chemical potential of different species is difficult to determine directly in a given experimental process from theoretical method. Even so, under thermal equilibrium growth condition, there are some thermodynamic limits on the chemical potential which can be used to estimate the energy range.

In bulk ZnO, the relation is:

$$\mu_{Zn_2O_2}^B = 2\mu_O + 2\mu_{Zn} = 2\mu_{Zn}^B + 2\mu_O^g - \Delta H_{Zn_2O_2} \quad (4.2)$$

Among,  $\mu_{Zn}^B$  is the chemical potential of bulk Zn in hexagonal phase.  $\mu_O^g$  is the chemical potential of O (gas phase).  $\Delta H_{Zn_2O_2}$  is the formation energy of bulk ZnO .

For bulk Zn<sub>3</sub>N<sub>2</sub>, It corresponds to:

$$\mu_{Zn_{48}N_{32}}^B = 48\mu_{Zn} + 32\mu_N = 48\mu_{Zn}^B + 32\mu_N^g - \Delta H_{Zn_{48}N_{32}} \quad (4.3)$$

where  $\mu_{Zn}^B$  is the chemical potential of bulk Zn (hexagonal phase).  $\mu_N^g$  is the chemical potential of N (gas phase).  $\Delta H_{Zn_{48}N_{32}}$  is the formation energy of bulk Zn<sub>3</sub>N<sub>2</sub>.

For bulk GaN, the relation is:

$$\mu_{Ga_2N_2}^B = 2\mu_{Ga} + 2\mu_N = 2\mu_{Ga}^B + 2\mu_N^g - \Delta H_{Ga_2N_2} \quad (4.4)$$

where  $\mu_{Ga}^B$  and  $\mu_N^g$  are the chemical potential of bulk Ga in orthorhombic phase and of N in gas phase.  $\Delta H_{Ga_2N_2}$  represents the formation energy of bulk GaN crystal.

As for bulk Ga<sub>2</sub>O<sub>3</sub>, it is:

$$\mu_{Ga_8O_{12}}^B = 8\mu_{Ga} + 12\mu_O = 8\mu_{Ga}^B + 12\mu_O^g - \Delta H_{Ga_8O_{12}} \quad (4.5)$$

where  $\mu_{Ga}^B$  and  $\mu_O^g$  are the chemical potential of bulk Ga in orthorhombic phase and of O in gas phase. Correspondingly,  $\Delta H_{Ga_2O_3}$  is the formation energy of Ga<sub>2</sub>O<sub>3</sub> bulk.

For H1-H4(A) and T1-T4(A) IDBs, the relative formation energy can be simplified as:

$$\gamma_{form} = \Delta E \quad (4.6)$$



The relative formation energy of H1/H4(B) IDBs is:

$$\gamma_{form} = \Delta E + (\mu_{Ga} - \mu_{Zn}) \quad (4.7)$$

Under the N-rich condition (as we have N-Zn interface), the value of  $\mu_N$  is equal in GaN and  $Zn_3N_2$  system under thermal equilibrium. According to Eq.(3) and (4), the chemical potential difference of  $\mu_{Ga} - \mu_{Zn}$  is

$$\mu_{Ga} - \mu_{Zn} = (8\mu_{Ga}^B - \mu_{Zn}^B) + \frac{1}{3}(\mu_N^g - \mu_N) - \frac{1}{2}\Delta H_{Ga_2N_2} + \frac{1}{48}\Delta H_{Zn_{48}N_{32}} \quad (4.8)$$

The lower limit of  $\mu_{Ga} - \mu_{Zn}$  is given when  $\mu_N$  takes the maximum value  $\mu_N^g$ :

$$\mu_{Ga} - \mu_{Zn} > (\mu_{Ga}^B - \mu_{Zn}^B) - \frac{1}{2}\Delta H_{Ga_2N_2} + \frac{1}{48}\Delta H_{Zn_{48}N_{32}} = -2.7431$$

and the upper limit can be determined when  $\mu_{Ga} = \mu_{Ga}^B$  and  $\mu_N = \mu_N^g$ :

$$\mu_{Ga} - \mu_{Zn} < \mu_{Ga}^B - \left( \mu_{Zn}^B - \frac{1}{48}\Delta H_{Zn_{48}N_{32}} \right) = -1.7585$$

Therefore, for H1/H4(B) IDB, the restriction is  $-2.7431 < \mu_{Ga} - \mu_{Zn} < -1.7585$ .

In H2/H3(B) and T1-T4(B) IDBs, the relative formation energy is:

$$\gamma_{form} = \Delta E + (\mu_O - \mu_N) \quad (4.9)$$

In thermal equilibrium, during the growth of ZnO on GaN,  $\mu_{Ga}$  is the same as in  $Ga_2O_3$  and in GaN. Then according to the Eq.(4.4) and (4.5):

$$\mu_O - \mu_N = (\mu_O^g - \mu_N^g) + \frac{1}{3}(\mu_{Ga} - \mu_{Ga}^B) - \frac{1}{12}\Delta H_{Ga_8O_{12}} + \frac{1}{2}\Delta H_{Ga_2N_2} \quad (4.10)$$

The upper limit of  $\mu_O - \mu_N$  is obtained when  $\mu_{Ga} = \mu_{Ga}^B$ , namely,

$$\mu_O - \mu_N < (\mu_O^g - \mu_N^g) - \frac{1}{12}\Delta H_{Ga_8O_{12}} + \frac{1}{2}\Delta H_{Ga_2N_2} = -0.3253 \quad (4.11)$$

Correspondingly, the lower limit can be determined when  $\mu_N = \mu_N^g$ :

$$\mu_O - \mu_N > (\mu_O^g - \mu_N^g) - \frac{1}{12}\Delta H_{Ga_8O_{12}} = -1.3099$$

Therefore, for H2/H3(B) and T1-T4(B) IDBs, the range of  $\mu_O - \mu_N$  is between -1.3099 to -0.3253. Table 4.3 and 4.4 show the total energies of IDB supercells and formation energies as well as chemical potentials of the species used above.

**Table 4.3.** Energy difference  $\Delta E$  of the sixteen IDBs with respect to the reference structure. The energies are given in eV.

	Type-A	Type-B		Type-A	Type-B
H1	-1.2982	2.4813	T1	-0.2799	-1.6302
H2	-0.9733	-0.4100	T2	-0.3052	-1.6164
H3	-0.9709	-0.4090	T3	-0.2204	-1.4251
H4	-1.3005	2.4798	T4	-0.2376	-1.4092

**Table 4.4.** Formation enthalpy and chemical potentials

Term	E <sub>atom</sub> (eV)	totE (eV) gas or solid	$\Delta H$ or $\mu$ (eV)
O <sub>2</sub>	E <sub>O</sub> =-1.54804765	-9.84162625 dimer	$\mu_O^g = \frac{1}{2}totE_{O_2} - E_O = -3.3728$
N <sub>2</sub>	E <sub>N</sub> =-3.10862376	-16.59638122 dimer	$\mu_N^g = \frac{1}{2}totE_{N_2} - E_N = -5.1896$
Zn <sub>2</sub>	E <sub>Zn</sub> =-0.16452753	-2.51985267 HCP	$\mu_{Zn}^B = \frac{1}{2}totE_{Zn_2} - E_{Zn} = -1.0954$
Ga <sub>8</sub>	E <sub>Ga</sub> =-0.33970202	-24.22359019 orthorhombic	$\mu_{Ga}^B = \frac{1}{8}totE_{Ga_8} - E_{Ga} = -2.6882$
Zn <sub>2</sub> O <sub>2</sub>		-18.21022507 wurtzite	$\Delta H_{Zn_2O_2} = totE_{Zn_2} + totE_{O_2} - totE = 5.8487$
Zn <sub>48</sub> N <sub>32</sub>		-318.06726164 anti-bixbyite	$\Delta H_{Zn_{48}N_{32}} = 24totE_{Zn_2} + 16totE_{N_2} - totE = -7.951$
Ga <sub>2</sub> N <sub>2</sub>		-24.62143382 wurtzite	$\Delta H_{Ga_2N_2} = \frac{1}{4}totE_{Ga_8} + totE_{N_2} - totE = -1.969$
Ga <sub>8</sub> O <sub>12</sub>		-120.79426354 $\beta$ (C2-m)	$\Delta H_{Ga_8O_{12}} = totE_{Ga_8} + 6totE_{N_2} - totE = -37.5209$

Figure 4.4 shows the relative formation energies of those IDBs with the variation of processing condition. In the results, negative value of  $\gamma_{form}$  demonstrates the relatively lower formation energy compared with the reference. For all the IDBs considered, it's

found that, the four structure pairs H1/H4, H2/H3, T1/T2 and T3/T4 IDBs exhibit very similar energy variation, respectively, independent of interface alignment. When comparing their corresponding stacking sequence, it's understandable that the structural deviation comes from the next-nearest neighbors and has small influence on the thermodynamical stability of IDBs.

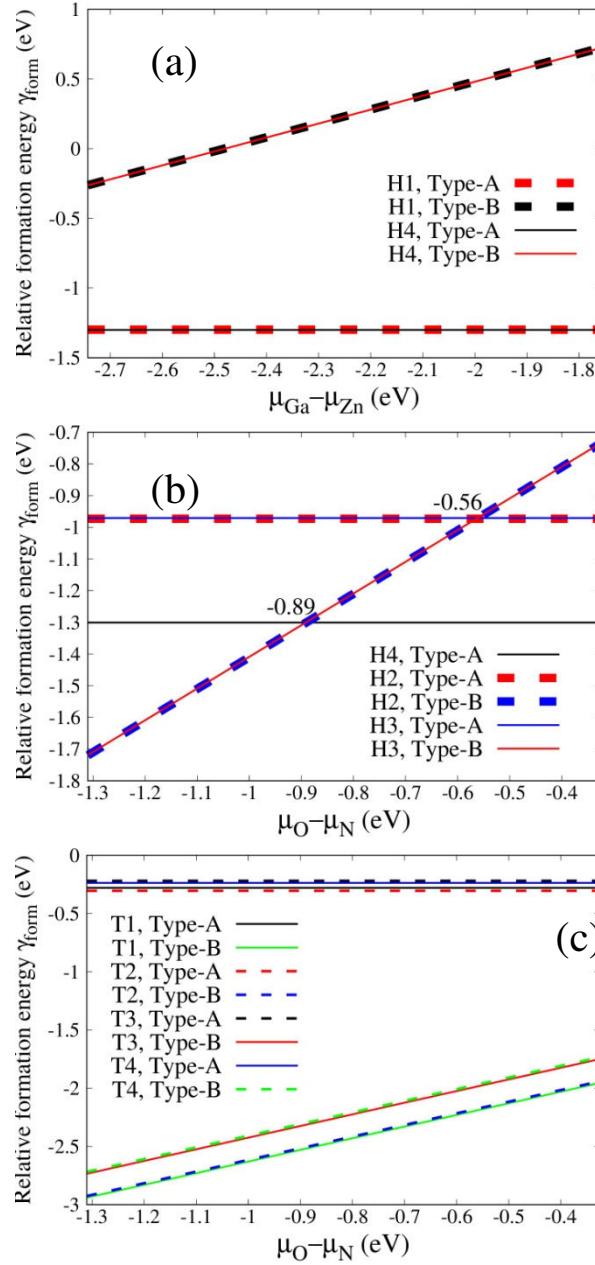


**Figure 4.4.** Relative formation energy of the (0001) plane IDBs of ZnO/GaN heterostructure with type-A and type-B interfaces: (a) H1/H4 IDBs, (b) H2/H3 IDBs in comparison to H4 IDB with type-A interface, and (c) T1-T4 IDBs, respectively.

In Figure 4.4(a), independent of the  $\mu_{Ga} - \mu_{Zn}$  variation, H1/H4(A) IDBs is more stable than H1/H4(B) IDBs, and the relative formation energy of H4(A) IDB is 2 meV lower than that of H1(A) IDB. It suggests that the H4(A) IDB is always more energetically favored than the other three IDBs. The relative formation energies of H2/H3(B) IDBs are smaller than those of H2/H3(A) IDBs when the  $\mu_O - \mu_N$  value is lower than -0.56 eV, seen in Figure 4.4(b). When the  $\mu_O - \mu_N$  value increases above -0.56 eV, H2/H3(A) IDBs become more stable. Taking the H4(A) IDB as a reference (black line in Figure 4.4(b)), it's found that H2/H3(A) IDBs always have higher formation energy namely lesser energetically favored than the H4(A) one. However, with the  $\mu_O - \mu_N$  value below to -0.89 eV, H2/H3(B) IDBs are the most stable configurations in all H IDBs. Once  $\mu_O - \mu_N > -0.89$  eV, H4(A) IDB becomes the most stable one among all H IDBs.

In regard to T IDBs, since the polarity arrangement has changed, their thermodynamic stability should be individually discussed without the comparison to H counterparts. Figure 4.4(c) clearly shows that T1/T2(B) IDBs are more stable than the other T IDBs within the whole range of chemical potential difference  $\mu_O - \mu_N$ . Additionally, between this two IDBs, the formation energy of T1(B) IDB is 14 meV smaller than T2(B) one. It means that T1 IDB with type-B interface is the most stable configuration with respect to all T IDBs in ZnO/GaN heterointerface.

Considering the growth condition of high O/Zn ratio in MBE process, the constraint of chemical potential difference  $\mu_O - \mu_N$  is larger than -0.89 eV, which indicates that the most energetically stable H4(A) IDB is the best appropriate structure to describe experimental results.

## 4.6 Chemical Bonding and Bader Population Analysis

After the atomic structure and elemental distribution of (0001) plane IDB observed by STEM (Figure 4.2) has been identified as an H4 IDB with -Zn-O-Ga-N- configuration at the ZnO/GaN heterointerface, the properties of chemical bonding and charge transfer

in vicinity of IDBs are further investigated for all possible (0001) plane IDBs in ZnO/GaN heterointerface for completeness. The corresponding analyses include ELF, and Bader charge population.

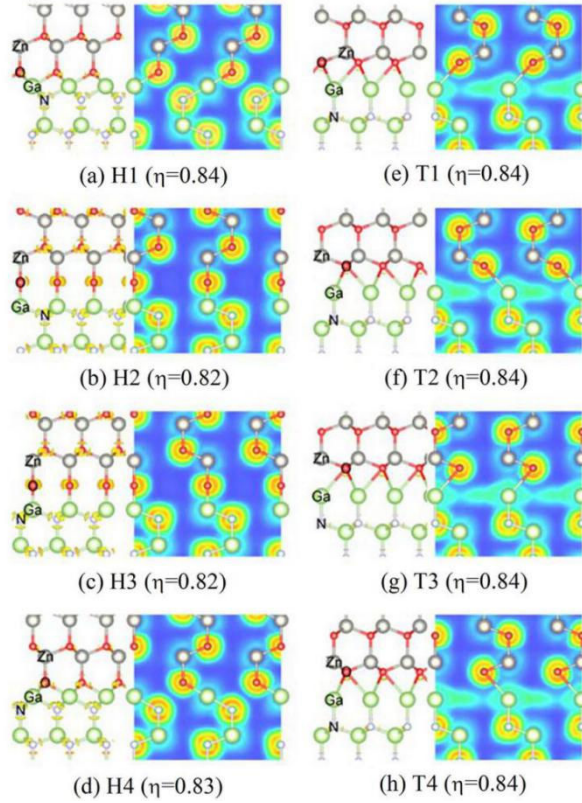


**Figure 4.5.** ELF of (0001) plane IDBs in ZnO/GaN heterointerface with type-A interface: (a)-(d) H IDBs and (e)-(h) T IDBs. In each panel the left side is ELF isosurface, while the right side is the 2D contour slice of ELF crossing  $(11\bar{2}0)$  atomic plane. Interfacial atomic alignment -Zn-O-Ga-N- is labeled by element symbols, and Zn, O, Ga and N atoms are represented by grey, red, green and silver balls, respectively.

Figure 4.5 and Figure 4.6 illustrate the ELF isosurface contour and 2D contour slice crossing  $(11\bar{2}0)$  atomic plane for the eight IDB structures with respect to type-A and type-B interfaces, respectively. As seen in GaN and ZnO bulk regions, the electron localization domains of -Zn-O- or -Ga-N- bonds localize more toward O/N atoms due to their large electronegativity. By increasing the isosurface value, those electron localization domains spatially bifurcate into four irreducible domains (yellow regions in left panels of Figure 4.5 and 4.6), named as bonding attractors, which correspond to the four bonds in perfect structure. The corresponding 2D contour slices are displayed

on right panels of Figure 4.5 and 4.6(a)-(h) using a color scheme in which the colors rang from blue through yellow to brown while ELF increases from 0 to 1. Regions of high electron localization are seen with a large brown-yellow annular region which are identified as O/N atoms. The Zn/Ga atoms are associated to a small ELF value with a light blue ring. The polarized covalent character of Zn-O and Ga-N bonds can be seen in the oval shaped localization domains of O/N atoms pointing towards Zn/Ga domains.

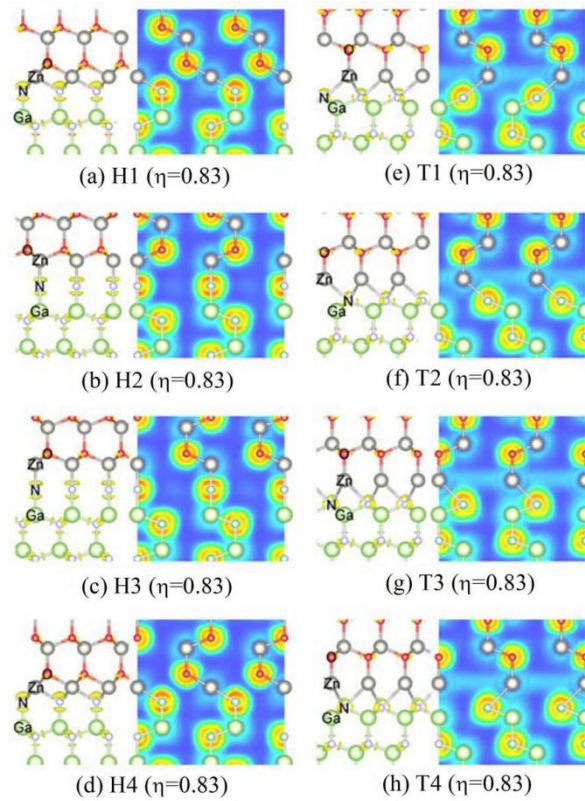


**Figure 4.6.** ELF of (0001) plane IDBs in ZnO/GaN heterointerface with type-B interface: (a)-(d) H IDBs and (e)-(h) T IDBs. Image layout keeps the same as in Figure 4.5.

In regard to H1/H4(A) IDBs, electron localization domains resolve into four bonding attractors around interfacial O/N atoms, which are consistent with those in bulk regions, as shown in the left panels of Figure 4.5(a) and (d). However, in H1/H4(B) IDBs, see left panels of Figure 4.6(a) and (d), the localization attractor along the N-Zn bonds appears to be a large domain located above N atom, deviated from tetrahedral configuration, which may respond to the high energy shown in Figure 4.4(a). As for

H2/H3(A) IDBs, the electron localization domain exhibits a spherical section around the interface O atom as shown in the left panels of Figure 4.5(b) and (c). Whereas in Figure 4.6(b) and (c), interfacial N atom at H2/H3(B) IDBs has two bonding attractors  $180^\circ$  apart which are located at the links of Zn-N and N-Ga. 2D contour slices exhibit no obvious change in H IDBs relative to the perfect crystal as described in their corresponding right panels of Figure 4.5(a)-(d) and Figure 4.6(a)-(d).

The electron localization domains of either Zn-O-Ga or Zn-N-Ga chains in T IDBs are located close to the intermediate O/N atoms and exhibit more dispersion since the O/N atoms are located at octahedral site which correspond to more nearest-neighbor atoms as shown in left panels of Figure 4.5(e)-(h) and Figure 4.6(e)-(h). Additionally, more interesting is seen that all the 2D contour slices exhibit a visible electron delocalization with the ELF value of about 0.5 at interfacial Ga/Zn atom layer in T(A/B) IDBs, which indicate the formation of homogeneous electron gas at the boundaries [46], as shown in right panels of Figure 4.5(e)-(h) and Figure 4.6(e)-(h).

Bader population analysis of each atom layer is implemented along [0001] direction to quantify the charge transfer in vicinity of IDBs. As shown in Figure 4.7(a) for all H(A) IDBs, the interfacial Ga atom has a charge of  $+1.7 e^-$ ,  $0.2 e^-$  more than the value in perfect crystal ( $+1.5 e^-$ ). This indicates a positively charged interfacial Ga layer in H(A) IDBs. Additionally, the adjacent N or O layer in H1/H4 or H2/H3 IDBs is also found to accept an extra charge of  $+0.3 e^-$  per atom in comparison to those in bulk regions, respectively. In the same vein, Bader charge shown in Figure 4.7(c) exhibits a positively charged N layer at H(B) IDBs with an additional charge of around  $+0.7 e^-$  gained by each N atom. This hole concentration at one (or even two) atom layer points to the existence of 2DHG in H IDBs. However, since the ELF does not visualize the hole density, there is no variation uncovered in 2D contour slices of ELF (right panels of Figure 4.5 and 4.6(a)-(d)).

Regarding to the T IDBs, the interfacial Ga or Zn atoms accept an extra charge of  $-1.0 e^-$  each in type-A interface and of  $-0.5 e^-$  each in type-B interface relative to those in



bulk region. And this electron accumulation in interfacial monolayer does not extend vertically to the adjacent atom layers, which strongly suggests the occurrence of 2DEG and perfectly agrees with the ELF results shown in Figure 4.5 and 4.6(e)-(h). The present DFT calculations constitute a quantum mechanical explanation of the results which were recently reported based on the effective mass approach, where the formation of interface charges attributed to the synergetic effect of piezoelectric and spontaneous polarization in such heterostructures.[34]

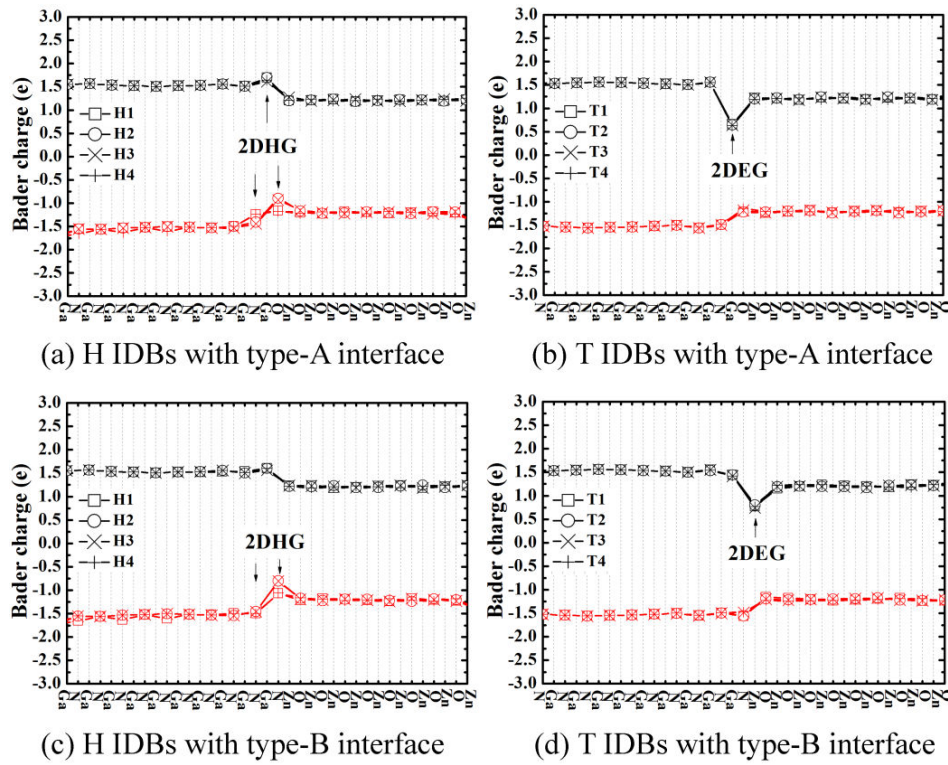


**Figure 4.7.** Bader population analysis of the (0001) plane IDBs in ZnO/GaN heterointerface: (a) H IDBs with type-A interface, (b) T IDBs with type-A interface, (c) H IDBs with type-B interface, (d) T IDBs with type-B interface.



## 4.7 Electronic Structure of IDBs

The computed partial density of states (PDOS) on individual atom layer at each IDB are plotted in Figure 4.8, in which H1/H4, H2/H3 as well as all T IDBs exhibit similar profiles within type-A and type-B interface, respectively. Moreover, the corresponding PDOS onto the p ( $p_x$ ,  $p_y$  and  $p_z$ ) orbitals of the atoms near the valence band edge are provided to further illustrate the electron contribution (see right panel of each figure).

As can be seen in Figure 4.8(a), (b), (d) and (e), all H IDBs are observed to be metallic as there is non-zero DOS across the Fermi level position. The metallic behavior of H(A) IDBs mainly comes from the contribution of Ga/Zn: 3d, 4p and N/O: 2p orbitals around the Fermi level position. The hybridization peak emerging across the Fermi level came from the strong interaction of Ga/Zn: 3d and N/O: 2p orbitals also confirms the metallic character in H(B) IDBs (Figure 4.8(d) and (e)). Combining with the ELF and Bader charge analysis above, the empty states just above the Fermi level may serve as p type interface states in H IDBs. The split PDOS onto  $p_x$ ,  $p_y$  and  $p_z$  orbitals of the interfacial atoms reveal that contributions of N/O: p orbitals on valence band edge are strongly dependent on local topology of the IDBs. As shown for H1/H4 IDBs in Figure 4.5 and 4.6(a), (d), interfacial cations are located at octahedral site and bounded with the symmetric O/N atoms in tetrahedral position. The number of cation-anion bonds and their bond angles are deviated from the perfect crystal. Therefore, the hybridization states at band edge are intensive in density with the contribution mainly comes from N/O:  $p_x$ ,  $p_y$ ,  $p_z$  orbitals below 0 eV; while the hybridization states above the Fermi level are originated from N/O:  $p_x$  and  $p_y$  orbitals. In H2/H3 IDBs which have linear atomic chain in z direction with the cations located at tetrahedral site (seen in Figure 4.5 and 4.6(b) and (c)), the  $p_z$  orbitals of the interfacial O atom in Figure 4.8(b) and N atom in Figure 4.8(e) stay identical as those in perfect wurtzite structure, while the  $p_y$  and  $p_z$  orbitals are strongly hybridized with Zn/Ga: 4d orbitals at the valence band edge. As for the rest band immediately below valence band maximum, states of Zn/Ga: 3d, 4p and N/O: 2p orbitals are dominant. The high density of Zn:3d orbital at entire valence

band range and the strong coupling interaction of p-d orbitals at valence band maximum fully agree with the experimental results from X-ray photo-electron spectroscopy[47] and the theoretical investigations obtained by all-electron band structure calculation[48] and LDA+U method[49].

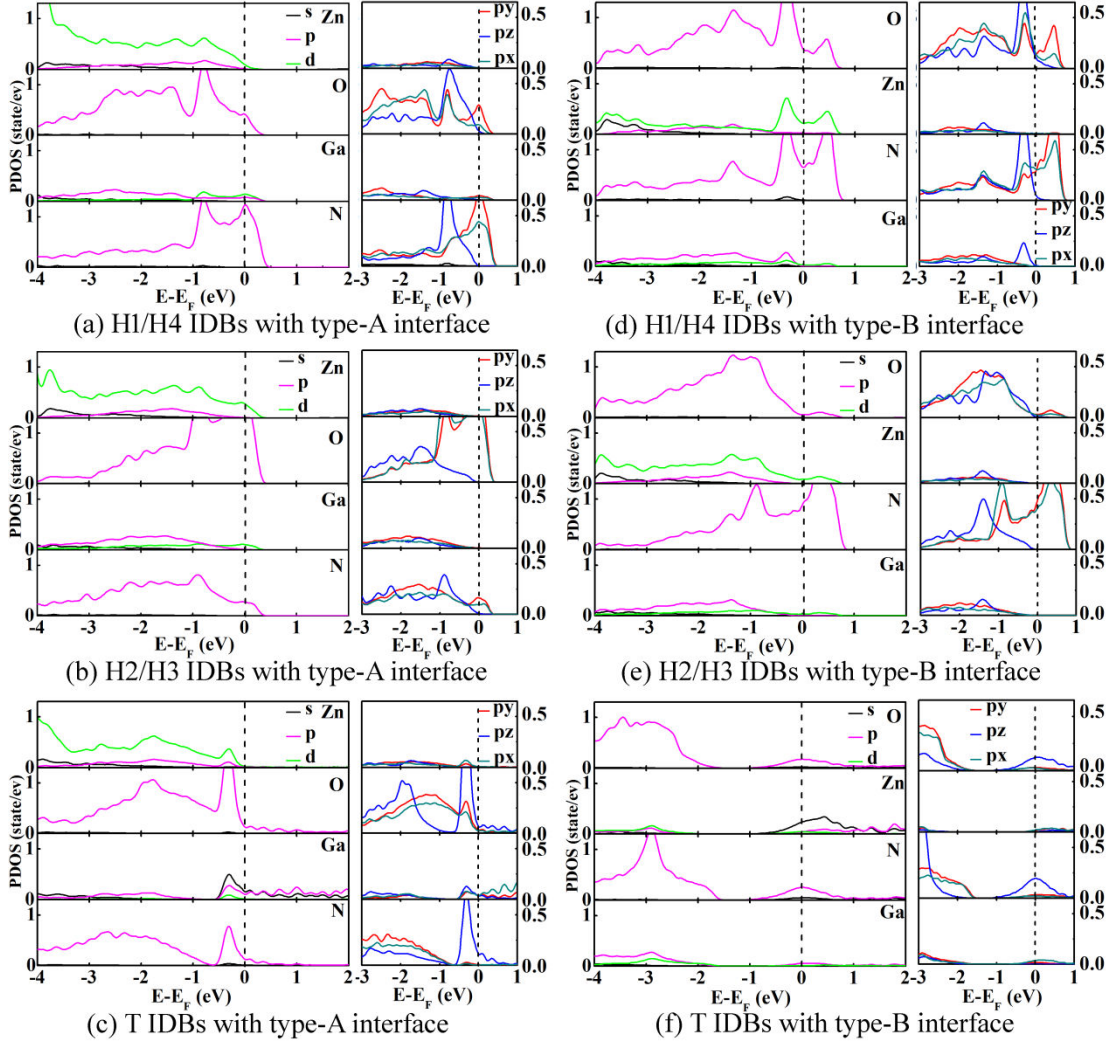


**Figure 4.8.** PDOS of the individual atomic layer (labeled in Figure 4.5 and 4.6) in H and T IDBs with type-A interface (a)-(c), and type-B interface (d)-(f). The atom sequence follows the atomic chain in type-A: Zn-O-Ga-N and type-B: O-Zn-N-Ga. Fermi level is highlighted by the dash line at zero position.

## 4.8 Conclusion

In summary, O-polar ZnO/Ga-polar GaN heterostructure has been achieved using high O/Zn ratio, above the critical value of 1.5, during low temperature P-MBE growth process. Detailed high resolution HAADF and ABF STEM investigation unveiled that the polarity inversion took place within one monolayer, in which the metal atoms are dominant, to form (0001) plane IDB at ZnO/GaN heterointerfaces. Systematical theory simulation of H and T type polarity alignment at ZnO/GaN heterointerface has been performed with the consideration of -Zn-O-Ga-N- and -O-Zn-N-Ga- interfaces. In contrast with the earlier work carried out on polycrystalline ZnO which predicted a H3 IDB, the H4 IDB with -Zn-O-Ga-N- type interface at O-polar ZnO/Ga-polar GaN heterointerface matches the experimental topology very well and comes to be more energetically stable by comparing the relative formation energy. In a detailed analysis of the chemical bonding and charge transfer at those IDBs, it's shown that, independent of atomic sequences, the H IDBs exhibit a 2DHG with one or two interfacial atom layers positively charged. Whereas the T IDBs display a visible electron delocalization with a ELF value of around 0.5 at interfacial Ga/Zn layers, and the layers gained extra 1.0/0.5 e- electron per atom which suggest the formation of 2DEG. PDOS analysis uncovered a metallic nature at the sixteen IDBs as there are non-zero electron states crossing the Fermi level which are mainly originated from Zn/Ga: 3d (H IDBs), 4s (T IDBs) and O/N: 2p orbitals. In this instance, we have unveiled a general property of such interfaces in agreement with a recent report which was based on the analysis of the transport properties in interplay with the polar character of these materials [34]. The desirable property suggests that the fabricated O-polar ZnO/Ga-polar GaN heterostructure could be a promising material for high electron mobility transistors for high frequency, and high power applications in telecommunication.

## References

- [1] Guo, X. L.; Choi, J. H.; Tabata, H.; Kawai, T. Jpn. J. Appl. Phys. 2001, Part 2 40 L177-L180.
- [2] Mitra, A.; Thareja, R. K.; Ganesanc, V.; Guptac, A.; Sahooa, P. K. and Kulkarni, V. N. Appl. Surf. Sci. 2001, 174, 232-239.
- [3] Hoffman, R. L.; Norris, B. J.; Wager, J. F. Appl. Phys. Lett. 2003, 82, 733-735.
- [4] Ohta, H.; Mizoguchi, H.; Narushima, M.; Kamiya, H. T.; and Hosono, H. Appl. Phys. Lett. 2003, 82, 823-825.
- [5] Amano, H.; Kito, M.; Hiramatsu, K. and Akasaki, I. Jpn. J. Appl. Phys. 1989, 28, L2112 - L21148.
- [6] Ozgür, U.; Alivov, Y. I.; Liu, C.; Teke, A.; Reshchikov, M. A.; Dogan, S.; Avrutin, V.; Cho, S. J.; Morkoç, H. J. Appl. Phys. 2005, 98, 041301.
- [7] Tampo, H.; Shibata, H.; Matsubara, K.; Yamada, A.; Fons, P.; Niki, S.; Yamagata, M.; Kanie, H. Appl. Phys. Lett. 2006, 89, 132113.
- [8] Kato, H.; Miyamoto, K.; Sano, M.; Yao, T. Appl. Phys. Lett. 2004, 84, 4562-4564.
- [9] Hong, S. K.; Hanada, T.; Ko, H. J.; Chen, Y.; Yao, T.; Imai, D.; Araki, K.; and Shinohara, M. Appl. Phys. Lett. 2000, 77, 3571-3573.
- [10] Wang, X.; Tomita, Y.; Roh, O. H.; Ohsugi, M.; Che, S. B.; Ishitani, Y.; Yoshikawa, A. Appl. Phys. Lett. 2005, 86, 011921.
- [11] Ruterana, P.; Potin, V.; Barbaray, B.; Nouet, G. Phil. Mag. A 2000, 80, 937-954.
- [12] Zhang, Y.; Lin, N.; Li, Y.; Wang, X.; Wang, H.; Kang, J.; Wilks, R.; Bär, M.; Mu, R. Sci. Rep. 2016, 6, 23106.
- [13] Yan, Y.; Dalpian, G. M.; Al-Jassim, M. M.; Wei, S. H. Phys. Rev. B 2004, 70, 193206.
- [14] Gerthsen, D.; Litvinov, D.; Gruber, T.; Kirchner, C. and Waag, A. Appl. Phys. Lett. 2002, 81, 3972-3974.
- [15] Yan, Y.; Al-Jassim, M. M. Phys. Rev. B 2004, 69, 085204.
- [16] Potin, V.; Ruterana, P.; Nouet, G.; Pond, R.C.; Morkoç, H. Phys. Rev. B 2000, 61, 5587-5599.

- [17] Rhode, S. K.; Horton, M. K.; Kappers, M. J.; Zhang, S.; Humphreys, C. J.; Dusane, R. O.; Sahonta, S. -L.; Moram, M. A. *Phys. Rev. Lett.* 2013, 111, 025502.
- [18] Hsu, J. W.; Manfra, P. M. J.; Lang, D. V.; Richter, S.; Chu, S. N. G.; Sergent, A. M.; Kleiman, R. N.; Pfeiffer, L. N.; Molnar, R. J. *Appl. Phys. Lett.* 2001, 78, 1685-1687.
- [19] Liu, B. D.; Yuan, F.; Dierre, B.; Sekiguchi, T.; Zhang, S.; Xu, Y. K.; Jiang, X. *ACS Appl. Mater. Interfaces* 2014, 6, 14159-14166.
- [20] Northrup, J. E. *Appl. Phys. Lett.* 2005, 86, 071901.
- [21] Potin, V.; Nouet, G.; Ruterana, P. *Appl. Phys. Lett.* 1999, 74, 947-949.
- [22] Northrup, J. E.; Neugebauer, J.; Romano, L. T. *Phys. Rev. Lett.* 1996, 77, 103-106.
- [23] Potin, V.; Nouet, G.; Ruterana, P. *Phil. Mag. A* 1999, 79, 2899-2919.
- [24] Dimitrakopoulos, G. P.; Komninou, P.; Kioseoglou, J.; Kehagias, T.; Sarigiannidou, E.; Georgakilas, A.; Nouet, G.; and Karakostas, T. *Phys. Rev. B* 2001, 64 245325.
- [25] Ko, R. M.; Wang, S. J.; Chen, C. Y.; Wu, C. H.; Lin, Y. R.; Lo, H. M. *Jpn. J. Appl. Phys.* 2016, 56, 04CH03.
- [26] O' Leary, S. K.; Foutz, B. E.; Shur, M. S.; Eastman, L. F. *Solid State Commun.* 2010, 150, 2182-2185.
- [27] Hadi, W. A.; Chowdhury, S.; Shur, M. S.; O'Leary, S. K. *J. Appl. Phys.* 2012, 112, 123722.
- [28] O' Leary, S. K.; Foutz, B. E.; Shur, M. S.; Lester, L. F. *J. Mater. Sci.: Mater. Electron.* 2006, 17, 87-126.
- [29] Kaufmann, U.; Schlotter, P.; Obloh, H.; Köhler, K. and Maier, M. *Phys. Rev. B* 2000, 62, 10867-10872.
- [30] Alivov, Y. I.; Van Nostrand, J. E.; Look, D. C.; Chukichev, M. V.; Ataev, B. M. *Appl. Phys. Lett.* 2003, 83, 2943-2945.
- [31] Zhang, X. M.; Lu, M. Y.; Zhang, Y.; Chen, L. J.; Wang, Z. L. *Adv. Mater.* 2009, 21, 2767-2770.
- [32] Rogers, D. J.; Teherani, F. H.; Yasan, A.; Minder, K.; Kung, P.; Razeghi, M. *Appl. Phys. Lett.* 2006, 88, 141918.

- [33] Yang, Q.; Wang, W.; Xu, S.; Wang, Z. L. *Nano Lett.* 2011, 11, 4012-4017.
- [34] Schuster, F.; Laumer, B.; Zamani, R. R.; Magen, C.; Morante, J. R.; Arbiol, J. and Stutzmann, M. *ACS Nano* 2014, 8, 4376-4384.
- [35] Liu, B. D.; Yang, W. J.; Li, J.; Zhang, X. L.; Niu, P. J.; Jiang, X. *Nano Lett.* 2017, 17, 3195-3201.
- [36] Hong, S. K.; Hanada, T.; Ko, H. J.; Chen, Y. and Yao, T. *Phys. Rev. B* 2002, 65, 115331.
- [37] Kobayashi, A.; Kawaguchi, Y.; Ohta, J.; Fujioka, H. *Appl. Phys. Lett.* 2006, 88, 181907.
- [38] Ullah, M. B.; Avrutin, V.; Li, S. Q.; Das, S.; Monavarian, M.; Toporkov, M.; Özgür, Ü.; Ruterana, P. and Morkoç, H. *Phys. Status Solidi RRL*. 2016, 10, 682-686.
- [39] Austerman, S. B. and Gehman, W. G. *Mater. Sci.* 1966, 1, 249-260.
- [40] Kim, J. C. and Goo, E. J. *Am. Ceram. Soc.* 1990, 73, 877-884.
- [41] Wang, Y.; Salzberger, U.; Sigle, W.; Suyolcu, Y. E. and van Aken, P. A. *Ultramicroscopy* 2016, 168, 46-52.
- [42] Kresse, G. and Joubert, J. *Phys. Rev. B* 1996, 54, 11169-11186.
- [43] Hafner, J. J. *Comput. Chem.* 2008, 29, 2044-2078.
- [44] Kresse, G. and Joubert, J. *Phys. Rev. B* 1999, 59, 1758-1775.
- [45] Li, S. Q.; Lei, H. P.; Wang, Z.; Chen, J.; Ruterana, P. *Phys. Status Solidi B* 2018, 255, 1700429.
- [46] Savin, A.; Jepsen, O.; Flad, J.; Andersen, O. K.; Preuss, H.; Von Schnering, H. G. *Angewandte Chemie-International Edition in English* 1992, 31, 187-188.
- [47] Kowalczyk, S. P.; Ley, L.; Pollak, R.A.; McFeely, F.R.; Kowalczyk, S.P. and Shirley, D. A. *Phys. Rev. B* 1974, 9, 381-391.
- [48] Wei, S. -H.; and Zunger, A. *Phys. Rev. B* 1988, 37, 8958-8981.
- [49] Janotti, A.; Segev, D. and Van de Walle, C.G. *Phys. Rev. B* 2006, 74, 045202.

## Chapter 5

### **[0001] Tilt Grain Boundaries in ZnO Semiconductor**

#### 5.1 Introduction

An important role is played by polycrystalline materials of technological importance where the performances of the corresponding devices are governed by the atomic structures of grain boundary (GB) [1]. The corresponding research has led to the development of the structural unit model which describes the GB atomic structure versus the macroscopic degrees of freedom (tilt, rotation, interface, ...) [2-4]. In this formalism, a GB can be built using only a few fundamental bricks: “the structural units”. For instance, the atomic structure of several [110] tilt boundaries in Al was reported to be systematically described by the combination of a limited number of units [4].

During the last years, many attempts have been made in order to extend this concept to the GBs investigation of lower symmetry systems like wurtzite structure. Especially along with the development of light-emitting devices, GaN and ZnO semiconductor with a wide bang gap attract a great attention due to their excellent performance in luminescence properties. The electrically activated states which may be induced by the GB itself as well as the interactions between GB and the native defects, such as intrinsic point defects [5,6], isolated dislocations [7-9], stacking faults [9-12] and IDBs [13,14], is a strong motivation for their investigation.

It has been reported that the atomic structure of the high angle ( $>15^\circ$ ) GBs is made of bulk dislocation-like structural units [15,16]. As was shown in GaN, through analysis by high-resolution TEM and multiscale atomic modelling, three configurations of pure a edge threading dislocation are considered to be the structural units of [0001] tilt GBs: 4-, 57- and 8-atom rings [5-7, 17-19]. They form upon growth of GaN on the six or

three fold symmetry surfaces of highly mismatched sapphire [20-22], silicon carbide [23], or silicon [13]. In the same way, Oba et al. [15] have investigated ZnO bi- and polycrystalline films, the  $\Sigma 7$  boundary atomic structure exhibited an array of bulk dislocation-like units which is in agreement with the models proposed for GaN [16,24].

In the coincidence site lattice (CSL) formalism, [0001] tilt GBs are defined by two angles:  $\theta$  and  $60^\circ - \theta$  among the 12 equivalent descriptions [16,25]. In these grain boundaries, the  $\Sigma 13$  GB at  $27.8^\circ/32.2^\circ$  seems to have been the most investigated in layers grown on sapphire [26]. Moreover, a structural transition from straight structure unit alignment to zigzag alignment generally appear at the tilt angle of around  $30^\circ$  [15,27-29]. However, the dislocation core structure of this GB is still not well understood. From their high-resolution TEM and topological theory analysis, Kiselev et al. showed that this boundary could be extensively faceted and form at an average angle of around  $31.5^\circ$  in ZnO bicrystals [30]. In their theoretical investigation in ZnO, Carlsson et al.[31] reported that the  $\Sigma 13$  ( $32.2^\circ$ ) boundary defect free atomic structure exhibited a minimum energy configuration made of a zigzag open core of 5/7 atom cycles exhibiting dangling bonds. In our theoretical investigation of [0001] tilt boundaries in wurtzite GaN, it was shown that this boundary exhibits a minimum energy configuration with two types of 5/7 atom-rings structural units ( $57/57^-$  and  $57^+57^-$  atom rings) [16].

In the following, we report on the [0001] tilt GB in wurtzite ZnO in a close combination of detailed experimental and theoretical investigation. Focusing on tilt angles around  $30^\circ$ , we demonstrate that the structural unit concept is also valid in wurtzite materials, and the specific units for GaN and ZnO are unveiled. To begin with, we propose that the topological description of the GB (boundary angle and plane, and dislocation content for the boundary period) should be the starting point for a better characterization or theoretical modelling. Consequently, the influences of those dislocation contents related to the electronic properties are investigated in terms of total density of states (DOS). The aim of this work is to fully understand the behaviour of GB in polycrystal



materials, GaN and ZnO, as well as the role of dislocation contents in the properties of materials for further technological applications.

## 5.2 Topological Analysis of GBs in Wurtzite Symmetry

Pond and coworkers [32-35] have developed an elegant device called the “topological theory” for the description of the grain boundary. They have proposed the use of dichromatic complexes to lay out the two crystals related by their respective orientation: as represented in white ( $\lambda$ ) and black ( $\mu$ ) [32]. This allows to visually obtain, for special misorientations ( $\Sigma$ ), the three-dimensional coincident site lattices (CSL). In case of the wurtzite structure and rotation around the [0001] axis, the CSL’s resulting from rotations  $\theta$  and  $60^\circ - \theta$  are identical except for a  $c/2$  translation [33]. The sides and diagonals of these CSLs constitute the densest atomic planes which can be shared by the two crystals located on each side of a GB. Therefore, like new basic unit supercells, they will tend to constitute the limiting planes for the grains as the most stable and lowest energy GBs [16,24]. In Pond’s device, the GB which is thus a particular planar defect is completely defined by the indices of the interface plan (for instance a side or diagonal of the CSL) and the corresponding unit vector which connect the two end coincident sites. Along this direction, the common sites are connected by a crystallographic defect known as a primary grain boundary defect which in most cases corresponds to one or more dislocations of the parent crystal [35] whose strain field overlap and release the misorientation between the adjacent crystals. The determination of the defect content follows the conventional Burgers circuit which runs in the two adjacent crystals, crossing the interface at coincident sites defining one period of the GB. Subsequently, the constructed circuit is mapped in one of the crystals and the obtained closure failure corresponds to the corresponding defect content which uniquely characterizes the particular boundary [35]. The typical case of  $\Sigma 7$  is illustrated in Figure 5.1. Considering first the side of the CSL  $\{1/3[\bar{1}, 5, \bar{4}, 0]/(\bar{3}, 1, 2, 0)\}$  at the rotation angle of  $\theta = 21.79^\circ$  in Figure 5.1(a), the number and type of the GB dislocations can be identified by taking circuit SXF ( $C_\mu = a_3 - 2a_2$ ,  $C_\lambda = -2a_3 + a_2$ ), which

encloses one period in the boundary plane (Figure 5.1(a)), is mapped in the  $\lambda$  crystal as the reference crystal. In this instance, the defect content inside one period of the boundary corresponds to  $FS = -a_{1\lambda}$ .

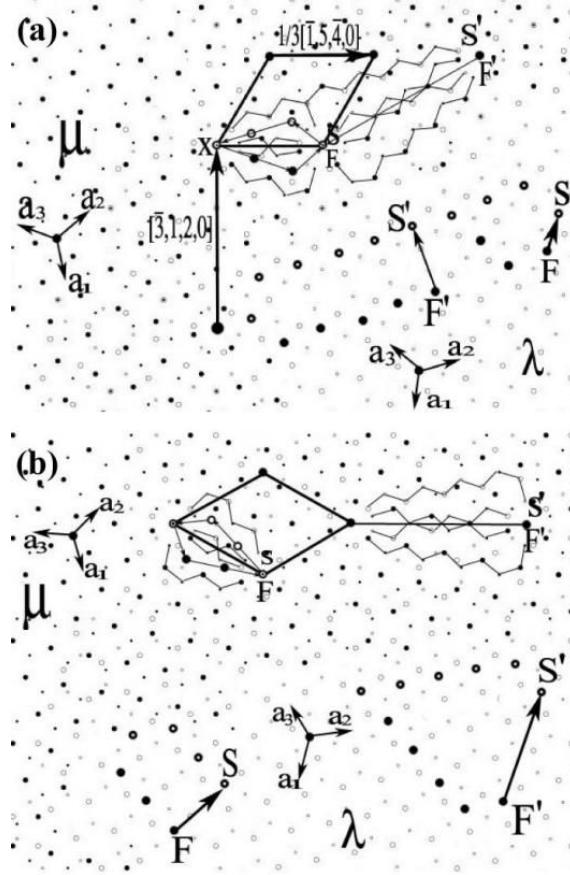


**Figure 5.1** The  $\Sigma 7$  GB dichromatic complex and Burgers circuit, the unit cell is underlined, for mapping the circuit, the  $\mu$  (black) crystal sites have been removed, the defect content is shown as the vector connecting the final and starting sites for the side (FS) and diagonal (F'S'): (a)  $\theta = 21.79^\circ$ ; (b)  $\theta = 38.21^\circ$

When a similar circuit is drawn around the diagonal of the CSL  $\{ 1/3[2, \bar{3}, 1, 0] / (\bar{4}, \bar{1}, 5, 0) \}$ , the obtained defect content comes out as  $F'S' = (a_3 - a_1)_\lambda$ , which corresponds to a  $[10\bar{1}0]$  dislocation content. Similarly, for the  $\Sigma 7$  at  $\theta = 38.21^\circ$  (Figure 5.1(b)), a  $[10\bar{1}0]$  edge dislocation content of  $(a_2 - a_1)_\lambda$  and  $-3a_{1\lambda}$  are obtained along the side  $\{ 1/3[1, 4, \bar{5}, 0] / (\bar{3}, 2, 1, 0) \}$  and the diagonal  $\{ 1/3[\bar{1}, 3, \bar{2}, 0] / (\bar{5}, 1, 4, 0) \}$  of CSL, respectively.

A similar analysis is shown in Figure 5.2 for  $\Sigma 13$  GB. As can be seen, at  $27.2^\circ$ , the defect content along the side  $\{1/3[2,5,\bar{7},0]/(\bar{4},3,1,0)\}$  is still  $(a_2 - a_1)_\lambda$ , and along the diagonal  $\{1/3[\bar{2},4,\bar{3},0]/(\bar{7},2,5,0)\}$ , it also  $-3a_{1\lambda}$ . Things change at  $32.2^\circ$ , as for the side  $\{1/3[\bar{2},7,5,0]/(\bar{4},1,3,0)\}$ , we have  $-2a_1$ , and along the diagonal  $\{[\bar{3},4,\bar{1},0]/(\bar{5},\bar{2},7,0)\}$ :  $2(a_3 - a_1)_\lambda$  which are larger vectors.

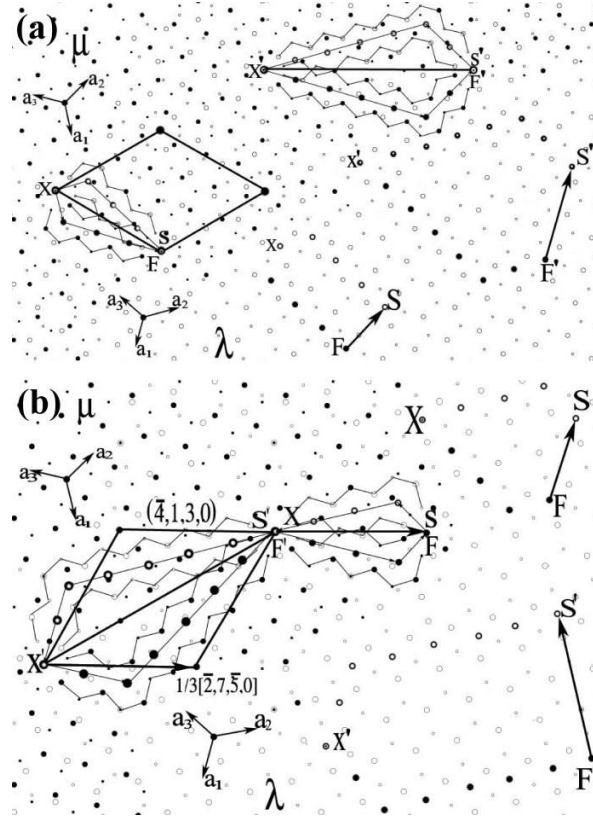


**Figure 5.2.** The  $\Sigma 13$  grain boundary (a)  $\theta=27.8^\circ$ ; (b)  $\theta=32.2^\circ$

This was systematically determined for the main CSLs which can be generated in the wurtzite crystal through rotations around the  $[0001]$  axis up to  $60^\circ$ . As can be seen in Table 5.1 the dislocation content for all the boundaries is made of  $1/3[\bar{2},1,1,0]$  and  $[1,0,\bar{1},0]$  dislocation whose number increases mainly with the length of the period of the corresponding CSL. We may have up to  $-9a_1$  along the diagonal  $\{[\bar{1}\bar{3},2,11,0]/(3,\bar{8},5,0)\}$  of  $\Sigma 49$  at  $43.57^\circ$  and  $4[\bar{1},0,1,0]$  for the diagonal  $\{[5,\bar{6},1,0]/(\bar{7},\bar{4},11,0)\}$  of  $\Sigma 31$  at  $42.1^\circ$ .

**Table 5.1** Burgers vectors of interface dislocations of the main  $[0001]$ .tilt GBs in wurtzite.

GB Parameters				Primary dislocation content	
	Tilt (°)	Boundary Plan	Period	Vector	Length
19	13.7	$(\bar{5}, 2, 3, 0)$	$1/3 [\bar{7}, \bar{1}, 8, 0]$	$-\mathbf{a}_1$	$1/3 [\bar{2}, 1, 1, 0]$
		$(\bar{7}, \bar{1}, 8, 0)$	$[\bar{3}, 5, \bar{2}, 0]$	$\mathbf{a}_1 - \mathbf{a}_3$	$[1, 0, \bar{1}, 0]$
	46.83	$(\bar{5}, 3, 2, 0)$	$1/3 [1, 7, \bar{8}, 0]$	$2(\mathbf{a}_2 - \mathbf{a}_1)$	$2[\bar{1}, 1, 0, 0]$
		$(\bar{8}, 1, 7, 0)$	$[3, \bar{5}, 2, 0]$	$-6\mathbf{a}_1$	$2 [\bar{2}, 1, 1, 0]$
49	16.43	$(\bar{8}, 3, 5, 0)$	$1/3 [\bar{2}, 13, \bar{11}, 0]$	$-2\mathbf{a}_1$	$2/3 [\bar{2}, 1, 1, 0]$
		$(\bar{11}, \bar{2}, 13, 0)$	$[5, \bar{8}, 3, 0]$	$2(\mathbf{a}_3 - \mathbf{a}_1)$	$2[\bar{1}, 0, 1, 0]$
	43.57	$(\bar{8}, 5, 3, 0)$	$1/3 [2, 11, \bar{13}, 0]$	$3(\mathbf{a}_2 - \mathbf{a}_1)$	$3[\bar{1}, 1, 0, 0]$
		$(\bar{13}, 2, 11, 0)$	$[3, \bar{8}, 5, 0]$	$-9\mathbf{a}_1$	$3 [\bar{2}, 1, 1, 0]$
31	17.90	$(\bar{6}, 5, 1, 0)$	$1/3 [4, 7, \bar{11}, 0]$	$\mathbf{a}_1 - \mathbf{a}_2$	$[1, \bar{1}, 0, 0]$
		$(\bar{11}, 4, 7, 0)$	$[\bar{1}, 6, \bar{5}, 0]$	$-3\mathbf{a}_1$	$[\bar{2}, 1, 1, 0]$
	42.10	$(\bar{6}, 1, 5, 0)$	$1/3 [\bar{4}, 11, \bar{7}, 0]$	$-4\mathbf{a}_1$	$4/3 [\bar{2}, 1, 1, 0]$
		$(\bar{7}, \bar{4}, 11, 0)$	$[5, \bar{6}, 1, 0]$	$4(\mathbf{a}_3 - \mathbf{a}_1)$	$4[\bar{1}, 0, 1, 0]$
7	21.79	$(\bar{3}, 1, 2, 0)$	$1/3 [\bar{1}, 5, \bar{4}, 0]$	$-\mathbf{a}_1$	$1/3 [\bar{2}, 1, 1, 0]$
		$(\bar{4}, \bar{1}, 5, 0)$	$[2, \bar{3}, 1, 0]$	$\mathbf{a}_3 - \mathbf{a}_1$	$[\bar{1}, 0, 1, 0]$
	38.21	$(\bar{3}, 2, 1, 0)$	$1/3 [1, 4, \bar{5}, 0]$	$\mathbf{a}_2 - \mathbf{a}_1$	$[\bar{1}, 1, 0, 0]$
		$(\bar{5}, 1, 4, 0)$	$[\bar{1}, 3, \bar{2}, 0]$	$-3\mathbf{a}_1$	$[\bar{2}, 1, 1, 0]$
13	27.80	$(\bar{4}, 3, 1, 0)$	$1/3 [2, 5, \bar{7}, 0]$	$\mathbf{a}_2 - \mathbf{a}_1$	$[\bar{1}, 1, 0, 0]$
		$(\bar{7}, 2, 5, 0)$	$[\bar{1}, 4, \bar{3}, 0]$	$-3\mathbf{a}_1$	$[\bar{2}, 1, 1, 0]$
	32.2	$(\bar{4}, 1, 3, 0)$	$1/3 [\bar{2}, 7, \bar{5}, 0]$	$-2\mathbf{a}_1$	$2/3 [\bar{2}, 1, 1, 0]$
		$(\bar{5}, \bar{2}, 7, 0)$	$[\bar{3}, 4, \bar{1}, 0]$	$2(\mathbf{a}_3 - \mathbf{a}_1)$	$2[\bar{1}, 0, 1, 0]$

## 5.3 Methodology

Subsequent to the work of Hornstra [36] in the diamond structure, Osipyan and Smirnova [37] reported a detailed geometrical investigation of the perfect dislocations that could form in the wurtzite lattice. Apart from the straightforward four dislocations which possess the simplest translations of  $1/3\langle 11\bar{2}0 \rangle$  and  $\langle 0001 \rangle$  as the Burgers vectors, the authors suggested that additional 9 different dislocations may exist. Two of the set exhibit a Burgers vector of  $\langle 1\bar{1}00 \rangle$  type and a glide plane of  $\{11\bar{2}0\}$  which can be identified as  $[10\bar{1}0]$  dislocations: the first is of pure edge type with its dislocation line along  $\langle 0001 \rangle$  direction, whereas the second one is a mixed dislocation with the dislocation line lies along  $\langle \bar{1}101 \rangle$ . Of particular interest is the edge type that may form as threading dislocation during the growth of layers along the conventional  $[0001]$  for GaN and ZnO. Indeed, it may then be suspected to be one of the structural unit for  $[0001]$  tilt GBs [18]. The GBs constructed by **a**-edge dislocation have already been studied both in GaN and ZnO. In GaN, it was shown that the periodic interfaces such as symmetric  $\Sigma 19$ ,  $\Sigma 7$  and  $\Sigma 13$  [5] can be explained in terms of a mixture of the three basic structure units of  $1/3[11\bar{2}0]$  dislocation [15,26,38]. A straight 57/57-atom ring core structure based  $\Sigma 13$  GB plane was also reported in ZnO [26].

Therefore, the interesting question is to determine the atomic structure which can take the topologically expected  $[10\bar{1}0]$  for the wurtzite crystals. To this end, we have carried out an extensive investigation in GaN and ZnO GBs, and in the following, we discuss the corresponding results for the atomic structure of the edge dislocations in GaN and ZnO using HTEM and theoretical modelling.

### 5.3.1 Experimental Procedures

The  $90^\circ$  misoriented growth domains have been observed in ZnO layers deposited on (0001) sapphire between  $550^\circ\text{C}$  and  $650^\circ\text{C}$  using magnetron sputtering. A radio frequency (RF) power of 150 W was used for ZnO deposition. Before the actual

deposition, ZnO targets experienced a pre-sputter step for 5 minutes to remove contamination from the surface. The as-deposited film was annealed at 850 °C for 1 hour in an ambient atmosphere which is designed to improve the crystalline quality. In addition, [0001] tilt boundaries have been observed in molecular beam epitaxy GaN layers.

The transmission electron microscopy (TEM) plan-view specimens were mechanically polished down to 100  $\mu\text{m}$  and then dimpled to 10  $\mu\text{m}$  from back surface. The electron transparency was finally obtained by ion-milling with the sample holder maintained at liquid nitrogen temperature in order to minimize the ion beam damage. The experimental observations were carried out in a 002B Topcon HRTEM operated at 200 kV with a point to point resolution of 1.8 Å. The image simulation based on multislice method were carried using electron microscopy software [39,40].

### 5.3.2 Computational Details

The atomistic simulation methodology was performed in two steps; first within molecular dynamics based on the modified Stillinger-Weber (SW) empirical potential [41,42] and second using first principle calculation. The modified SW empirical potential takes only into account the two- and three-body short-range interactions and the molecular dynamics can handle very large systems (100000 atoms) within reasonable computing times. As the treatment of semiconductor compounds raises the problem of wrong bonds, which form in crystallographic defects, the parameters for Zn-O were optimized by fitting the structural parameters and the elastic constants to the experimental results. For the Zn-Zn and O-O parameters, we fitted the total-energy calculation of inversion domain boundaries (IDBs: Holt IDB and IDB\*) which contain wrong bonds to the ab-initio calculation results of Yanfa et al. [43]. In our case, the Holt IDB is energetic unstable and transforms to IDB\* with an energy of 0.4 eV and the calculated Zn-O bond length across the boundary is 1.87 Å instead of 1.97 Å in the bulk, which is in agreement with the first principle calculations [43]. GBs are

constructed by taking into account the three-dimensional periodic boundary conditions. For a given interface all possible distinct initial crystallographic configurations have been considered and the corresponding  $\gamma$  surface has been analyzed to obtain the structure of lowest energy [38].

The first principle calculations were carried out in a next step using the SIESTA package [44] with a self-interaction correction (SIC) scheme for LDA as exchange correlation as parametrized by Perdew and Zunger [45] and the standard norm-conserving pseudopotentials for Zn and O are used for the core-valence electron interactions. The energy cutoff was set to 250 Ry and the k-point in Brillouin zone was sampled in 4×4×4 Monkhorst-Pack scheme.

We followed the definition of formation energy for boundary in periodic boundary conditions proposed by Northrup et al [46] as:

$$\sigma_{wall} = \frac{1/2 (E - E_{bulk})}{A}$$

where  $1/2 (E - E_{bulk})$  is the formation energy of a single boundary by subtracting the total energy ( $E_{bulk}$ ) of a bulk structure with an equivalent atom number from the total energy ( $E$ ) of the supercell containing two boundaries. The factor of  $A$  is the area of the periodic unit cell of the tilt boundary.

The three basic structure units of GB (4-, 8-, 5/7-atom rings) are obtained on the basis of the dichromatic complex approach as described in our previous studies of grain boundaries in GaN [11,16,38]. The topological structures can be seen in Ref. 19. In the simplest case,  $\Sigma 7$  GB based on the each of three basic structure units could be taken as example to explain the different behavior of ZnO and GaN. Table 5.2 shows the calculated formation energies of the  $\Sigma 7$  ZnO GB which are made of these 3 basic structural units using SW parameters and SIESTA calculation. The energies with SW(O) are calculated in open-core condition without considering wrong bonds in models. The Zn-Zn wrong bonds are counted in the condition of SW(C). It points out

that, the energies are sensitive to the conditions used for calculation and the 5/7 configuration always appears to have a higher energy in all the calculations. The formation energy trend obtained here is at variance from the case of GaN [16] which always shows the lowest energy in 57-atom rings structure, but agrees with the relative stability of ZnO GB calculated by J. Y. Roh et al [27]. This may be explained by the energetically unfavorable Zn-Zn and O-O wrong bonds formed at 5/7-atom rings which may theoretically not be expected in this more ionic material.

**Table 5.2.** *The formation energies of the  $\Sigma 7$  grain tilt boundary at  $21.79^\circ$  for the 3 basic structural unit structures of the  $1/3[11\bar{2}0]$  GB dislocation in ZnO compound. The energies are given in mJ/m<sup>2</sup>.*

	SW (O)	SW(C)	SIESTA
4	1174	1174	1078
8	1071	1347	999
5/7	1616	1447	1276

#### 5.4. The Atomic Structure of the $[10\bar{1}0]$ Edge Dislocation

As shown by the topological analysis, all the tilt grain boundaries around  $[0001]$  should exhibit the  $\langle 10\bar{1}0 \rangle$  edge dislocation in the wurtzite structure. In their theoretical report on the wurtzite dislocations, Osipyan and Smirnova have classified this dislocation in the category of other dislocation and jogs and proposed a large and open atomic structure [37]. However, during our detailed investigations of grain boundaries GaN we have not been able to observe a distinct structural unit for this dislocation. In the following we report the topological analysis carried out on an asymmetric  $\Sigma 7$  GB in GaN which brought about the evidence of such a dislocation.



### 5.4.1. The $[10\bar{1}0]$ Edge Dislocation in GaN

In our samples, the observed asymmetric GB is exhibited in Figure 5.3. where 4 periods have been marked. In each of them, the three basic dislocation cores have been identified. Periods 1 and 2 are aligned; period 3 is a step which makes period 4 to shift upward. Therefore, this area contains an additional feature of GBs: an interfacial step which also can be characterized using the topological theory [5]. As can also be seen, this interface is only made of a mixture of the three atom cycles of the  $1/3[11\bar{2}0]$  edge dislocation (57-, 4-, 8-). As the period has three dislocations, one would compared it to the  $\Sigma 7 \theta=38.21^\circ \{[\bar{1}, 3, \bar{2}, 0]/(\bar{5}, 1, 4, 0)\}$  boundary, but looking at the lower part of the boundary, it is seen clearly that a  $\{10\bar{1}0\}$  is parallel to the boundary. So referring to the basal vectors on each side of the boundary, we clearly have a  $\Sigma 7 \theta=38.21^\circ$ , but the GB plane is asymmetric and has indices in the  $\lambda$  and  $\mu$  crystals as  $(\bar{3}8\bar{5}0)_\lambda/(0\bar{1}10)_\mu$ .

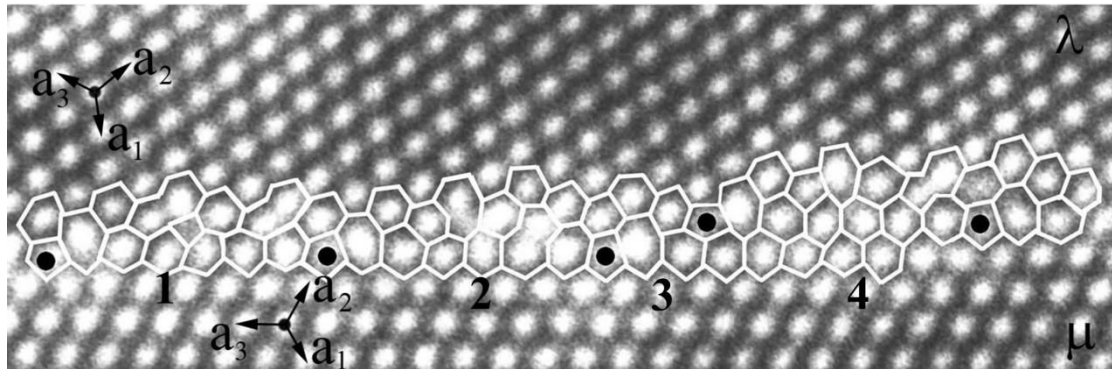


**Figure 5.3.** a  $\Sigma 7 \theta=38.21^\circ$  asymmetric GB exhibiting 4 periods made of 4-, 57- and 8- atom cycles of the  $1/3\langle 11\bar{2}0 \rangle$  edge dislocation, as well as a step.

The defect content of the period of this boundary has been determined for period 4. To this end a Burger circuit can be seen in Figure 5.4a, as marked by full black circles where the start (S) and final (F) points coincide at a coincidence site of the two grains in the boundary. The Burgers vectors as can be seen after mapping the same circuit inside the  $\lambda$  crystal (open circles) corresponds to FS vector as:  $-2\mathbf{a}_1 + \mathbf{a}_2$ . This vector is not parallel to any of the basal vectors  $\mathbf{a}_1$ ,  $\mathbf{a}_2$ ,  $\mathbf{a}_3$  and can be decomposed in two vectors:

$-\mathbf{a}_1 + (\mathbf{a}_2 - \mathbf{a}_1)$  as shown in Figure 5.4b. Finally as  $(\mathbf{a}_2 - \mathbf{a}_1)$  corresponds exactly to  $[\bar{1}100]$ , the defect content of this asymmetric  $\Sigma 7$  GB is:  $-\mathbf{a}_1 + [\bar{1}100]$ . Therefore, in GaN, the core structure of the  $\langle 10\bar{1}0 \rangle$  edge dislocation is simply formed by a combination of the  $1/3\langle 11\bar{2}0 \rangle$  atom cycles as can be seen in Figure 5.4c in case of the 57- rings.

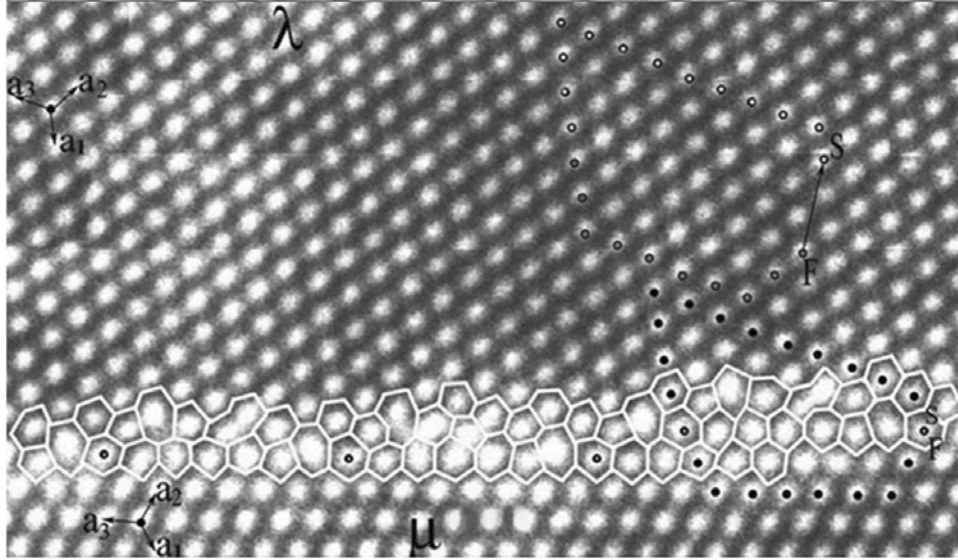


**Figure 5.4a.** Burgers circuit around period 4 and mapping in  $\lambda$  crystal

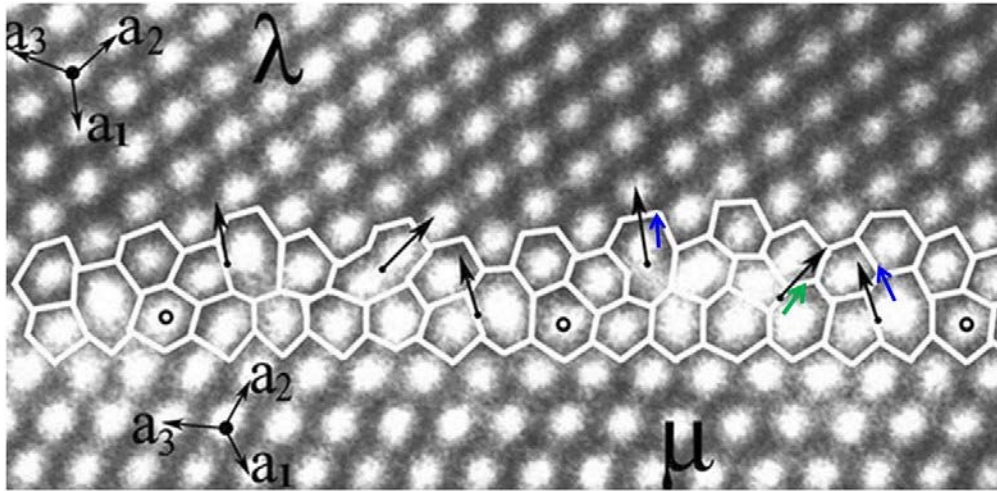


**Figure 5.4b.** Inside the boundary, the dislocations are mainly grouped and their Burgers vectors appear to rotate (arrows).

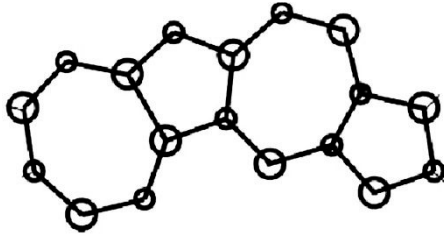


**Figure 5.4c.** Example of a possible core structure for the  $\langle 10\bar{1}0 \rangle$  edge dislocation in GaN.

#### 5.4.2 The $[10\bar{1}0]$ Edge Dislocation in ZnO

Before moving to the atomic structure of the  $[10\bar{1}0]$  dislocation, as shown in Figure 5.5 we have a typical growth with adjacent grains of ZnO rotated by  $30^\circ$  so that the  $[11\bar{2}0]$  and  $[10\bar{1}0]$  zone axis are directly visualized in the same area. It is necessary to sum up the results on this type of investigation in ZnO GBs for the **a** type dislocation. In plane-view, the overall diffraction showed systematically the formation of  $30^\circ$  rotation grains, as can be seen in Figure 5.6.

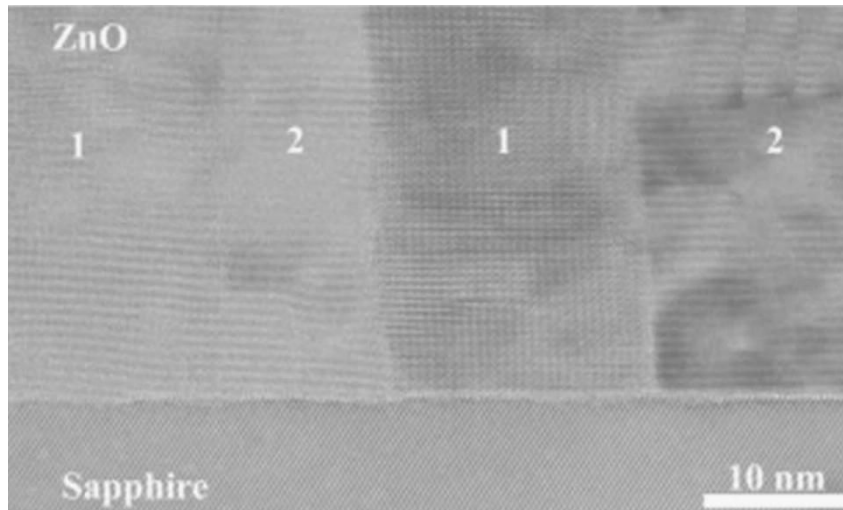


**Figure 5.5a.** Columnar growth of ZnO on (0001) sapphire with column (1) along a  $[11\bar{2}0]$  zone axis and (2) along  $[10\bar{1}0]$ .

However during all the subsequent analysis in high resolution TEM, we only observed  $\Sigma 13$  GBs for  $\theta = 32.2$  or  $27.8^\circ$ . This is an obvious proof of tendency of the materials to minimize the formation energy also during the growth. Indeed, the possible existence

of the  $\Sigma 97$  with a rotation angle of  $29.41^\circ$  would have needed the formation of some  $5a$  dislocation inside period, which would have costed much more energy [16]. In this instance, we also could demonstrate the validity of the CSL concept for the wurtzite symmetry, by accurately obtaining the core structures and number of dislocations inside the side and diagonal planes.

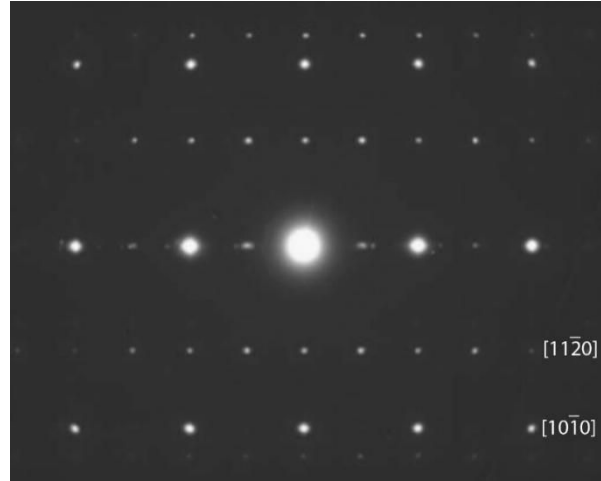


**Figure 5.5b.** The diffraction pattern of ZnO in columnar growth, the spots corresponding to the  $[11\bar{2}0]$  and  $[10\bar{1}0]$  zone axis are shown.

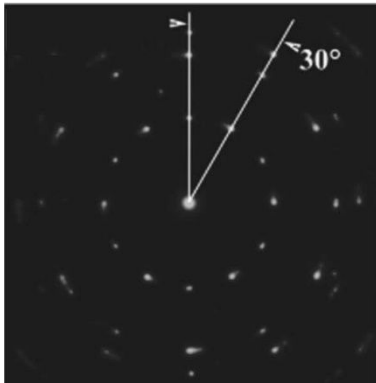


**Figure 5.6.** Diffraction pattern recorded along the  $[0001]$  zone axis of ZnO/sapphire columnar grains.

Starting by  $\theta = 32.2^\circ$ , along the sides of CSL  $\{1/3[\bar{2}, 7, \bar{5}, 0]/(\bar{4}, 1, 3, 0)\}$  where one expects a Burgers vector content of  $-2a_1$ , the atomic structure that we determined was at variance with the one that had been discussed in the literature for many times which had been mistakenly taken for  $2a$ , although that configuration exhibited clearly a  $[10\bar{1}0]$  Burgers content [47].

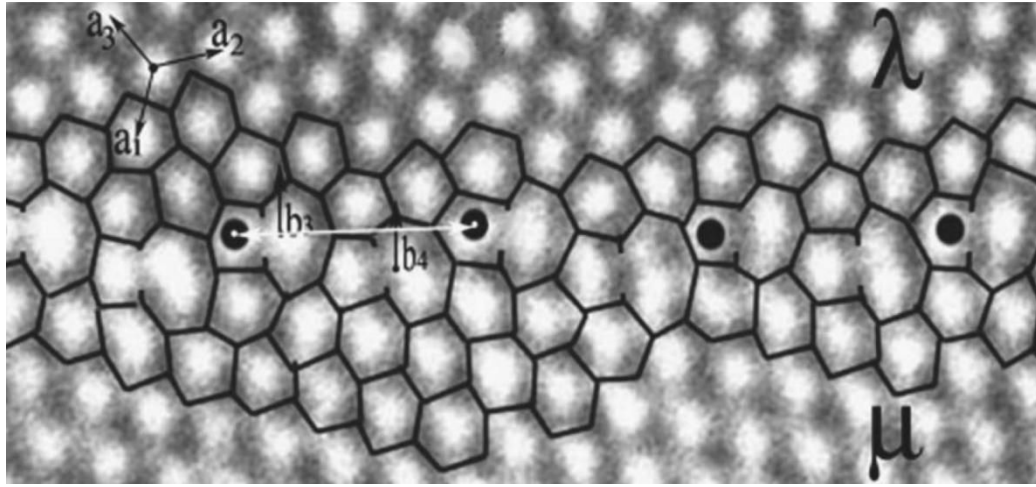


**Figure 5.7.** Atomic structure of  $\Sigma 13$  GB, CSL side at  $32.2^\circ$   $b_1$  and  $b_2$  are parallel and the period (black dots) contains two dislocations.

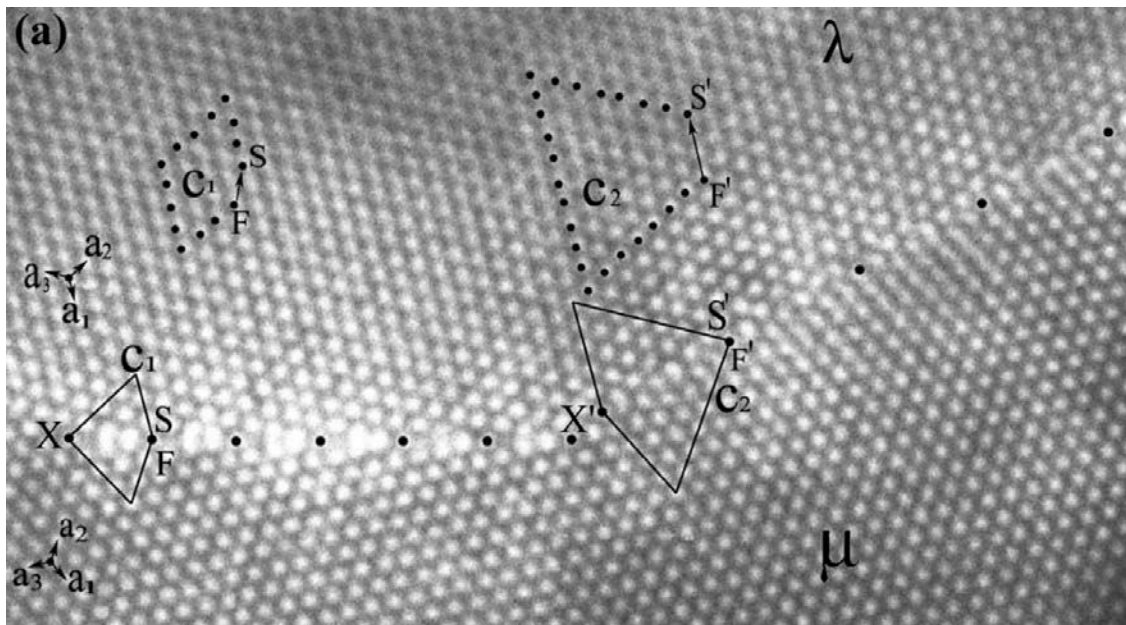


**Figure 5.8a.** HRTEM image of a  $\Sigma 13$  GB for the rotation angle of  $27.8^\circ$  with boundary planes lied on the side and diagonal of CSL.

In order to keep the overall average rotation angle as shown in the diffraction pattern above, this work shows that the GBs are systematically made of the side and diagonals and the rotation angle goes randomly from  $27.8^\circ$  to  $32.2^\circ$  between adjacent grains. In this instance, the topological analysis which identifies the defect content and the combination with HRTEM become an important tool for the determination of the right

grain boundary characteristics. In the HRTEM micrographs of the grain boundary, as shown in Figure 5.8a, the symmetric boundaries indices are first determined along with the corresponding periods. Subsequently the defect contents are determined by mapping each circuit in the  $\lambda$  crystal. As can be seen, the corresponding Burgers vectors are  $\mathbf{a}_2 - \mathbf{a}_1$  (side of the CSL) inside the  $(\bar{4}, 3, 1, 0)$  boundary plane, and  $-3\mathbf{a}_1$  (diagonal of the CSL) in the  $(\bar{7}, 5, 2, 0)$ , respectively. Now referring to the CSL diagram in Figure 5.8b, this is exactly to a  $\Sigma 13$  boundary with a rotation angle of  $27.8^\circ$  around  $[0001]$  axis.

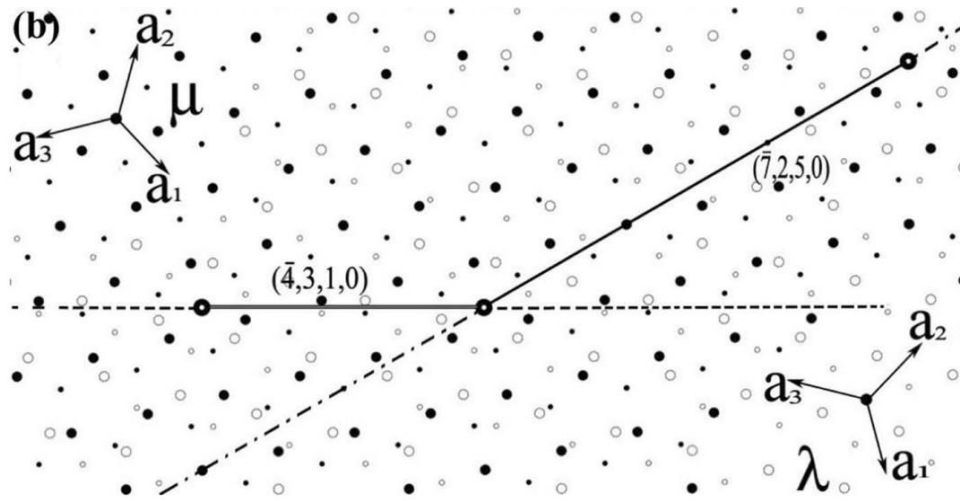


**Figure 5.8b.** The topological layout of a  $\Sigma 13$  GB with rotation angle of  $27.8^\circ$  showing the side and diagonal planes. Black and white crystal represent the crystal  $\mu$  and  $\lambda$ .

As seen in Figure 5.8a, we have thus a Burgers vector content of  $\mathbf{a}_2 - \mathbf{a}_1$  which then corresponds to  $1/3[\bar{1}2\bar{1}0] - 1/3[2\bar{1}\bar{1}0] = [\bar{1}100]$  and indeed the corresponding core structure is, as can be seen, completely different to that of a simple combination of  $\mathbf{a}$  dislocations (seen above for GaN). The same procedure has been used to systematically characterize the boundaries in the same sample, and as seen in Figure 5.9a, we have a new configuration.



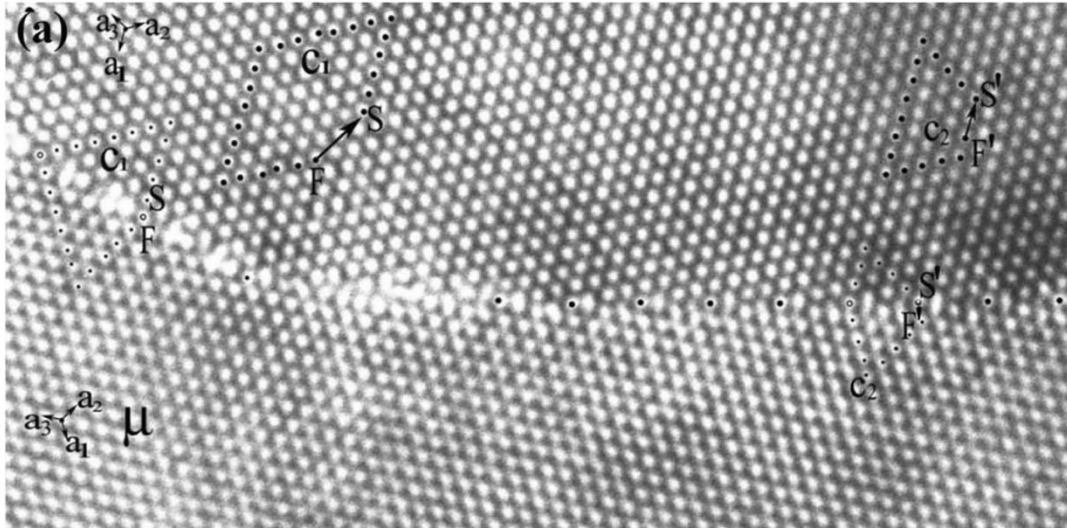


**Figure 5.9a.** HRTEM of another grain boundary with a different configuration.

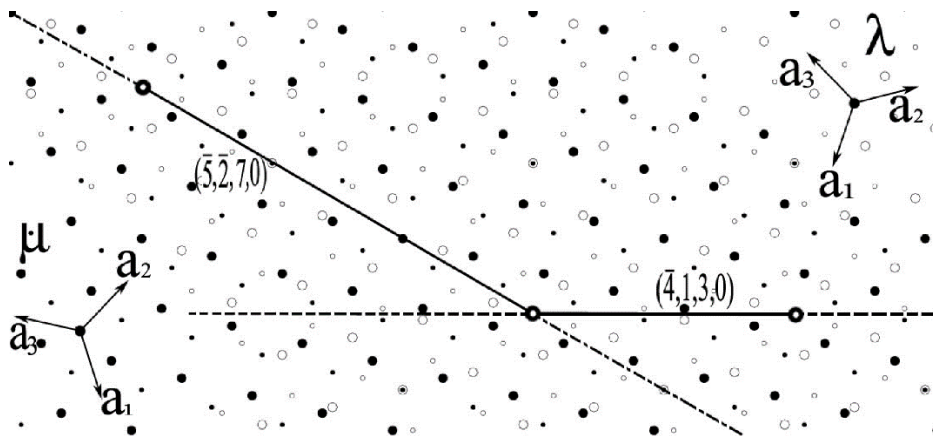


**Figure 5.9b.** The topological layout of a  $\Sigma 13$  GB with rotation angle of  $32.2^\circ$  showing the side and diagonal planes.

In this instance the Burgers vector content inside the  $(\bar{5}, \bar{2}, 7, 0)$  plane is  $-2\mathbf{a}_1 + 2\mathbf{a}_2$ , which is larger than the case above at  $[\bar{1}100]$ , whereas that inside the  $(\bar{4}, 1, 3, 0)$  plane corresponds to  $-2\mathbf{a}_1$ . This latter configuration corresponds to Figure 5.7 and illustrates perfectly the atomic structure of the side of symmetric  $\Sigma 13$  GB at  $\theta = 32.2^\circ$ . The corresponding topological analysis is shown in Figure 5.9b, it thus reproduces the results of the general Table 5.1. From these observations, the next step has been to try to determine the core structure of this  $[\bar{1}100]$  dislocation content, which exhibits an original configuration which cannot be directly deduced from the three known structures

unites for the **a** edge dislocation in wurtzite GaN [5]. For ZnO, these two observations show that the  $[10\bar{1}0]$  type dislocation plays a critical role in the construction of GBs. In the following, we have carried out atomic simulations using combinations of the known 4-, 8-, 57-, 6-atom rings and variations by opening combined cores to determinate the core structure of the observed  $[10\bar{1}0]$  dislocation. The  $\gamma$  surface (energetic minima) of each starting configuration was addressed by taking into account the translations in two directions: parallel to the rotation axis ( $[0001]$  direction) and to GB plane, respectively. Atoms are full relaxed in the third direction which is normal to the GB plane [38].

**Table 5.3.** Atomic structure of  $[0001]$  tilt  $\Sigma 13$  GBs with rotation angle of  $27.8^\circ$  simulated in SW model. The energies are given in  $\text{mJ/m}^2$ .

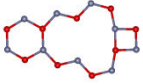
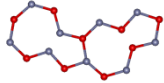
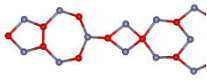
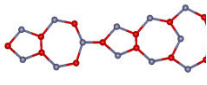
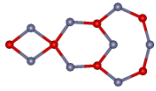
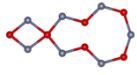
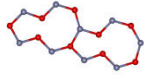
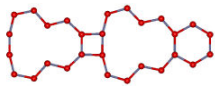
Core Structure	Name	SW(O)	SW(F)	SIESTA	Burgers Vector ( $\lambda$ ) inside one period of STBP
	6684	1861	1861	1384	$(\mathbf{a}_3 - \mathbf{a}_1)$
	57+57-	2481	1690	1694	$(\mathbf{a}_3 - \mathbf{a}_1)$
 (N1)	57468	1394	1304	1642	$-\mathbf{3a}_1$
 (N2)	57578	1651	1619	1525	$-\mathbf{3a}_1$

Table 5.3 and 5.4 list the atomic configurations of the  $\Sigma 13$  GBs period with relatively low formation energy which should correspond to those that may be observed. The corresponding Burgers vector is provided in the last column in order to show the defect contents: **a** or  $[10\bar{1}0]$  type dislocation core. As can be noticed, consistent with the energy comparison of single structure unit based GB in Table 5.2, core structures



possessed the contribution of 57- structure unit generally have high formation energy in Table 5.3 and 5.3. Nevertheless, the energy difference between each type of dislocation cores are too small to conclude a definitely stable configuration which could be observed.

**Table 5.4.** Atomic structure of  $[0001]$  tilt  $\Sigma 13$  GBs with rotation angle of  $32.2^\circ$  in SW model. The energies are given in  $\text{mJ}/\text{m}^2$ .

Core Structure	Name	SW(O)	SW(F)	SIESTA	Burgers Vector ( $\lambda$ ) inside one period of STBP
	468	1177	1497	1364	$-\mathbf{2a}_1$
	457	1609	2195	1367	$-\mathbf{2a}_1$
	57/57	2426	2000	1596	$-\mathbf{2a}_1$
	864866 (N6)	1981	1981	1432	$2(\mathbf{a}_3 - \mathbf{a}_1)$

To this end, extensive image simulations are implemented based on the constructed models to further identify the observed new core structure within  $[10\bar{1}0]$  dislocation content. The multislice technique in JEMS software was used in all simulations [39,40]. Depending on the minimum energy configuration shown in Table 5.3 and the Burgers vector contents identified in Figure 5.9a, the 6684 open core structure is seen to agree with the experimental observations.

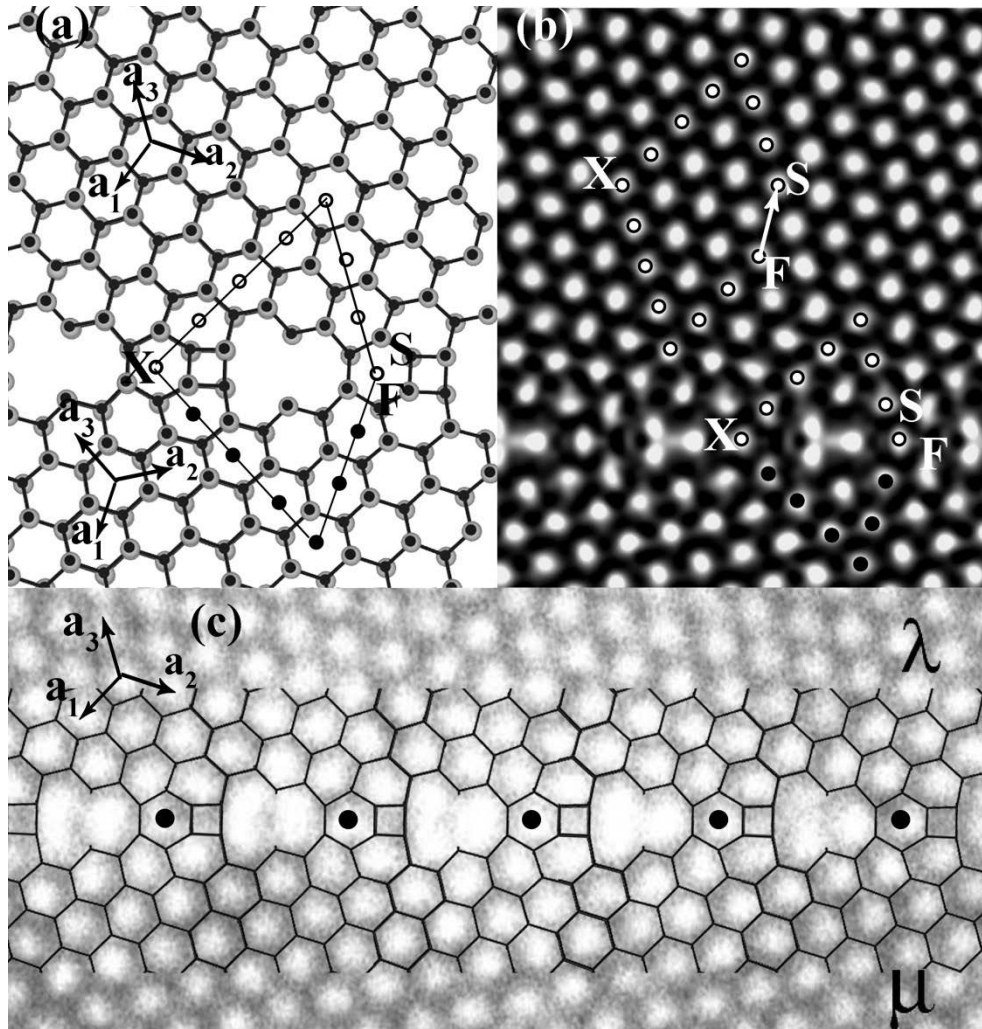


**Figure 5.10.** Atomic core structure of the  $\Sigma 13$  GB. (a) The atomic model of 6684 core structure. (b) The corresponding simulated image of 6684 core structure (defocus: 25 nm, thickness: 5 nm). (c) A HRTEM micrograph of the new core structure in Figure 5.9a lied on  $\{[\bar{3}, 4, \bar{1}, 0]/(\bar{5}, \bar{2}, 7, 0)\}$  boundary plane. Four periods of defect content superposed with atomic structure are shown.

In Figure 5.10(a) the periodic boundary based on 6684 core structure is presented. The SXF circuit  $C_\lambda = 3\mathbf{a}_3 + 4\mathbf{a}_3, C_\lambda = -4\mathbf{a}_3 - 3\mathbf{a}_1$  within one period of GB plane is mapped in  $\lambda$  crystal and a Burgers vector of  $(\mathbf{a}_3 - \mathbf{a}_1)$  is found, which indicates the  $[10\bar{1}0]$  dislocation content, as seen in Figure 5.10(b). The simulated image, under condition of the 5 nm thickness and 25 nm defocus value, shows one large white contrast connect with a normal one in right side within one period of boundary plane and a quite small contrast on the left. This is in great agreement with the experimental micrograph, as shown in Figure 5.10(c) where the periodic atom model is superposed. In the model, the Zn-O bonds in dislocation core are not shown in order to emphasize the large contrast respect to TEM image. But the charge population presents a net charge of -1.196 and +1.2  $e^-$  for the interfacial O and Zn atom respectively, which is fairly matched with those in bulk material. It turns out that all those atoms in interface are fully (four-folds) coordinated. The small variation may come from the elongated bond length. This may explain the rather low formation energy in SIESTA calculation and the same amount of formation energy in SW model with different calculation conditions. And also, the DOS analysis (discussed below) exhibits bulklike behaviors which could further confirm the rationality of this model.

In this chapter, one of the objectives has been to determine the atomic structure of the  $[10\bar{1}0]$  edge dislocation which is a fundamental building unit of  $[0001]$  tilt boundaries as shown by the topological investigation. For GaN, the corresponding structural units in such grain boundaries exhibit only well separated  $a=1/3[11\bar{2}0]$  edge dislocations based on the three basic atom rings: 4-, 8- and 5/7. In this case, the Burgers vectors are found to adapt their orientation in order to accommodate for the GB tilt angle. In ZnO, we have characterized the  $\Sigma 13$  GB along the two tilt angles (32.2 and 27.8°), and most interestingly, it exhibited boundaries along the sides as well along the diagonals. The observed atomic structures of the 4 boundaries reproduced completely the topological description and the  $[10\bar{1}0]$  dislocation is found to be a new and entirely characteristic structural unit. This dislocation exhibits a large core with the elemental atomic configuration of connected 6-8-4 rings. The newly observed core corresponds to the

structure of the  $[10\bar{1}0]$  dislocation, as proposed by Osipyan and Smirnova [37], in their theoretical work on possible dislocations and jogs that may exist in the wurtzite symmetry materials as shown in Figure 5.11.

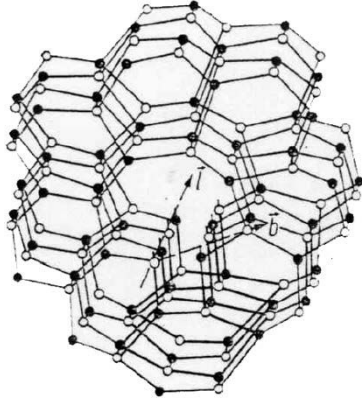


**Figure 5.11.**  $[10\bar{1}0]$  edge dislocation in wurtzite structure. Dislocation line  $\vec{l}$  is along  $[0001]$  axis.

## 5.5 Electronic Properties of GBs

Apart from the topology and energetics, the influences of the GBs in ZnO and GaN related to electronic property are crucial for the practical applications [48]. Especially for the utilization of ZnO varistors, GB-induced deep acceptor levels formed below the bottom of conduction band maximum (CBM) can trap the electrons in bandgap, a double Schottky Barrier thus is build up resulting in the nonlinear current-voltage characteristics in devices [49,50]. The common concept ascribes this deep unoccupied electronic level to the GB itself and/or its cooperative effects with impurities and excessive oxygen [51]. However, the GB-induced deep donor electronic level formed above the VBM is also reported in the literature. For instance, Korner et al. [6] reported that the occupied deep levels above valence band edge originated from the undercoordinated O atoms in pure and/or non-stoichiometric ZnO GBs. Besides, local strain field in the vicinity of GBs is also considered to induce a deep state in some covalent compounds like GaN [52], Si, Ge and SiC, [50] in which the bond distortion is dominant.

In the present study, we have analyzed the electronic structures of those GBs proposed in Table 5.3 and 5.4, the corresponding total DOS are given in Figure 5.12. For better

visualization, the obtained DOS curves are artificially raised by 20-80 (1/eV) in order, with respect to the bulk one. As exhibited in Figure 5.12, with SIC-LDA method, the band gap of ZnO is very well corrected at 3.4 eV for bulk ZnO. For the ZnO GBs deal with in this study, the significant effects on the electronic states associated with GBs mainly appear at the valence band edges. Deep electronic levels are recognized above the VBM for configurations of faceted 5757, 57468 (seen in Figure 5.12(a)) and straight 5757, 457 (shown in Figure 5.12(b)), in which 57-atom ring is present. For the other configurations containing only 4-, 8- and perfect 6-atom rings, there is no additional contribution near the valence band edge. The obtained behavior in total DOS is consistent with the boundary energies calculated in Table 5.3 and 5.4 showing that all 57-atom ring based configurations exhibit relatively high formation energies. It turns out that the 57-structure unit is the main factor to affect the system stability and contribute the deep electronic state. In the 57-structural unit core, a Zn atom faces to a Zn across the boundary plane, and so does O atom in next atom layer along [0001] direction. After structural relaxation, bond length population of Zn-Zn and O-O in 57-structural unit is implemented for all the 57-based GBs. It turns out that, the atom distance of Zn-Zn is about 1.34%-4.37% shorter than that of O-O inside these 57-structural units. This may suggest the coexistence of Zn-Zn wrong bond and oxygen dangling bond (O-O broken bond) in those boundary planes. In addition, an analysis of the local DOS for individual atom contribution reveals that these deep electronic states come from the O dangling bonds in the boundaries. However, if we consider the 6684 core in which the undercoordinated O atoms are present, the Zn/O atom faces to another O/Zn atom across the boundary plane indicates that interfacial broken bonds is the normal Zn-O bonds rather than any wrong bond. In addition, its total DOS does not show any deep state in near VBM. This study confirms that the GB-induced deep occupied states are not solely generated from the undercoordinated O atoms, it more likely comes from the cooperative effective of the established Zn-Zn wrong bond and O-O dangling bond (O-O broken). In contract, the total DOS at the bottom of conduction band are in general delocalized since the interaction of Zn:4s electrons are large in ZnO compound. Their shapes are slightly deviated to narrow the band gap for

all the considered models. This seems to come from the structural deformation rise by the defective boundary regions. Indeed, our present results fairly agree with Oba et al [50], who reported bulklike electronic property for GBs only made by 4-, 8- and 6-atom rings. As seen in our results, deep state is not induced in those structures even for the GBs with dangling bonds like 6684, and 864866.

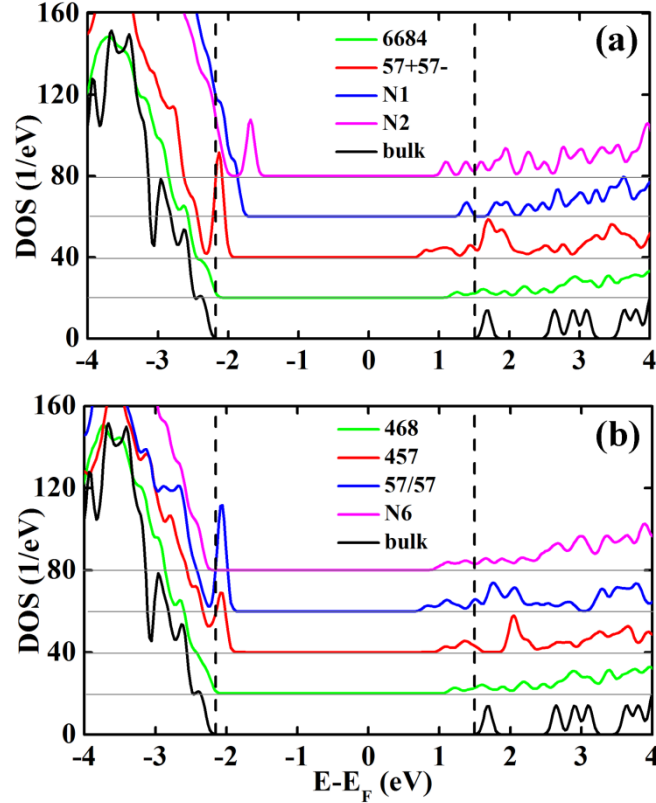


**Figure 5.12.** Total DOS of the dislocation cores shown in Table 5.3 and 5.4. The total DOS of bulk ZnO is given for comparison. Fermi level is specified to zero. The dash lines in each figure indicates the valance band maximum (VBM) and conduction band minimum (CBM) positions.

## 5.6 Conclusion

In summary, a detailed description using topological CSL formalism has been presented with a special focus on [0001] tilt  $\Sigma 7$  and  $\Sigma 13$  GBs. Combining high-resolution TEM and atomistic calculation, we demonstrate that GBs in GaN can be reconstructed using the three basic structural units of **a** edge dislocations. As for ZnO, a new structural unit is shown to possess the dislocation content of  $[10\bar{1}0]$  in  $\Sigma 13$  GBs. The core structure is characterized as a compact mixture of 4-8-6-atom rings. Further investigation on

electronic structure of the proposed GB structures indicate that the GB induced deep occupied state mainly originate from the complex interface ambient of established Zn-Zn wrong bond and O-O dangling bond in those 57-atom ring based GBs.

## References

- [1] L. Hozer, *Semiconductor Ceramics: Grain Boundary Effects*, London: Ellis Horwood; (1994).
- [2] G. H. Bishop and B. Chalmers, *Philos. Mag.* **24**, 515-526 (1971).
- [3] M. J. Weins, H. Gleiter, and B. Chalmers, *J. Appl. Phys.* **42**, 2639-2645 (1971).
- [4] A. P. Sutton and V. Vitek, *Interfaces in Crystalline Materials* Oxford University Press, New York, pp: 286 (1995)
- [5] V. Potin, P. Ruterana, G. Nouet, R. C. Pond and H. Morkoc, *Phys. Rev. B* **61**, 5587-5599 (2000).
- [6] W. Körner and C. Elsässer, *Phys. Rev. B* **81**, 08324 (2010).
- [7] Y. Xin, S. J. Pennycook, N. D. Browning, P. D. Nellist, S. Sivanathan, F. Omnes, B. Beaumont, J. P. Faurie, and P. Gibart, *Appl. Phys. Lett.* **72**, 2680-2682 (1998).
- [8] J. Chen, P. Ruterana, G. Nouet, *Mat. Sci and Eng. B* **82**, 117-119 (2001).
- [9] V. Potin, P. Vermaut, P. Ruterana and G. Nouet, *J. Electron. Mater.* **27**, 266-275 (1998).
- [10] V. Potin, P. Ruterana and G. Nouet, *J. Phys.: Condens. Matter* **12**, 10301-10306 (2000).
- [11] P. Ruterana, B. Barbaray, A. Béré, P. Vermaut, A. Hairie, E. Paumier, G. Nouet, A. Salvador, A. Botchkarev, and H. Morkoc, *Phys. Rev. B* **59**, 15917-15925 (1999).
- [12] P. Vermaut, P. Ruterana, G. Nouet, H. Morkoç, *Phil. Mag. A* **75**, 239-259 (1997).
- [13] A. M. Sánchez, P. Ruterana, M. Benamara, and H. P. Strunk, *Appl. Phys. Lett.* **82**, 4471-4473 (2003).
- [14] V. Potin, G. Nouet and P. Ruterana, *Appl. Phys. Lett.* **74**, 947-949 (1999).

- [15] F. Oba, H. Ohta, Y. Sato, H. Hosono, T. Yamamoto and Y. Ikuhara, Phys. Rev. B **70**, 125415 (2004).
- [16] J. Chen, P. Ruterana and G. Nouet, Phys. Rev. B **67**, 205210 (2003).
- [17] S. Ranganathan, Acta Cryst. **21**, 197-199 (1966).
- [18] P. Ruterana, G. Nouet, Phys. Stat. Sol. (b) **227**, 177-228 (2001).
- [19] L. Lymperakis, J. Neugebauer, M. Albrecht, T. Remmele, and H. P. Strunk, Phys. Rev. Lett. **93**, 196401(2004).
- [20] F. A. Ponce, MRS Bulletin **22**, 51-57 (1997).
- [21] P. Ruterana, V. Potin, B. Barbaray, and G. Nouet, Phil. Mag. A **80**, 937-954 (2000).
- [22] V. Narayanan, K. Lorenz, W. Kim and S. Mahajan, Appl. Phys. Lett. **78**, 1544-1546 (2001).
- [23] P. Vermaut, P. Ruterana, G. Nouet, H. Morkoç, Inst. Phys. Conf. Ser. **146**, 289-292 (1995).
- [24] A. Bere and A. Serra, Phys. Rev. B **65**, 205323 (2002).
- [25] P. S. Hagege and G. Nouet, Acta Cryst. **A45**, 217-227 (1989).
- [26] P. Ruterana, M. Abouzaid, A. Bere and J. Chen, J. Appl. Phys. **103**, 033501 (2008).
- [27] J. Y. Roh, Y. Sato and Y. Ikuhara, J. Am. Ceram. Soc. **97**, 617-621 (2014).
- [28] Y. Sato, T. Mizoguchi, F. Oba, Y. Ikuhara and T. Yamamoto<sup>1</sup>, Phys. Rev. B **72**, 064109 (2005).
- [29] Y. Sato, J. Y. Roh, and Y. Ikuhara, Phys. Rev. B **87**, 140101 (2013).
- [30] A. N. Kiselev, F. Sarrazit, E. A. Stepantson, E. Olsson, T. Claeson, V. I. Bandarenko, R. C. Pond and N. A. Kiselev, Philos. Mag. A **76**, 633-655 (1997).
- [31] J. M. Carlsson, B. Hellsing, H. S. Domingos, and P. D. Bristowe, J. Phys. Condens. Matter **13**, 9937 (2001).
- [32] R. C. Pond and S. D. Vlachavas, Proc. Roy. Soc. A **386**, 95-143 (1983).
- [33] R. C. Pond, N. A. McAuley, A. Serra, and W. A. T. Clark, Scripta Met. **21**, 197-202 (1987).
- [34] R. C. Pond, Line defects in interfaces. F. R. N. Nabarro (Ed.), Dislocations in Solids, Vol. 8, North-Holland, Amsterdam, p.1 (1989).
- [35] R. C. Pond, Interface Sci. **2**, 299-310 (1995).



- [36] J. Hornstra, J. Phys. Chem. Solids **5**, 129-141 (1958).
- [37] Y. A. Osipyan and I. S. Smirnova, Phys. Stat. sol. (b) **30**, 19-29 (1968).
- [38] J. Chen, P. Ruterana and G. Nouet, Phys. stat. sol. (a) **203**, 247-258 (2006).
- [39] P. A. Stadelmann. Ultramicroscopy **21**, 131-146 (1987).
- [40] P. A. Stadelmann, JEMS-EMS java version, 2004, Electron Microscopy Software,  
<http://cimewww.epfl.ch/people/stadelmann/jemswebsite/jems.html>.
- [41] F. H. Stillinger and T. A. Weber, Phys. Rev. B, **31**, 5262-5271 (1985).
- [42] N. Aïchoune, V. Potin, P. Ruterana, A. Hairie. G. Nouet, E. Paumier, Comput.  
Mater. Sci. **17**, 380-383 (2000).
- [43] Y. F. Yan and M. M. Al-Jassim, Phys. Rev. B **69**, 085204 (2004).
- [44] J. M. Soler, E. Artacho, J. D. Gale, A. Garc'ia, J. Junquera, P. Ordejon and D.  
Sanchez-Portal, J. Phys.: Condens. Matter **14**, 2745-2779 (2002).
- [45] J. P. Perdew and A. Zunger, Phys. Rev. B **23**, 5048-5079 (1981).
- [46] J. E. Northrup, J. Neugebauer, and L. T. Romano, Phys. Rev. Lett. **77**, 103-106  
(1996).
- [47] J. M. Carlsson, H. S. Domingos, P. D. Bristowe and B. Hellsing, Phys. Rev. Lett.  
**91**, 165506 (2003).
- [48] S. J. Rosner, E. C. Carr, M. J. Ludowise, G. Giralami, and H. I. Erikson, Appl. Phys.  
Lett. **70**, 420-422 (1997).
- [49] J. D. Russell, D. C. Halls, C. Leach, J. Mater. Sci. Mater. Electron. **14**, 676 (1995).
- [50] F. Oba, S. R. Nishitani, H. Adachi, I. Tanaka, M. Kohyama and S. Tanaka, Phys.  
Rev. B **63**, 045410 (2001).
- [51] D. R. Clarke, J. Am. Ceram. Soc. **82**, 485 (1999).
- [52] S. M. Lee, M. A. Belkhir, X. Y. Zhu, Y. H. Lee, Y. G. Hwang and T. Frauenheim,  
Phys. Rev. B **61**, 16033-16039 (2000).



## Chapter 6

### General Conclusion and Perspective

#### 6.1 General Conclusion

In this work, we investigated two kinds of interfacial defects: inversion domain boundary (IDB) (group III-nitrides and ZnO/GaN heterointerface) and grain boundary (GB) (ZnO and GaN) in wurtzite materials. High-resolution TEM techniques (HAADF, ABF) of microstructural investigation at atomic level was used to measure the atomic configurations of the defects at interfaces and closely combined with the theoretical simulations (molecular dynamic, DFT) to predict the defective boundaries. Furthermore, the electronic properties of the defective interfaces were discovered.

The main results are as follow:

1. Theoretical total-energy calculation predicted Head-to-Head type IDB with an interfacial stacking sequence of AaBbAa-AcCaA (H4 IDB) as the most stable IDB configuration both in group-III nitrides and ZnO homogeneous compounds, with respective to the other candidates.
2. Formation of 2-dimensional electron gas (2DEG) and 2-dimensional hole gas (2DHG) in Head-to-Head IDBs and Tail-to-Tail IDBs, respectively, is uncovered because of the polar character of the materials.
3. Polarity reversal of O-polar ZnO/Ga-polar GaN heterostructure has been achieved within one monolayer using high O/Zn ratio, above a critical value of 1.5, during low temperature P-MBE growth process.
4. This detailed investigation indicated that the polarity reversal took place at one metal layer at heterointerface. From the energetic stability analysis, the H4 IDB with -Zn-O-Ga-N- interface was found to match the experimental results.

5. In analogy, 2DEG and 2DHG are found to appear in Head-to-Head IDBs and Tail-to-Tail IDBs, respectively, at the ZnO/GaN heterointerface.
6. The topological analysis of  $[10\bar{1}0]$  edge dislocation based  $[0001]$  tilt grain boundaries (GBs) in wurtzite structure has been carried out. In GaN, the investigated grain boundaries in GaN are only made of individual  $\mathbf{a}=1/3[11\bar{2}0]$  edge dislocations (three basic structure units: 4-, 8- and 57-atom ring), and it shown that the Burgers vectors adapt their orientation in order to accommodate for the GB tilt angle.
7. For tilts grain boundaries around  $[0001]$  in ZnO, a new structural unit is reported, it corresponds to the  $[10\bar{1}0]$  edge dislocation. The theoretical analysis showed that it is a large core made of connected 6, 8- and 4-atom rings in agreement with the TEM investigation.

## 6.2 Perspectives

In this analysis, we have closely combined the atomic scale TEM measurement and accurate theoretical calculation in order to investigate the interfacial structure of inversion domain boundary and grain boundary. Although the experimental results show good agreement with the theoretical calculation, some limitations still exist and require a further investigation:

- (1) The theoretical models used to simulate the IDBs were taken from Kim and Goo's work. The original models were constructed without taking into account the metal-metal and nonmetal-nonmetal wrong bonds. This may limit the applicability of the theoretical models on the one hand. On the other hand, the implementation of two types of interface alignments (-Zn-O-Ga-N- and -O-Zn-N-Ga-) has been adopted based on the combination of the TEM results (abrupt interface, no intermediate layer, polarity inversion in one monolayer) and growth conditions (low surface mobility in MBE, high O/Zn ratio). We therefore did not consider possible mixtures of Zn/Ga and N/O within the one atomic layer at interface. This point need further experimental confirmation and theoretical analysis.

(3) In grain boundary part, we have pointed out that the boundaries of GaN is only made of the separated  $a=1/3[11\bar{2}0]$  edge dislocations based on the three basic atom rings: 4-, 8- and 57-. For ZnO, topological analysis indicated that the boundaries exhibit  $[10\bar{1}0]$  edge dislocation content along the side or the diagonal of CSL in  $\Sigma 13$  GBs. And we have characterized a specific structural unit of  $[10\bar{1}0]$  edge dislocation with a large core made of 6-8-4 rings. However, extensive experiments are still needed to see if there is another core structure which can be used to describe the GBs in ZnO bicrystals.



# **Structure atomique des domaines d'inversion et joints de grains dans les semiconducteurs wurtzite : Modélisation atomistique et microscopie électronique en transmission haute résolution**

## **Résumé**

Au cours de ce travail, nous avons étudié deux types de défauts interfaciaux: domaines d'inversion (DI) et joints de grains (JG) dans des semiconducteurs de structure wurtzite (nitrures- d'éléments III, ZnO et l'hétérostructure ZnO/GaN) en utilisant le MET haute résolution et la modélisation ab initio. Dans le cas des DI, nos analyses théoriques montrent qu'une configuration tête-à-tête avec une séquence d'empilement à l'interface AaBbAa-AcCaA (H4) est la structure la plus stable dans les composés binaires (nitrures et ZnO wurtzites). De plus, un gaz d'électrons (2DEG) ou de trous (2DHG) à 2 dimensions est formé pour les configurations « tête-à-tête » ou queue-à-queue. A l'interface ZnO/GaN, l'observation de MET très haute résolution a confirmé la configuration H4 avec une interface -Zn-O-Ga-N. Notre modélisation théorique a mis en évidence la formation d'un gaz de trous à 2 dimensions à cette hétérointerface. Nous avons aussi réalisé l'étude topologique, théorique et par MET des joints de grains de rotation autour de l'axe [0001] dans ces matériaux. Dans le GaN, nous avons trouvé que les plans du joint sont simplement formés par des dislocations de type **a** déjà connues pour le matériau en couche mince. Par contre, dans ZnO, la théorie topologique est complètement démontrée, et la dislocation  $[10\bar{1}0]$  est une brique de base dans la constitution des joints de grains avec des cycles d'atomes 6-8-4-.

Mots clés: Domaines d'inversion; Joints de grains; Nitrures-III; MET; Modélisation ab-initio, Dislocation coin  $[10\bar{1}0]$ , Unité structurale

## **The atomic structure of inversion domains and grain boundaries in wurtzite semiconductors: an investigation by atomistic modelling and high resolution transmission electron microscopy**

### **Abstract**

In this work, we investigated two kinds of interfacial defects: inversion domain boundaries (IDBs) and grain boundaries (GB) in wurtzite semiconductors (III-nitrides, ZnO and ZnO/GaN heterostructure) using high-resolution TEM and first-principle calculations. For IDBs, theoretical calculation indicated that a head-to-head IDB with an interfacial stacking sequence of AaBbAa-AcCaA (H4) is the most stable structure in wurtzite compounds. Moreover, 2-dimensional electron gas (2DEG) and 2-dimensional hole gas (2DHG) build up in head-to-head and tail-to-tail IDBs, respectively. Considering the IDB at the ZnO/GaN heterointerface, TEM observations unveiled the H4 configuration with a -Zn-O-Ga-N interface. Moreover the theoretical investigation also confirmed stability of this interface along with the corresponding formation of a 2DHG. A detailed topological, TEM and theoretical investigation of [0001] tilt Grain Boundaries (GBs) in wurtzite symmetry has also been carried out. In GaN, it is shown that the GBs are only made of separated **a** edge dislocations with 4, 5/7 and 8 atoms rings. For ZnO, a new structural unit: the  $[10\bar{1}0]$  edge dislocation made of connected 6-8-4-atom rings is reported for the first time, in agreement with an early theoretical report on dislocations and jogs in the wurtzite symmetry.

Key words: inversion domain boundary; grain boundary; group III-nitrides; TEM; First-principle calculations,  $[10\bar{1}0]$  edge dislocation; Structural unit